Accepted for Publication in the Astronomical Journal
Preprint typeset using LaTeX style emulateapj v. 5/2/11

ESTIMATING THE STAR FORMATION RATE AT 1 KPC SCALES IN NEARBY GALAXIES

Adam K. Leroy[1], Frank Bigiel[2], W.J.G. de Blok[3], Samuel Boissier[4], Alberto Bolatto [5], Elias Brinks[6], Barry Madore[7], Juan-Carlos Munoz-Mateos[1], Eric Murphy[7], Karin Sandstrom[8], Andreas Schruba[8], Fabian Walter[8]

Accepted for Publication in the Astronomical Journal

ABSTRACT

Using combinations of Hα, ultraviolet (UV), and infrared (IR) emission, we estimate the star formation rate (SFR) surface density, $\Sigma_{\rm SFR}$, at 1 kpc resolution for 30 disk galaxies that are targets of the IRAM HERACLES CO survey. We present a new physically-motivated IR spectral energy distribution-based approach to account for possible contributions to 24μm emission not associated with recent star formation. Considering a variety of "reference" SFRs from the literature, we revisit the calibration of the 24μm term in hybrid (UV+IR or Hα+IR) tracers. We show that the overall calibration of this term remains uncertain at the factor of two level because of the lack of wide-field, robust reference SFR estimates. Within this uncertainty, published calibrations represent a reasonable starting point for 1 kpc-wide areas of star-forming disk galaxies but we re-derive and refine the calibration of the IR term in these tracers to match our resolution and approach to 24μm emission. We compare a large suite of $\Sigma_{\rm SFR}$ estimates and find that above $\Sigma_{\rm SFR} \sim 10^{-3}$ M$_\odot$ yr^{-1} kpc^{-2} the systematic differences among tracers are less than a factor of two across two orders of magnitude dynamic range. We caution that methodology and data both become serious issues below this level. We note from simple model considerations that focusing on a part of a galaxy dominated by a single stellar population the intrinsic uncertainty in Hα and FUV-based SFRs are ~ 0.3 and ~ 0.5 dex.

Subject headings: galaxies: evolution — galaxies: ISM — ISM: dust, extinction — stars: formation

1. INTRODUCTION

Comparing the distributions of recent star formation and interstellar gas can illuminate the preconditions for star formation, the impact of local conditions on the conversion of gas to stars, and the process of galaxy assembly. Making these comparisons quantitative requires local estimates of the recent star formation rate (SFR) that span whole galaxies. Such estimates can be reconstructed from the observational signatures of massive stars, which live only a short time after they are born. These signatures include recombination line and thermal radio emission, both produced by ionizing photons emitted by the most massive stars. In regions of active star formation, direct photospheric emission from massive stars also dominates ultraviolet (UV) emission and provides the bulk of starlight reprocessed by dust into infrared (IR) emission.

This paper investigates the use of such observations to estimate the surface density of recent star formation, $\Sigma_{\rm SFR}$, at 1 kpc resolution in nearby galaxies. We focus on 30 galaxies that are targets of the IRAM[9] HERACLES Large Program (Leroy et al. 2009). HERACLES surveyed CO $J = 2 \rightarrow 1$ emission and we have H I maps for each target, mostly from the VLA THINGS survey (Walter et al. 2008). As a result, we know the distributions of both the molecular (H_2) and atomic (H I) interstellar medium (ISM). THINGS and HERACLES aim to constrain theories of star formation via comparisons of H I, H_2, SFR, and environment at matched resolution across large areas. $\Sigma_{\rm SFR}$ estimates matched to the gas maps play a key role in such tests a main goal of this paper is to motivate our approach to such comparisons.

There is no definitive approach to estimate $\Sigma_{\rm SFR}$ at kpc resolutions. Indeed, less attention has been paid to estimating $\Sigma_{\rm SFR}$ for large parts of galaxies than to SFRs for individual regions or whole galaxies. We therefore begin at a low level and focus on issues related to this intermediate scale as we work towards $\Sigma_{\rm SFR}$ estimates. These include the scatter in SFR estimates that arises from considering individual stellar populations, the fraction of IR emission not associated with recent star formation, and the appropriate calibration for "hybrid" UV+IR or Hα+IR tracers.

We begin by defining our approach, which follows other recent work by hybridizing UV or Hα emission with IR emission (Sections 3 and 4). We consider how UV and Hα-based estimates will be affected by isolating individual stellar populations rather than considering an integrated, continuously star-forming population (Section 3). This will be an increasing issue moving from integrated galaxies to sub-galactic scales and we examine Starburst99 (Leitherer et al. 1999) simulations to estimate the magnitude of the issue. We discuss basic trends

[1] National Radio Astronomy Observtory, 520 Edgemont Road, Charlottesville, VA 22903, USA
[2] Institut für Theoretische Astrophysik, Universität Heidelberg, Albert-Ueberle-Str. 2, 69120, Heidelberg, Germany
[3] Astrophysics, Cosmology and Gravity Centre, Department of Astronomy, University of Cape Town, Private Bag X3, Rondebosch 7701, South Africa
[4] Laboratoire d'Astrophysique de Marseille, Université de Provence, CNRS (UMR6110), 38 rue Frédéric Joliot Curie, 13388 Marseille Cedex 13
[5] Department of Astronomy, University of Maryland, College Park, MD, USA
[6] Centre for Astrophysics Research, University of Hertfordshire, Hatfield AL10 9AB, United Kingdom
[7] Observatories of the Carnegie Institution for Science, 813 Santa Barbara Street, Pasadena, CA 91101, USA
[8] Max Planck Institute für Astronomie, Königstuhl 17, 69117, Heidelberg, Germany

[9] IRAM is supported by CNRS/INSU (France), the MPG (Germany) and the IGN (Spain).

among observed intensities of UV, Hα, and IR emission at 1 kpc resolution, including their correlations and relative magnitudes (Section 4). We then explore the effects and potential magnitude of IR emission not directly associated with star formation (Section 5). We adopt a physically motivated approach to this topic, interpreting 24μm emission through the lens of dust models fit to the whole IR spectral energy distribution (SED) and test its effect (Section 5). Based on these calculations, we explore the calibration of empirical "hybrid" (IR+Hα and IR+UV) tracers for our regime (Section 6) and discuss previous work on this topic. We emphasize the substantial uncertainty that still remains in the absolute calibration of such tracers despite much recent attention. We conclude by comparing a large suite of $\Sigma_{\rm SFR}$ estimates (Section 7) and then discussing uncertainties in SFR estimates, outlining our recommended approach to estimate $\Sigma_{\rm SFR}$, and noting several implications of our work for studying star-formation in galaxies (Section 8). We present our conclusions in Section 9.

We focus on IR emission measured by the *Spitzer* Space Telescope, emphasizing the use of 24μm to trace embedded star formation. The 24μm maps produced by *Spitzer* have very good sensitivity and resolution well matched to our ISM data. Many studies of nearby galaxies have revealed a strong empirical correlation between 24μm emission and sites of active star formation (e.g., Calzetti et al. 2005; Alonso-Herrero et al. 2006; Pérez-González et al. 2006; Prescott et al. 2007) and it has been used extensively to investigate the correlations between gas and star formation (e.g., Kennicutt et al. 2007; Bigiel et al. 2008; Leroy et al. 2008; Wilson et al. 2009; Rahman et al. 2010). Critically, as part of the SINGS and LVL legacy programs, *Spitzer* produced well-calibrated maps, publicly available maps for each of our targets. Based on these considerations, we focus on *Spitzer* data here but expect that similar studies using the short wavelength *Herschel* bands will yield complementary results in the near future.

2. DATA

We focus on $\Sigma_{\rm SFR}$ to complement our database of H I and CO maps. We therefore present measurements for galaxies meeting the following criteria: 1) a HERACLES CO map containing a robust detection, 2) *Spitzer* data from 3.6–160μm, and 3) inclination $\lesssim 75°$. This yields the sample of 30 disk galaxies listed in Table 1. This table also gives the distance, the physical resolution corresponding to the (limiting) 13″ angular resolution of HERACLES at that distance, inclination, position angle, optical radius, and the source of the Hα data that we will use for that galaxy. We adopt redshift-independent distances and orientation from the careful literature compilation in Kennicutt et al. (2011) wherever possible, Walter et al. (2008) elsewhere, and from LEDA (Prugniel & Heraudeau 1998) and NED when neither are available.

We will estimate $\Sigma_{\rm SFR}$ from combinations of broadband infrared (IR), UV, and Hα emission with references to other estimates from the literature. By construction HERACLES and THINGS overlap SINGS (Kennicutt et al. 2003), LVL Dale et al. (2009), and the *GALEX* NGS (Gil de Paz et al. 2007) surveys, so Hα, UV, and IR are readily available for each target.

We aim to compare tracers of the ISM and star formation. The maps of the ISM limit the resolution of such comparison; the HERACLES CO maps have 13″ resolution and the naturally-weighted THINGS H I data are often comparable. For most of our targets, this angular resolution corresponds to $\lesssim 1$ kpc and we adopt 1 kpc as our working resolution. We convolve each map to have a symmetric gaussian beam with FWHM= 1kpc. For the *Spitzer* 24μm maps we first convert from the MIPS PSF to a 13″ gaussian beam using a kernel provided by K. Gordon (priv. comm.) then we convolve to 1 kpc. This effectively places our targets at a common distance but does not account for foreshortening along the minor axis. Five galaxies are too distant to convolve the ISM maps to 1 kpc. We mark these in Table 1 and include them in our analysis at the 13″ angular resolution of the CO data.

From these convolved maps, we generate a database of intensity measurements. We sample each map using an hexagonal grid spaced by 0.5 kpc, i.e., one half-resolution element. At each sampling point we measure the CO $J = 2 \rightarrow 1$, 24μm, FUV, NUV, HI, and Hα intensities. We also note dust properties, estimated at coarser resolution, for each point. Table 2 summarizes our data set. The rest of this section explains how we derive the measurements for each point.

2.1. *HERACLES CO*

The HERA CO Line Extragalactic Survey (HERACLES, Leroy et al. 2009) used the Heterodyne Receiver Array (HERA, Schuster et al. 2004) on the IRAM 30m telescope to map CO $J = 2 \rightarrow 1$ emission from 48 nearby galaxies. The HERACLES cubes cover out to r_{25} with angular resolution 13″ and typical 1σ sensitivity 20 mK per 5 km s^{-1} channel. Leroy et al. (2012, in prep.) present the full data set and more details[10].

We estimate H_2 mass surface density, $\Sigma_{\rm H2}$, from CO $J = 2 \rightarrow 1$ intensity via

$$\Sigma_{\rm H2}[{\rm M}_\odot\,{\rm pc}^{-2}] = 6.3\,\left(\frac{0.7}{R_{21}}\right)\,\left(\frac{\alpha_{\rm CO}}{4.4}\right)\,I_{CO}\,[{\rm K\,km\,s^{-1}}], \quad (1)$$

where R_{21} is the CO(2→1)-to-CO(1→0) line ratio and $\alpha_{\rm CO}$ is the CO(1→0)-to-H_2 conversion factor. The formula includes a factor of 1.36 to account for helium. We adopt a line ratio of 0.7[11], and a Galactic conversion factor, $\alpha_{\rm CO} = 4.4\ {\rm M}_\odot\ {\rm pc}^{-2}\ \left({\rm K\ km\ s^{-1}}\right)^{-1}$ equivalent to $X_{\rm CO} = 2 \times 10^{20}\,{\rm cm}^{-2}\,({\rm K\,km\,s^{-1}})^{-1}$. This value is intermediate among recent determinations of the Milky Way $\alpha_{\rm CO}$ (e.g., Strong & Mattox 1996; Dame et al. 2001; Heyer et al. 2009; Abdo et al. 2010) and represents a commonly adopted "best single value" for work on nearby disk galaxies (e.g., Wong & Blitz 2002; Leroy et al. 2008). HERACLES does span a range

[10] All HERACLES data are publicly available from the IRAM and NRAO web pages. Current URL `www.cv.nrao.edu/$\sim$aleroy/HERACLES`

[11] This line ratio is slightly lower than the 0.8 used by Leroy et al. (2009), reflecting the revised efficiency used in the data reduction. This value, 0.7, is the mean ratio of integrated CO $J = 2 \rightarrow 1$ HERACLES flux divided by the CO $J = 1 \rightarrow 0$ flux measured by Young et al. (1995), Helfer et al. (2003), or Kuno et al. (2007).

TABLE 1
Sample Properties

Galaxy	D[a] [Mpc]	res.[b] [kpc]	i [°]	PA [°]	r_{25} [′]	Hα Map	Adopted $\log_{10} f_{\mathrm{H}\alpha+\mathrm{NII}}$ (erg s^{-1} cm^{-2})	Adopted N II/Hα
NGC 0337	19.3[c]	1.24	51	90	1.5	SINGS (Kennicutt et al. 2003)	−11.43	0.23
NGC 0628	7.2	0.46	7	20	4.9	Palomar Las Campanas Atlas	−10.84	0.35
NGC 0925	9.1	0.59	66	287	5.4	Boselli & Gavazzi (2002)	−11.10	0.20
NGC 2403	3.2	0.21	63	124	7.9	Boselli & Gavazzi (2002)	−11.76	0.36
NGC 2841	14.1	0.91	74	153	3.5	Palomar Las Campanas Atlas	−11.53	0.61
NGC 2903	8.9	0.57	65	204	5.9	Hoopes et al. (2001)	−10.71	0.56
NGC 2976	3.6	0.23	65	335	3.6	LVL (Dale et al. 2009)	... [d]	0.13
NGC 3049	19.2[c]	1.24	58	28	1.0	SINGS (Kennicutt et al. 2003)	−11.93	0.40
NGC 3184	11.8	0.76	16	179	3.7	SINGS (Kennicutt et al. 2003)	−11.12	0.52
NGC 3198	14.1	0.91	72	215	3.2	Palomar Las Campanas Atlas	−11.4	0.30
NGC 3351	9.3	0.60	41	192	3.6	LVL (Dale et al. 2009)	... [d]	0.62
NGC 3521	11.2	0.72	73	340	4.2	SINGS (Kennicutt et al. 2003)	−10.81	0.57
NGC 3627	9.4	0.61	62	173	5.1	SINGS (Kennicutt et al. 2003)	−10.75	0.54
NGC 3938	17.9[c]	1.15	14	15	1.8	SINGS (Kennicutt et al. 2003)	−11.25	0.42
NGC 4214	2.90	0.19	44	65	3.4	Hunter & Elmegreen (2004)	−10.77	0.16
NGC 4254	14.4	0.93	32	55	2.5	GoldMine (Gavazzi et al. 2003)	−10.89	0.45
NGC 4321	14.3	0.92	30	153	3.0	GoldMine (Gavazzi et al. 2003)	−11.08	0.43
NGC 4536	14.5	0.94	59	299	3.5	GoldMine (Gavazzi et al. 2003)	−11.36	0.45
NGC 4559	7.0	0.45	65	328	5.2	SINGS (Kennicutt et al. 2003)	−10.97	0.28
NGC 4569	9.86	0.64	66	23	4.6	GoldMine (Gavazzi et al. 2003)	−11.39	0.99
NGC 4579	16.4[c]	1.06	39	100	2.5	GoldMine (Gavazzi et al. 2003)	−11.49	0.62
NGC 4625	9.3	0.60	47	330	0.7	LVL (Dale et al. 2009)	... [d]	0.55
NGC 4725	11.9	0.77	54	36	4.9	Knapen et al. (2004)	−11.42	0.38
NGC 4736	4.7	0.30	41	296	3.9	Knapen et al. (2004)	−10.72	0.71
NGC 5055	7.9	0.51	59	102	5.9	LVL (Dale et al. 2009)	... [d]	0.50
NGC 5194	7.9	0.52	20	172	3.9	Boselli & Gavazzi (2002)	-10.42	0.60
NGC 5457	6.7	4.3	18	39	12.0	Hoopes et al. (2001)	−10.22	0.54
NGC 5713	21.4[c]	1.38	48	11	1.2	SINGS (Kennicutt et al. 2003)	−11.63	0.55
NGC 6946	6.8	0.44	33	243	5.7	SINGS (Kennicutt et al. 2003)	−10.42	0.54
NGC 7331	14.5	0.94	76	168	4.6	SINGS (Kennicutt et al. 2003)	−11.09	0.61

[a] Distances adopted, in order of preference, from compilations by Kennicutt et al. (2011), Walter et al. (2008), and the NED/LEDA databases.
[b] Linear resolution corresponding to 13.3″ angular resolution at the distance of the target.
[c] Too distant to convolve to 1 kpc resolution. Included in analysis at native (13″) resolution.
[d] Flux calibration of LVL Hα maps taken to be correct.

of metallicities (e.g., Moustakas et al. 2010) and observational evidence suggests that the CO-to-H_2 conversion factor varies as a function of metallicity (e.g., see summary in Leroy et al. 2011). However, most low-metallicity, high-α_{CO} systems also tend to be dominated by atomic gas and in this paper only the total (H I+ H_2) gas supply will be relevant. We therefore neglect metallicity variations in α_{CO} for purposes of estimating the dust-to-gas ratio and Σ_{SFR}, though we consider these in our subsequent comparison of Σ_{H2} and Σ_{SFR} (Leroy et al., in prep.).

2.2. *THINGS and Supplemental* H I

We assemble H I maps for all targets, which we use to mask the CO, estimate the dust-to-gas ratio, and explore 24μm cirrus corrections. These come from THINGS (Walter et al. 2008) and a collection of new and archival VLA[12] data (including our programs AL731 and AL735). These supplemental H I are C+D configuration maps with resolutions 13″–25″. We reduced and imaged these a standard way using the CASA package (see Leroy et al. in prep.). In a few cases the native angular resolution of the H I maps corresponds to a spatial resolution coarser than 1 kpc. In these cases we assume the H I to be smooth at scales smaller than the resolution. Given the low dynamic range in H I column densities observed at these resolutions (Walter et al. 2008) this approximation should have minimal impact on our results. We translate 21-cm intensity into H I surface density assuming optically thin emission (see references in Walter et al. 2008) and include helium when quoting atomic gas surface density, Σ_{HI}. Thus

$$\Sigma_{\mathrm{HI}}\ \left[\mathrm{M}_\odot\ \mathrm{pc}^{-2}\right] = 0.020\ I_{\mathrm{HI}}\ \left[\mathrm{K\ km\ s}^{-1}\right] \qquad (2)$$

[12] The National Radio Astronomy Observatory is a facility of the National Science Foundation operated under cooperative agreement by Associated Universities, Inc.

2.3. GALEX *UV*

For 24 galaxies, we use NUV and FUV maps from the Nearby Galaxy Survey (NGS, Gil de Paz et al. 2007). For one galaxy, we use a map from the Medium Imaging Survey (MIS) and we take maps for 5 targets from the All-sky Imaging Survey (AIS Martin et al. 2005). We subtract a small background from the UV maps, determined after blanking the bright (SNR> 2), extended emission in the map. The magnitude of this background is typically $\sim 5 \times 10^{-4}$ MJy sr^{-1}. This corresponds to $\Sigma_{\mathrm{SFR}} \sim 4 \times 10^{-5}$ M$_\odot$ yr^{-1} kpc^{-2}, much lower than the typical Σ_{SFR} considered in this paper. We identify foreground stars via their UV color, by-eye inspection, and the color-based masks of Muñoz-Mateos et al. (2009b), which also blank background galaxies. We correct the FUV maps for the effects of Galactic extinction following Schlegel et al. (1998) and Wyder et al. (2007) — see

Leroy et al. (2008).

2.4. *SINGS & LVL IR*

We use maps of IR emission from 3.6–160μm from the *Spitzer* Infrared Nearby Galaxies Survey (SINGS, Kennicutt et al. 2003) and the Local Volume Legacy survey (LVL, Dale et al. 2009). We mask foreground stars based on UV color, by-eye inspection, and the color-based masks from Muñoz-Mateos et al. (2009b).

2.5. *Literature Hα*

We draw Hα maps from the literature for all of our targets. Whenever possible, we draw maps from the LVL survey. These have clean backgrounds and agree very well with previous flux measurements. For the remaining targets we assembled Hα maps from a variety of literature sources, including the SINGS data release, the GOLDMine database, and surveys with the Palomar-Las Campanas Observatories. The photometric calibrations for these maps were not always available. Even when such calibrations were present, e.g., for the SINGS Hα maps, the integrated fluxes of the maps often scattered substantially about previous measurements (a conclusion verified independently by several of us and also implicitly present in Kennicutt et al. 2009, who mix spectroscopic, literature, and narrow-band imaging measurements for estimates of SINGS galaxies). Therefore for non-LVL maps, we set the overall flux scale of each map by searching the literature for pinning the integrated flux of the Hα map to match the average literature value. Table 1 lists the source and adopted Hα+N II flux for each Hα. When several Hα maps were available for a single target, we chose among them based on a by-eye evaluation of the quality of continuum subtraction and overall flat fielding. Because our coarse working resolution, 13$''$, involves heavily smoothing the maps before any analysis these considerations are more important than seeing or sensitivity.

We process the Hα maps as follows. Whenever available, we apply the masks of Muñoz-Mateos et al. (2009b) to blank bright foreground stars and background galaxies, which often leave residual artifacts in the continuum subtracted image and are in any case not associated with our galaxies. We also mask foreground stars identified by eye. During convolution to our working resolution, we fill in these blank regions with interpolated values.

For non-LVL images we found it necessary to subtract a background determined away from the galaxy. Using the UV and IR 24μm images, we define a mask that encompasses all bright star formation in each galaxy and then verify by eye that this encloses bright Hα emission. We subtracted the median of the map determined outside this region from the whole map. In a few cases that displayed obvious horizontal or vertical striping, we also used this external region to determine and subtract a row- or column-wise median away from the galaxy. For some literature images in which the field of view was fairly small it was not possible to determine a robust median far away from all IR or UV emission. In these cases we subtracted the mode of a histogram of the Hα map after carefully blanking all bright Hα emission. After this processing but before any correction for Galactic extinction or N II contamination we renormalized the Hα maps so that their integrated flux matches values adopted from the literature.

The Hα filter includes both Hα and [N II]. We correct for this effect using the spectroscopic ratios from Kennicutt et al. (2008) and Kennicutt et al. (2009). If the [N II]-to-Hα ratio is not available, we use the galaxy's B-band magnitude with the scaling relation from Kennicutt et al. (2008) to estimate a ratio. We correct the maps for the effect of Galactic extinction following Schlegel et al. (1998).

2.6. *Dust Property Fits*

Of the *Spitzer* far-infrared data, only the 24μm data reach our working resolution but the whole IR SED provides valuable information. We derive a variety of information at the coarser ($\approx 40''$) resolution of the 160μm data. Most of this information comes from fitting the IR SED using the Draine & Li (2007) models. This fitting resembles that in Muñoz-Mateos et al. (2009a) but we include several galaxies that they did not and derive dust-to-gas ratios using our new CO and H I maps.

We carry out the dust fits using the following approach. First, we mask the 8μm and 24μm images using the masks of Muñoz-Mateos et al. (2009b). We then subtract a stellar contribution from the 8μm image using the 3.6μm image as a template. We use a scaling factor of 0.269, adopted from Muñoz-Mateos et al. (2009a); see also Helou et al. (2004). We convolve the 8, 24, 70, and 160μm *Spitzer* images and the H I and CO maps to all share the PSF of *Spitzer* 160μm. We then construct radial profiles of each IR image treating our targets as thin disks with the orientation parameters in Table 1. Before adopting this approach, we experimented with fitting SEDs to each line-of-sight but the lower signal-to-noise ratio and the correlation among uncertainties the fitted dust parameters (e.g., DGR and $U_{\rm min}$) led to instability in the analysis. We found the loss of information from assuming azimuthal symmetry and working in profile to be offset by the improved S/N.

We consider only rings with S/N$>$ 4 at each band and for each IR SED we calculate χ^2 across a grid of dust emission models following Draine et al. (2007) and Muñoz-Mateos et al. (2009a). The free parameters in the grid are: the intensity of the ambient radiation field $U_{\rm min}$ in units of the local interstellar radiation field; the fraction of dust mass illuminated by a distribution of more intense radiation fields (the rest is illuminated by $U_{\rm min}$); $q_{\rm PAH}$, the mass fraction of dust in PAHs; and the total dust mass. To calculate χ^2 we use uncertainties estimated from the scatter in the convolved maps away from the galaxy or 10% of the observed intensity, whichever is higher (this approach follows Draine et al. 2007). We identify best-fit parameters from the minimum χ^2 in our grid search.

Based on these calculations we derive the following quantities for each line of sight: 1) the dust-to-gas ratio, DGR, from comparison to the convolved H I and CO maps; 2) the 24μm-to-total infrared (TIR) luminosity ratio — defined as $\nu L_\nu / L_{\rm TIR}$ for ν at $\lambda = 24\mu$m and $L_{\rm TIR}$ calculated using the prescription of Draine & Li (2007); 3) the 24μm emission per unit dust mass given $U_{\rm min}$ and $q_{\rm PAH}$ for the best-fit model. Along with $U_{\rm min}$, these quantities will allow us to explore contamination of the 24μm

band and the impact of dust abundance on star formation and map 24μm emission to total IR emission.

We derive these IR-based quantities from radial profiles of maps with the $\sim 40''$ resolution of the 160μm data. For this reason, we focus on ratios like the dust-to-gas ratio or 24μm-to-TIR ratio that we expect to vary weakly within a resolution element. Under these assumptions, these can be extrapolated to higher resolution if part of the ratio is known at high resolution.

3. UV AND Hα EMISSION

We start with the assumption that the time-averaged rate of recent star formation can be inferred from the rate of ionizing photon production or the UV luminosity over part of a galaxy. Ionizing photon production is driven by the most massive stars, which live only a very short time. Assuming case B recombination, the distribution of ionizing photons can be traced by Hα emission after correcting for extinction. UV emission traces mainly photospheric direct emission from O and B stars.

Both approaches have a long pedigree with well established tradeoffs and biases. Thanks to its short age sensitivity, Hα emission directly traces the most recent generation of star formation. However, ionizing photons may leak from their parent regions or be absorbed by dust, confusing the mapping of recombination line emission to local star formation. UV emission probes down to lower stellar masses, rendering it less sensitive to stochasticity and variations in the initial mass function and more sensitive to star formation at intermediate ages (a few tens of Myr). Horizontal branch stars and scattered light may contaminate UV emission, and the longer time window to see UV emission may bias the SFR estimate to reflect slightly older populations.

3.1. *Adopted Conversions of UV and Hα to SFR*

We take the relation between SFR to Hα emission from Calzetti et al. (2007),

$$\mathrm{SFR}\ \left[\mathrm{M}_\odot\ \mathrm{yr}^{-1}\right] = 5.3\times10^{-42}\ L_{\mathrm{H}\alpha}\ \left[\mathrm{erg\ s}^{-1}\right]\ . \quad (3)$$

A similar, more recent calculation by Murphy et al. (2011) adjusts the coefficient to 5.37×10^{-42}. Both conversions derive from population synthesis modeling. Equation 3 adopts the default (in 2007) Starburst99 IMF, which resembles a Kroupa (2001) IMF truncated at 120 $\mathrm{M}_\odot$. In surface brightness units Equation 3 is

$$\Sigma_{\mathrm{SFR}}\ \left[\mathrm{M}_\odot\ \mathrm{yr}^{-1}\ \mathrm{kpc}^{-2}\right] = 634\ I_{\mathrm{H}\alpha}\ \left[\mathrm{erg\ s}^{-1}\ \mathrm{sr}^{-1}\right]. \quad (4)$$

This calibration coefficient in Equation 3 is about 0.66 times that suggested by Kennicutt (1998) with the differences mainly due to the adopted IMF. Given our current understanding of the IMF (e.g., Bastian et al. 2010), the conversion in Equation 4 should yield more realistic Σ_{SFR} than the Kennicutt (1998) calibration.

We also adopt the relation between SFR and FUV emission from Salim et al. (2007),

$$\mathrm{SFR}\ \left[\mathrm{M}_\odot\ \mathrm{yr}^{-1}\right] = 0.68\times10^{-28} L_{\mathrm{FUV}}\ \left[\mathrm{erg\ s}^{-1}\ \mathrm{Hz}^{-1}\right]\ . \quad (5)$$

In surface brightness units this is

$$\Sigma_{\mathrm{SFR}}\ \left[\mathrm{M}_\odot\ \mathrm{yr}^{-1}\ \mathrm{kpc}^{-2}\right] = 8.1\times10^{-2}\ I_{\mathrm{FUV}}\ \left[\mathrm{MJy\ sr}^{-1}\right]\ . \quad (6)$$

Equation 6 comes from comparison of SED modeling to UV flux for large set of multiband observations. It adopts a Chabrier (2003) IMF. The coefficient in Equation 6 is $\sim 30\%$ lower than the Kennicutt (1998) value, even after accounting for IMF differences. It is $\approx 20\%$ lower than the more recent calculation by Murphy et al. (2011), which like Kennicutt (1998) considers a theoretical population that has been continuously star-forming for ~ 100 Myr. Salim et al. (2007) discuss this difference. Given the large calibration data set and observational grounding, we take the Salim et al. (2007) FUV calibration to be correct. From the original works, the uncertainty on the coefficients due to metallicity, IMF truncation, and star formation history appears to be ~ 10–30%.

3.2. *Effects of Discrete Star Formation Events*

Equations 4 and 6 assume continuous star formation. This assumption will break down as one considers systems with low integrated SFR, either very small galaxies or parts of a galaxy. For such systems, a single "star formation rate" becomes an inadequate approximation and one eventually approaches the case of a single stellar population with a discrete age. We expect a square kiloparsec portion of an actively star-forming galaxy to contain more than a single single stellar population but investigating this limiting case yields insight into the effect of resolution on SFR estimates.

Figure 1 illustrates aspects of this breakdown (see also Figure 6 in Genzel et al. 2010). We plot Hα and FUV emission (at 1500 Å) as a function of time after an instantaneous burst of star formation. The calculation uses the Starburst99 code (Leitherer et al. 1999), runs out to 100 Myr, and adopts the default evolutionary tracks and IMF.

Age Sensitivity: We use this simple simulation to quantify the age sensitivity of the two tracers, which we report in Table 3. We measure the falloff from peak intensity as a function of time, noting the time that it takes to reach 50% and 5% of the peak. We also derive the time needed to emit 50% and 95% fraction of the cumulative emission given off over the whole simulation. Finally we calculate the luminosity-weighted average time after the burst at which a photon is emitted, defined as

$$\langle\tau\rangle = \int \tau L d\tau \Big/ \int L d\tau\ . \quad (7)$$

Both FUV and Hα emission emit most of their light within a few Myr after the burst. FUV emission then has a long "tail" (in time) over which it continues to emit at a low but significant level. Meanwhile Hα drops precipitously before the burst is 10 Myr old. We recover the expected time sensitivity of a few Myr for Hα (Vacca et al. 1996; McKee & Williams 1997) while FUV covers a wide range of times with a characteristic value of ~ 10–30 Myr and most emission gone by 65 Myr.

Intrinsic Scatter: Luminosity varies with time after the burst, but the same stellar population produces the luminosity at all times. Considering SFR $\sim M/\delta t$ over a relatively long $\delta t \sim 100$ Myr, the time-average SFR is

TABLE 2
Measurements For Each Sampling Point

Quantity	Origin
FUV	*GALEX* (Martin et al. 2005; Gil de Paz et al. 2007)
NUV	*GALEX* (Martin et al. 2005; Gil de Paz et al. 2007)
Hα	Literature (Table 1)
I_{24}	*Spitzer* SINGS & LVL(Kennicutt et al. 2003; Dale et al. 2009)
$\Sigma_{\rm H2}$	IRAM 30-m HERACLES (Leroy et al. 2009, Leroy et al. in prep.)
$\Sigma_{\rm HI}$	VLA THINGS (Walter et al. 2008) + supplemental H I
$\Sigma_{\rm Dust}$	*Spitzer* IR + Draine & Li (2007)
Dust-to-Gas Ratio	*Spitzer* IR + Draine & Li (2007)
24μm-to-TIR ratio	*Spitzer* IR + Draine & Li (2007)
$U_{\rm min}$	*Spitzer* IR + Draine & Li (2007)
24μm/$\Sigma_{\rm Dust}$ for $U_{\rm min}$	*Spitzer* IR + Draine & Li (2007)

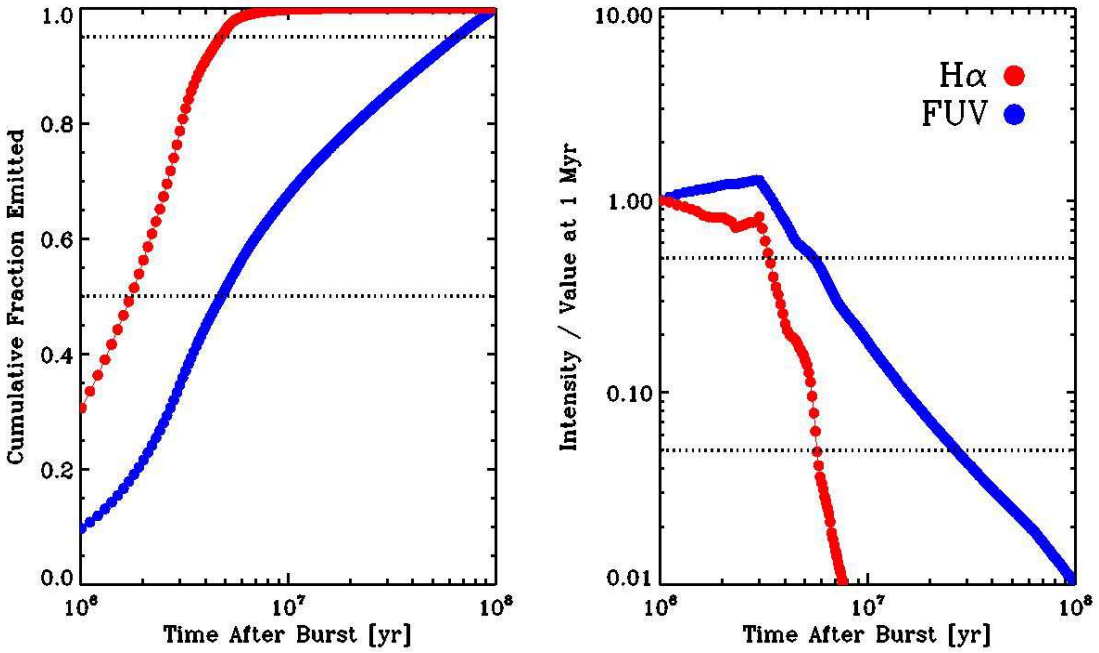

Fig. 1.— *Behavior of a Burst of Star Formation.* Starburst99 calculations for UV (blue) and Hα (red) emission from an instantaneous burst of star formation. The left panel shows cumulative emission as a function of time after the burst, so that one corresponds to all emission over the calculation. The right panel shows intensity of the population relative to intensity at 1 Myr as a function of time. Dashed lines in both panels indicate the 50% and 95% (left) / 5% (right) levels.

TABLE 3
Calculations for a Simple Burst Model

Quantity	Hα	FUV
Time		
... of 50% intensity at 1 Myr	3.4 Myr	5.5 Myr
... of 5% intensity at 1 Myr	5.7 Myr	27 Myr
... of 50% cumulative emission	1.7 Myr	4.8 Myr
... of 95% cumulative emission	4.7 Myr	65 Myr
... luminosity-weighted $\langle\tau\rangle$	2 Myr	14 Myr
Intrinsic scatter[a]		
... out to 5% peak emission	0.36 dex	0.44 dex
... out to 95% cumulative emission	0.26 dex	0.49 dex
... luminosity weighted	0.34 dex	0.63 dex

[a] RMS scatter in log of the Hα or FUV intensity for a fixed-mass burst as it evolves to the indicated point. This will roughly correspond to the scatter in SFR estimates as one isolates a single stellar population.

the same for all times in the calculation. In this light, the varying luminosity implies scatter in the ability to map luminosity to SFR. We calculate this scatter as an estimate of the intrinsic uncertainty in estimating an SFR in a regime better described by discrete events.

We assume that a tracer is visible out to time $t_{\rm visible}$ and that we view it at some random time $t < t_{\rm visible}$. At all t we wish to recover the same SFR. If we use a linear conversion of luminosity to SFR then the scatter in luminosity for $t < t_{\rm visible}$ is the minimum uncertainty in the accuracy of this linear conversion. We try two values $t_{\rm visible}$: the time at which the intensity has fallen to 5% of its value at 1 Myr and the time by which 95% of the total emission has occured. We also report the results of the luminosity-weighted scatter, the second moment in $\log_{10}$ luminosity weighting by $Ld\tau$, which is a more natural but less intuitive quantity.

Table 3 reports these estimates. In the limiting case of discrete bursts we expect a factor of ~ 2 uncertainty (1σ) inferring SFR from Hα and a factor of 3–4 uncertainty inferring SFR from FUV. Over a square kpc, we

expect to average several populations so that the scatter in intensity should be lower than in Table 3 by $\sim \sqrt{N}$, where N is the number of independent populations that we average (e.g., see Schruba et al. 2010).

4. HYBRID Hα+IR AND FUV+IR SFR TRACERS

Dust absorbs Hα and UV light, leaving only $\sim$ 20–40% of the original emission visible in a typical spiral galaxy ($\sim$ 1–2 mag, e.g., Kennicutt 1998) and reprocessing the remainder into IR emission. Correcting for this extinction represents a central challenge to SFR estimation.

Following extensive work in the literature, we will account for extinction by combining Hα and FUV with IR emission. Adding UV and IR emission has an established pedigree (Buat 1992; Meurer et al. 1995, 1999; Cortese et al. 2008), while the combination of Hα and IR has been explored more recently (Calzetti et al. 2007; Kennicutt et al. 2007, 2009). Both combinations offer a powerful way to circumvent the problem of extinction.

Driven by the availability and quality of *Spitzer* data at $\lambda = 24\mu$m, we work with linear combinations of Hα and FUV with IR emission at this wavelength. Several subtle effects complicate the simple conversion of 24μm into SFR. First, the 24μm band does not capture a significant fraction of the total IR luminosity for radiation fields $\lesssim 10^4$ times the Solar Neighborhood value (Draine & Li 2007). Second, the exact fraction of the total IR luminosity emitted near 24μm depends on the dust size distribution, specifically the PAH fraction in the Draine & Li (2007) models, and the mixture of radiation fields illuminating the dust. Finally, producing 24μm does not require ionizing photons. Indeed, stochastic heating by an older stellar population may represent an important contribution in some regions (e.g., Murphy et al. 2011). This last point is a general concern for the use of IR emission to estimate SFR, one that may be somewhat alleviated at 24μm compared to longer wavelengths. For this paper the critical point is that due to these complicating factors, *the use of 24μm emission to infer SFRs has an empirical, not theoretical, foundation.*

4.1. *Definitions and Approach*

We follow recent work in the field by defining a "reference" SFR, which we assume to be correct, and bootstrapping the calibration of more readily observed estimates to match this reference. We draw reference SFRs from literature measurements at wavelengths where dust is only a small concern, including radio continuum emission and Paα emission (Niklas et al. 1997; Murphy et al. 2011; Calzetti et al. 2007). We also use UV and Hα, corrected for extinction based on astrophysical expectations, e.g., by the "Balmer decrement" or IRX-β approach (Storey & Hummer 1995; Osterbrock & Ferland 2006; Kennicutt 1998; Cortese et al. 2008). In Section 6, we give more details on these "reference" measurements and use them to estimate the calibration of the 24μm term in hybrid Hα+24μm or UV+24μm tracers. Before doing so, we define our terms (this section), investigate the relationships among the components of these hybrid tracers (Section 4.2), and consider the effect of 24μm emission not associated with recent star formation (Section 5).

Linear combinations of Hα+24μm or UV+24μm have the desirable properties of working independent of scale and breaking apart into "obscured" and "unobscured" terms in an easy-to-interpret way. This behavior comes at the cost of accuracy, as the conversion of IR intensity to extinction may depend on $\Sigma_{\rm SFR}$ (i.e., luminosity), scale, or the ratio of IR-to-unobscured tracer in a complex way. For example, see Cortese et al. (2008) or the comparison among competing, often regime-dependent and non-linear, conversions of monochromatic 24μm intensity to SFR in Calzetti et al. (2010). We adopt the simple approach, focusing on linear combinations in which the SFR is the sum of an obscured and an unobscured term.

A priori we do not know the weight to apply to 24μm intensity, I_{24}, in combination with an unobscured tracer, $\Sigma_{\rm SFR,tracer}$, to recover $\Sigma_{\rm SFR}$. We solve for this quantity, which we refer to as $w_{\rm tracer}$ and define as

$$w_{\rm tracer} = \frac{(\Sigma_{\rm SFR,ref} - \Sigma_{\rm SFR,tracer})}{0.0025\ I_{24}}\ . \quad (8)$$

Very simply, w is the coefficient to convert 24μm into $\Sigma_{\rm SFR}$ in combination with a tracer of unobscured star formation. It has units of $\rm M_\odot\ yr^{-1}\ kpc^{-2}\ \left(400\ MJy\ sr^{-1}\right)^{-1}$

Thus

$$\Sigma_{\rm SFR} = \Sigma_{\rm SFR,tracer} + w_{\rm tracer}\ \frac{I_{24}}{400\ \rm MJy\ sr^{-1}} \quad (9)$$

For integrated systems, one can derive w by substituting total SFR for $\Sigma_{\rm SFR}$ and L_{24} for I_{24}. For ease of comparison, we choose the normalization of w so that $w_{\rm H\alpha} = 1$ recovers the Calzetti et al. (2007) result, Equation 10.

It will be desirable to consider roughly how much star formation occurs along a line of sight without too much emphasis on a particular calibration. We define the "composite" $\Sigma_{\rm SFR}$, $\langle\Sigma_{\rm SFR}\rangle$, to be the median among $\Sigma_{\rm SFR}$ calculated in a variety of ways. The quantity depends on the adopted suite of tracers, but represents a useful ordinate that we will plot throughout the paper. Our $\langle\Sigma_{\rm SFR}\rangle$ is the median of 1) from $\rm H\alpha + A_{H\alpha} = 1$ mag; 2-9)[13] from Hα+24μm and FUV+24μm with and without 24μm cirrus subtraction, with only cirrus associated with H I subtracted, and with cirrus due to twice our adopted radiation field (see Section 5). 10) FUV + A_{FUV} estimated from the UV spectral slope (the "IRX-β relation" Muñoz-Mateos et al. 2009a); 11-12) FUV + $\rm A_{FUV}$ estimated from the TIR/FUV ratio for young and middle-aged populations following Cortese et al. (2008).

4.1.1. *Existing Work on 24μm-based "Hybrid" Tracers*

Hα+24μm in "H II knots": Calzetti et al. (2007) and Kennicutt et al. (2007) demonstrated that a linear combination of Hα and 24μm intensities recover ionizing fluxes inferred from Paα emission for "HII knots," bright regions from $\sim$ 0.05–1.2 kpc in size, and averages over the central parts of galaxies. Assuming the Paα to trace the true SFR, Calzetti et al. (2007) found:

$$\Sigma_{\rm SFR}\left[\rm M_\odot\ yr^{-1}\ kpc^{-2}\right] = 634\ I_{\rm H\alpha}\ \left[\rm erg\ s^{-1}\ sr^{-1}\right] \quad (10)$$

[13] $A_{\rm H\alpha}$ refers to the extinction (in magnitudes) of Hα emission by dust. $A_{\rm FUV}$ is defined analogously for FUV emission in the GALEX FUV band.

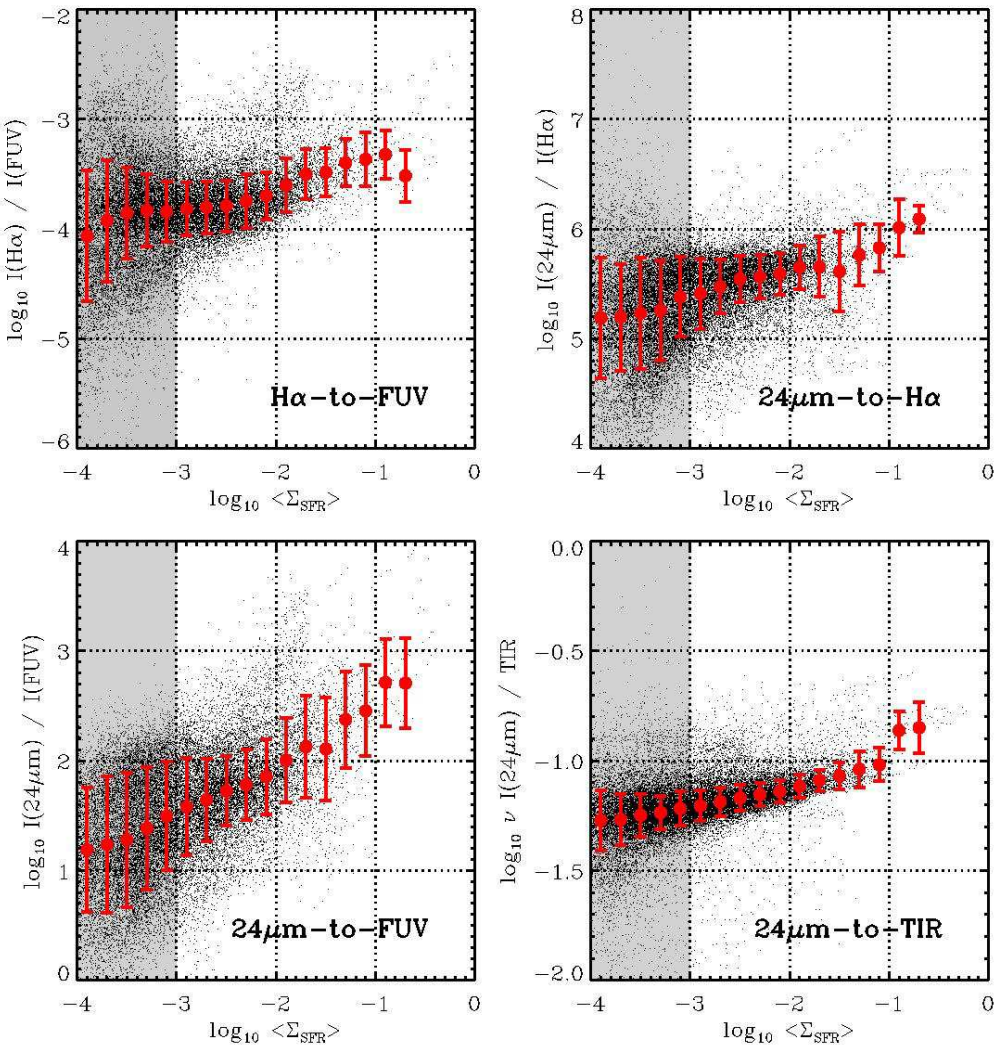

FIG. 2.— *Ratios among terms in hybrid SFR tracers as a function of composite* $\langle\Sigma_{\rm SFR}\rangle$. (*top left*) Ratio of Hα to FUV intensity along a line of sight. (*top right*) Ratio of 24μm to Hα emission. (*bottom left*) Ratio of 24μm to FUV intensity. (*bottom right*) Ratio of 24μm to TIR luminosity surface density (νL_ν) calculated at 45″ resolution ($\sim$ 2.2 kpc at the median distance of our sample). The red points show median ratio in bins of $\langle\Sigma_{\rm SFR}\rangle$ with error bars indicating 1σ scatter.

$$0.0025\ I_{24\mu{\rm m}}\ \left[{\rm MJy\ sr^{-1}}\right]\ .$$

The first term is Equation 4. The second term attempts to account for Hα emission obscured by dust. This corresponds to $w_{\rm H\alpha} = 1$ (see our Equation 9).

Hα+24μm for Whole Galaxies: Kennicutt et al. (2009) compared combinations of 24μm and Hα emission to Hα fluxes corrected for extinction using the Balmer decrement. For whole galaxies, they found $w_{\rm H\alpha} = 0.68$; for the SINGS galaxies specifically, they found $w_{\rm H\alpha} = 0.52$. The Balmer decrements used to calibrate these results appear uncertain, at least for the SINGS galaxies (Moustakas et al. 2010). We return to this result below.

FUV+24μm in Radial Profile: Leroy et al. (2008) proposed that FUV+24μm emission could trace the recent SFR for large parts of the disks of nearby galaxies (see also Thilker et al. 2007). They suggested

$$\Sigma_{\rm SFR}\left[{\rm M_\odot\ yr^{-1}\ kpc^{-2}}\right] = 0.081\ I_{\rm FUV}\ \left[{\rm MJy\ sr^{-1}}\right] + 0.0032\ I_{24\mu{\rm m}}\ \left[{\rm MJy\ sr^{-1}}\right]\ . \quad (11)$$

They picked the 24μm coefficient, $w_{\rm FUV} = 1.3$, to match other estimates in radial profile. In profile, this estimate matched other tracers with $\approx 50\%$ scatter extending down to $\Sigma_{\rm SFR}$ a few times 10^{-4} M$_\odot$ yr^{-1} kpc^{-2}.

4.2. *Relation Among Hybrid Tracer Components*

Figures 2 and 3 show how the components of the hybrid tracers relate to one another. Figure 2 shows the ratios of Hα-to-FUV, 24μm-to-Hα, 24μm-to-FUV, and 24μm-to-TIR emission as a function of $\langle\Sigma_{\rm SFR}\rangle$. Black points show individual kpc-resolution lines of sight. Red points plot the median trend with error bars indicating 1σ scatter. Figure 3 shows the median fraction of the total $\langle\Sigma_{\rm SFR}\rangle$ contributed by each term as a function of $\langle\Sigma_{\rm SFR}\rangle$ (left)

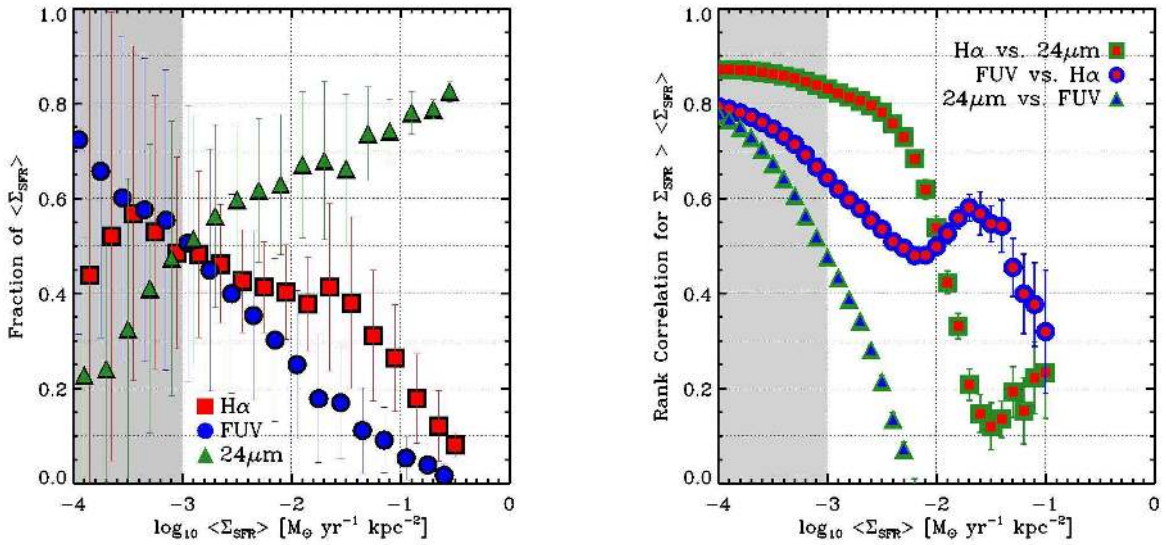

FIG. 3.— *Fractional contribution and correlation among SFR terms:* (*left*) Median fractional contribution of different terms to $\Sigma_{\rm SFR}$ as a function of composite $\langle\Sigma_{\rm SFR}\rangle$: (*red*) H$\alpha$, (*blue*) FUV, and (*green*) 24μm emission with $w = 1$ (so that the Hα and 24μm components roughly sum to 1.0). (*right*) Rank correlation among these terms for all data above a threshold $\langle\Sigma_{\rm SFR}\rangle$ as a function of that threshold.

and the rank correlation among the terms for data above a given $\langle\Sigma_{\rm SFR}\rangle$ as a function of that limiting value (right).

As $\langle\Sigma_{\rm SFR}\rangle$ increases, FUV emission becomes fainter relative to both Hα and 24μm emission. While FUV has about the same magnitude as the 24μm term near $\langle\Sigma_{\rm SFR}\rangle \sim 10^{-3}$ M$_\odot$ yr^{-1} kpc^{-2}, it contributes negligibly, $\lesssim$ 10%, to the overall SFR by $\langle\Sigma_{\rm SFR}\rangle \sim 10^{-1}$ M$_\odot$ yr^{-1} kpc^{-2}. FUV exhibits a significant correlation with Hα even up to high $\langle\Sigma_{\rm SFR}\rangle$, while its correlation with 24μm diminishes quickly, becoming consistent with no correlation or a weak anti-correlation by $\langle\Sigma_{\rm SFR}\rangle \sim 10^{-2}$ M$_\odot$ yr^{-1} kpc^{-2}.

The ratio of 24μm to Hα emission also increases with with increasing $\langle\Sigma_{\rm SFR}\rangle$ though the trend is weaker than for the 24μm-to-FUV ratio. This is consistent with star formation becoming increasingly embedded in regions with high $\Sigma_{\rm SFR}$ and agrees with trends observed in individual SINGS galaxies by Prescott et al. (2007). Hα contributes $\sim$ 40% of the total SFR over the range, $10^{-3} < \langle\Sigma_{\rm SFR}\rangle \sim 10^{-1}$ M$_\odot$ yr^{-1} kpc^{-2}, equivalent to $\sim$ 1 magnitude of extinction. We include few lines of sight with $\langle\Sigma_{\rm SFR}\rangle > 10^{-1}$ M$_\odot$ yr^{-1} kpc^{-2}, but in these regions Hα contributes a small amount to the total SFR.

Over the whole data set, $\langle\Sigma_{\rm SFR}\rangle > 10^{-3}$ M$_\odot$ yr^{-1} kpc^{-2}, Hα and 24μm exhibit the strongest rank correlation among the terms. This correlation diminishes at high $\langle\Sigma_{\rm SFR}\rangle$, with the correlation between Hα and FUV becoming stronger than that between Hα and 24μm at very high $\langle\Sigma_{\rm SFR}\rangle$. However, we emphasize that again that we have little data at very high $\langle\Sigma_{\rm SFR}\rangle$.

The bottom right panel of Figure 2 shows fraction of TIR emission emerging at 24μm increases from $\sim$ 5 to $\sim$ 10% across two decades in $\langle\Sigma_{\rm SFR}\rangle$. This magnitude roughly agrees with the calculations of Draine & Li (2007) and the trend has the expected sense if dust heating increases with $\langle\Sigma_{\rm SFR}\rangle$. The small scatter in the ratio suggests that 24μm can be used to estimate the the bolometric IR emission (though some of the narrowness in the scatter arises because we measure 24μm-to-TIR at the coarse resolution of the 160μm data).

Thus Figures 2 and 3 illustrate the utility of the 24μm band to help trace the SFR. It correlates closely with Hα, traces the bolometric IR emission at higher resolution and sensitivity than can be achieved near the peak of the IR SED, and offers a way to trace the dominant, obscured component of $\Sigma_{\rm SFR}$.

The figures also show how the FUV+24μm tracer operates. Unlike Hα+24μm, where both terms contribute significantly across a wide range of $\langle\Sigma_{\rm SFR}\rangle$, the FUV+24$\mu$m works as a true hybrid, blending tracers appropriate for different regimes: FUV traces $\Sigma_{\rm SFR}$ at low levels where dust extinction is weak and 24μm traces $\Sigma_{\rm SFR}$ in dusty, vigorously star-forming regions.

5. A PHYSICAL APPROACH TO 24μM "CIRRUS"

Weak radiation fields associated with older stellar populations may still excite 24μm emission, leading to a potential 24μm "cirrus." Here we define "cirrus" to mean infrared emission from dust heated by radiation fields not generated by recent star formation. Such radiation fields may illuminate either molecular or atomic gas, so that our "cirrus" can come from dust anywhere in a galaxy (i.e., we do not use the term to refer to exclusively high-latitude or atomic gas). Figures 2 and 3 suggest that this cirrus does not dominate the 24μm over our range of interest. If the cirrus did dominate we would expect a breakdown in the correlation between Hα and 24μm emission and an increase in the ratio of 24μm to other tracers at low $\langle\Sigma_{\rm SFR}\rangle$. Neither effect appears strong in the data. However, even sub-dominant cirrus may represent an important second order correction and a physical estimate of contamination is important.

Proposals to identify and subtract cirrus emission tend to be morphological, defining the cirrus as a smooth background and removing it via image processing techniques such as iterative median filtering (e.g., see Greenawalt et al. 1998; Thilker et al. 2000; Dale et al. 2007; Rahman et al. 2010). Such approaches have very little utility at 1 kpc resolution, where the contrast be-

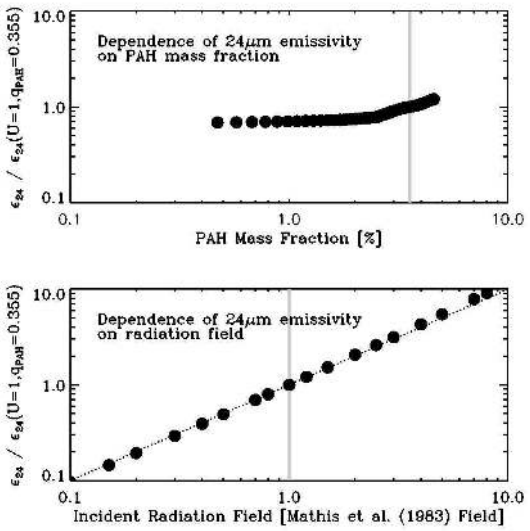

FIG. 4.— *Dependence of 24μm emissivity on dust properties.* Dust emission per unit mass at $\lambda = 24\mu$m, ϵ_{24}, as a function of dust properties in the Draine & Li (2007) models. The upper panel shows the weak dependence of ϵ_{24} on PAH mass fraction, a measure of the dust size distribution. The lower panel plots the dependence of ϵ_{24} on the radiation field illuminating the dust. Gray vertical bars show the value at which we fix the quantity in the other panel. The dotted line in the lower panel shows a linear dependence for comparison.

tween star-forming regions 10–100 pc in size and the embedding medium occurs almost entirely sub-resolution. We therefore focus on an astrophysical cirrus estimate that leverages our multiwavelength data. We estimate the amount of dust present in each resolution element and the radiation field not associated with recent star formation. Together, these give us an estimate of potential cirrus contamination.

The 24μm cirrus will be the product of the amount of dust present, $\Sigma_{\rm dust}$, and the emission per unit dust mass of dust heated by sources other than recent star formation, $\epsilon_{24}^{\rm cirrus}$. Then

$$I_{24}^{\rm cirrus} = \epsilon_{24}^{\rm cirrus}\ \Sigma_{\rm dust}\ . \quad (12)$$

The dust surface density depends on the gas surface density and the dust-to-gas ratio, *DGR*. *DGR*, in turn, varies with metallicity, at least to first order (Draine et al. 2007; Muñoz-Mateos et al. 2009a; Leroy et al. 2011). The 24μm emissivity depends on the dust composition and incident radiation field. In Figure 4 we plot these dependencies as they appear in the Draine & Li (2007) dust models. The top panel shows the weak dependence of $\epsilon_{24}^{\rm cirrus}$ on $q_{\rm PAH}$, the PAH mass fraction. The lower panel shows how $\epsilon_{24}^{\rm cirrus}$ varies with the incident radiation field[14], U. To good approximation over our regime of interest, $0.1 < U < 10$, $\epsilon_{24}^{\rm cirrus}$ will vary linearly with the radiation field not associated with recent star formation.

5.1. *Dust and $q_{\rm PAH}$ for Our Data*

[14] Following Draine & Li (2007) we discuss U in units of the local interstellar radiation field (ISRF, Mathis et al. 1983) and consider only changes to the intensity, not the color, of the field.

To first order $I_{24}^{\rm cirrus}$ depends linearly on $\Sigma_{\rm dust}$ and U and weakly on $q_{\rm PAH}$. We need to estimate each of these terms for each line of sight.

From our fits using the Draine & Li (2007) models to the broadband IR data, we know $\Sigma_{\rm dust}$ at the coarse ($\sim 40''$) resolution of the 160μm data. To estimate $\Sigma_{\rm dust}$ at our finer 1 kpc resolution we assume that the *DGR* varies on large spatial scales. With this assumption, we can take advantage of the finer resolution of our ISM maps to estimate $\Sigma_{\rm dust}$ from $DGR \times \Sigma_{\rm gas}$. Not much is known about the behavior of the *DGR* on kpc scales, but changes in metallicity do tend to be weak over such scales (e.g., Rosolowsky et al. 2008; Moustakas et al. 2010).

Using gas to trace dust on small scales also provides a breakdown between dust associated with H I and dust associated with H_2. H I is less directly associated with star formation than H_2 (see references in Schruba et al. 2011) and most studies of Milky Way cirrus focus on H I (e.g., Boulanger et al. 1996). We may be fairly certain that dust associated with H I and a weak radiation field is not driven by star formation. We therefore experiment with cirrus subtractions that use either only dust associated with H I or all dust.

Our fits using the Draine & Li (2007) models also yield $q_{\rm PAH}$, which we assume to hold sub-resolution. This term only weakly influences ϵ_{24} (Figure 4, top panel) so the approximation should have little impact.

5.2. *The Cirrus Radiation Field for Our Data*

Estimating the radiation field not associated with recent star formation represents the most challenging part of the calculation. Following Draine et al. (2007), we fit our data with a two-component radiation field model. One component is heated by a power law distribution of radiation fields extending to very high U, presumably due to star formation. The other component is heated by a single, weaker radiation field with magnitude represented by the free parameter $U_{\rm min}$. In our fits, $U_{\rm min}$ exhibits a narrow 5–95% range $U = 0.7$–4.0, maximum ≈ 9, and median ≈ 1.35. It displays a positive correlation with $\langle \Sigma_{\rm SFR} \rangle$ ($r_{\rm corr} \sim 0.4$) and the stellar mass surface density ($r_{\rm corr} \sim 0.4$) and an anti-correlation with galactocentric radius ($r_{\rm corr} \sim -0.3$). See Muñoz-Mateos et al. (2009a) for more details.

$U_{\rm min}$ can be interpreted as the ambient radiation field due to old stars but this interpretation is not unique. In the fit this is only the minimum radiation field illuminating the dust. A high $U_{\rm min}$ may still be driven by star formation so that discarding all emission associated with $U_{\rm min}$ may represent an overestimate of the cirrus. For instance, a square kiloparsec centered on the Sun would include several OB associations (Sco-Cen, Perseus, Orion; see Reipurth 2008a,b). These contribute substantially to the average ISRF so that the dominant heating for our local $U = 1$ cannot be said to come from a truly "old" population (see Mathis et al. 1983).

Because of this uncertainty, we undertake an independent estimate of the radiation field driving the cirrus. This investigation appears in Appendix A. We conclude that our data suggest a cirrus driven by a radiation field $U_{\rm cirrus} = 0.5 U_{\rm min}$ with typical magnitude $U_{\rm cirrus} \sim 0.6$. Such a field would drive an equilibrium dust temperature ~ 1 K lower than a $U = 1$ field, consistent with the $\sim$ 16–19 K observed in H I and the

TABLE 4
Effects of Cirrus Subtraction[a]

Description	Median $f_{\rm cirr}$ + 67% Range[b]	$\log_{10}\Sigma_{\rm SFR}^{0.95}$ [c]
Best Cirrus Estimate	0.19 (0.05–0.32)	...
Only Dust with H I	0.10 (0.03–0.17)	...
Twice Cirrus	0.36 (0.10–0.58)	−2.4

[a] See Section 5.3.
[b] Median integrated cirrus fraction and 67% range by galaxy.
[c] $\log_{10}\langle\Sigma_{\rm SFR}\rangle$ below which 95% of IR is deleted.

outskirts of molecular clouds in the Solar Neighborhood (e.g., Boulanger et al. 1996; Schnee et al. 2008; Lee et al. 2011). When we refer to "cirrus" or "cirrus subtraction" throughout the rest paper, we mean that we have calculated the 24μm cirrus emission associated with cirrus powered by $U_{\rm cirrus} = 0.5U_{\rm min}$. When we refer to "double" or "twice" cirrus we calculated the 24μm cirrus emission associated with $U_{\rm cirrus} = U_{\rm min}$, i.e., twice our best estimate.

5.3. *Effect of Cirrus Subtraction*

We combine our dust SED fits (to radial profiles) and our gas maps to estimate the 24μm cirrus everywhere across our sample. We assume that $q_{\rm PAH}$ and the dust-to-gas ratio remain fixed within a radial profile and that $U_{\rm cirrus} = 0.5\ U_{\rm min}$. Combined with our higher-resolution gas maps this gives us a local estimate of $I_{24}^{\rm cirrus}$ for each line of sight. When we refer to "cirrus-subtracted" or corrected data, this intensity has been subtracted from the observed 24μm intensity.

Figure 5 displays our cirrus subtraction graphically for one face-on spiral. Figure 6 plots the fraction of 24μm emission deemed cirrus by our calculation as a function of composite $\langle\Sigma_{\rm SFR}\rangle$. In both plots, we illustrate the impact of our methodology by also plotting results for two variant cirrus subtractions: one using only dust associated with H I and one using twice our adopted radiation field (see Section 5.2). Table 4 synthesizes these data into a few key numbers: the median and 1σ range of cirrus emission subtracted by galaxy and the limiting $\langle\Sigma_{\rm SFR}\rangle$ below which 95% of lines of sight are blanked by each cirrus approach.

The cirrus subtraction suppresses faint emission at large radius and enhances the contrast between bright regions and their surroundings. Subtracting only the component associated with H I removes the low-lying, extended component but has almost no effect on the bright part of the galaxy where most of the star formation occurs. Setting the radiation field to twice its nominal value isolates only the brightest star formation, implying no extinction for Hα or UV emission over the rest of the galaxy.

The magnitude of the 24μm cirrus identified by our approach resembles but somewhat exceeds the fraction of emission identified as powered by old stars in an analysis of integrated SINGS and LVL SEDs by Law et al. (2011). Law et al. (2011) found typically $\sim 7\%$ of 24μm luminosity in these galaxies, on average, to come from old stars. This resembles the fraction of H I-associated cirrus in our data but is about half the total cirrus that we find. Qualitatively, both studies find that dust emission from old stars represents a second-order, but still potentially important, correction in nearby disk galaxies.

6. THE 24μM TERM IN HYBRID SFR TRACERS

As described in Section 4, the calibration of the 24μm component in hybrid tracers is empirical and may vary with scale, target, and "unobscured" tracer. Given this empirical underpinning, any new approach to handling 24μm emission requires that one re-derive, or at least verify, the adopted calibration w. Recall that $w_{\rm tracer}$, defined in Equation 8, is the factor to linearly scale 24μm intensity in combination with an unobscured tracer (the "tracer" indicated in the subscript) to account for dust-obscured star formation (Section 4.1). The lack of a "gold-standard" reference SFR hampers this effort, but we are able to draw several independent estimates of $\Sigma_{\rm SFR}$ from the literature to check $w_{\rm H\alpha}$ and $w_{\rm FUV}$ for our approach and sample.

6.1. *Expectation in the IR-Dominated Case*

From the typical ratio of 24μm-to-TIR emission we can estimate the limiting w, regardless of unobscured tracer, by considering the case where the IR term dominates $\Sigma_{\rm SFR}$. The median ratio of 24μm to TIR emission across our sample is ~ 0.07 (Figure 2). If we equate TIR emission with the reprocessed bolometric light from an embedded, continuous starburst (Kennicutt 1998, corrected to our adopted IMF) this implies $w \sim 2.4$. In fact, the 24μm-to-TIR ratio increases with increasing $\langle\Sigma_{\rm SFR}\rangle$ so that for lines of sight where IR dominates it may be ~ 0.1 or higher which implies a lower $w \sim 1.7$. Based on this calculation, we expect $w \lesssim 2$. It would be possible, in principle, to have w higher than this value for a specific regime but such a calibration could not successfully extend to the case where the overwhelming majority of star formation is embedded and visible only through the IR.

6.2. *Hα+24μm*

6.2.1. *Previous Work on the SINGS Sample*

Our targets heavily overlap the SINGS sample, which has acted as a proving ground for combining Hα and 24μm. Calzetti et al. (2007) and Kennicutt et al. (2007) determined $w_{\rm H\alpha}$ for Hα peaks using Paα as a reference SFR. Kennicutt et al. (2007) found $w_{\rm H\alpha} = 1.23$ and Calzetti et al. (2007) derived $w_{\rm H\alpha} = 1.0$. This difference presumably results from different geometry, escape fraction, and dust properties between M51 and the larger Calzetti et al. (2007) sample, which included M51. Calzetti et al. (2007) found that their 24μm coefficient applies without modification to integrals over the central 50″ of their targets. Subsequently, Kennicutt et al. (2009) considered integrated SFRs for whole galaxies and found a 24μm term $w_{\rm H\alpha} = 0.68$, and $w_{\rm H\alpha} \approx 0.52$ for the SINGS sample specifically. They also found significant scatter in $w_{\rm H\alpha}$ from galaxy-to-galaxy.

Kennicutt et al. (2009) interpreted their low $w_{\rm H\alpha}$ to imply contamination of integrated measurements by a substantial cirrus component. However, they based $w_{\rm H\alpha}$ on Balmer decrement extinctions that were later revised to much higher values by Moustakas et al. (2010). These revised estimates should represent an improvement over those used in Kennicutt et al. (2009) (J. Moustakas, priv. comm.). The revision affects both circumnuclear spectra

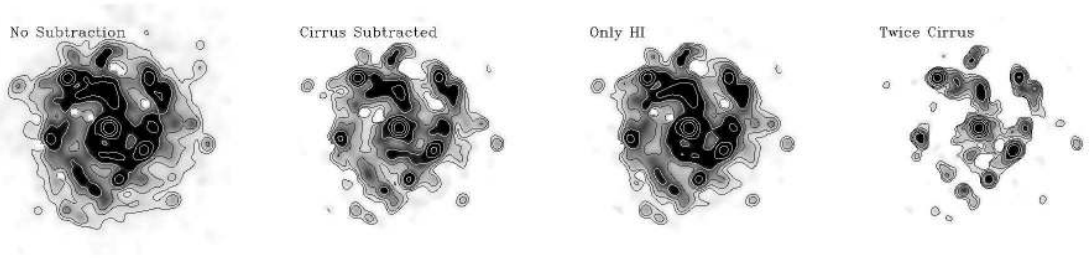

FIG. 5.— *Illustration of the cirrus subtraction for NGC 3184.* Infrared emission at $\lambda = 24\mu$m and 1 kpc resolution. Contours run from 0.1 to 6.4 MJy sr^{-1}, stepping by factors of two. Contours ≥ 0.8 MJy sr^{-1} are white. Individual panels show left to right: no subtraction, 24μm emission after our cirrus subtraction, 24μm emission after our cirrus subtraction applied only for dust associated with H I, and 24μm emission after cirrus subtraction using double the recommended radiation field.

TABLE 5
$\log_{10} w_{\mathrm{H}\alpha}$ BY STUDY FOR SINGS GALAXIES

	C07 Centers	K07 Regions	K09 Centers	K09+M10[a] Centers	K09 Galaxies	K09+M10[a] Galaxies
Median $\log_{10} w_{\mathrm{H}\alpha}$[b]	0.0	0.08	−0.32	0.25	−0.32	0.24
Scatter (1σ) $\log_{10} w_{\mathrm{H}\alpha}$	0.37	0.15	0.24	0.36	0.39	0.52

[a] Fluxes from Kennicutt et al. (2009) and Dale et al. (2007) with Moustakas et al. (2010) Balmer decrements.
[b] Omitting data that yield negative or zero w.

and the radial strips used for galaxy averages [15].

Figure 7 and Table 5 show $w_{\mathrm{H}\alpha}$ for the central parts of galaxies measured by Calzetti et al. (2007) referencing to Paα and for both integrated measurements and the central parts of galaxies referenced to Balmer decrement extinctions by Kennicutt et al. (2009). We also plot $w_{\mathrm{H}\alpha}$ from applying the revised extinctions by Moustakas et al. (2010) to the Kennicutt et al. (2009) measurements. The top panel of Figure 7 shows a histogram of all $w_{\mathrm{H}\alpha}$ measurements, allowing repeats among galaxies using different reference SFRs. The bottom panel shows $w_{\mathrm{H}\alpha}$ broken down by study. Table 5 reports the median and scatter in $\log_{10} w_{\mathrm{H}\alpha}$ by study. Calzetti et al. (2007) did not publish their measurements of individual regions, but Table 5 includes the M51 measurements by Kennicutt et al. (2007). However, both authors emphasize that because of their heavy image processing these "H II knot" calibrations should not apply to large parts of galaxies.

The ensemble of measurements in Figure 7 yields median $w_{\mathrm{H}\alpha} = 0.9$, just below the Calzetti et al. (2007) value. The data exhibit significant scatter, 1σ in $\log_{10} w_{\mathrm{H}\alpha}$ is ≈ 0.45 dex. This scatter includes systematic shifts due to choice of reference SFR and so reflects both an uncertainty and a true scatter. Even for a fixed reference SFR $w_{\mathrm{H}\alpha}$ still scatters significantly ($1\sigma \approx 0.15$–0.52 dex) from galaxy to galaxy. The calibration of $w_{\mathrm{H}\alpha}$ for large parts of SINGS galaxies thus appears very uncertain due to both uncertainty in the reference SFR and galaxy-to-galaxy scatter.

[15] Kennicutt et al. (2009) also work with a larger sample of IRAS 25μm fluxes and Balmer decrements measured by Moustakas & Kennicutt (2006). These measurements were not reconsidered with the improved approach of Moustakas et al. (2010) but because of their higher S/N they may be less affected by the revision than the Moustakas et al. (2010) radial strip measurements (R. C. Kennicutt, priv. comm.). "Circumnuclear" Balmer decrements also changed significantly from Kennicutt et al. (2009) to Moustakas et al. (2010) and the quoted S/N for the Moustakas & Kennicutt (2006) data is similar to that for the Moustakas et al. (2010) "Circumnuclear" spectra.

TABLE 6
$\log_{10} w_{\mathrm{H}\alpha}$ 24μM TERM IN THE HYBRID Hα+24μM TRACER

Reference SFR	No Cirrus	Cirrus
Extinction-Free Estimates		
... Pa-α Centers (C07)	0.05 ± 0.41	0.08 ± 0.44
... Thermal R.C. (N95,N97)	0.00 ± 0.18	0.08 ± 0.19
Balmer Decrements + Hα		
... Galaxy Centers (M10)	0.13 ± 0.34	0.14 ± 0.27
... Whole Galaxies (M10)	0.40 ± 0.16	0.41 ± 0.28
... Galaxy Centers (K09)	-0.59 ± 0.43	-0.51 ± 0.51
... Whole Galaxies (K09)	-0.35 ± 0.24	-0.28 ± 0.27
Other Estimates		
... Gas-Column[a] + Hα	0.61 ± 0.88	0.58 ± 0.97
... $A_{\mathrm{H}\alpha} = 1$ Mag + Hα	-0.06 ± 0.25	0.14 ± 0.28
Average of All Estimates	-0.07 ± 0.47	0.01 ± 0.43

[a] Extinction based on column density of gas following "hybrid model" in Wong & Blitz (2002).

6.2.2. $w_{\mathrm{H}\alpha}$ *in Our Data*

We calculate $w_{\mathrm{H}\alpha}$ for our approach and data set. To do so, we use a reference SFR calculated from Hα plus an extinction correction. We draw the extinction correction from a variety of literature estimates based on , Balmer decrements, contrasting Pα- and Hα-emission, and contrasting radio continuum and Hα emission. These are measured variously for either whole galaxies or central regions. For each extinction estimate, we calculate $w_{\mathrm{H}\alpha}$ following Equation 8, reporting the results in Table 6 and Figure 8.

For the central parts of galaxies we use Paα-based extinctions from Calzetti et al. (2007) and Balmer decre-

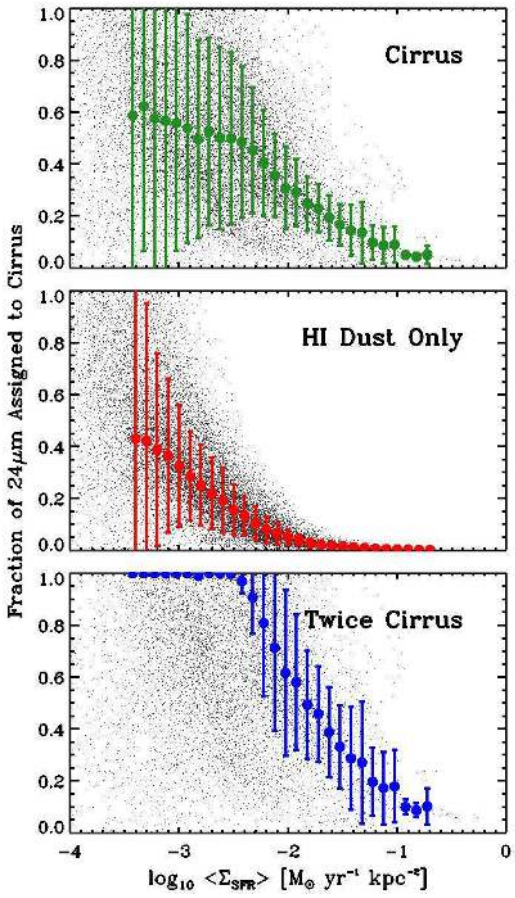

FIG. 6.— *Fraction of 24μm emission identified as cirrus* as a function of $\langle\Sigma_{\rm SFR}\rangle$ from top to bottom: (*green*) our best-estimate cirrus; (*red*) emission only from dust associated with H I; (*blue*) a cirrus powered by a radiation field twice our best-fit value. Individual points show results for 1 kpc resolution elements, colored points show the median and 1σ scatter after binning the data by $\langle\Sigma_{\rm SFR}\rangle$.

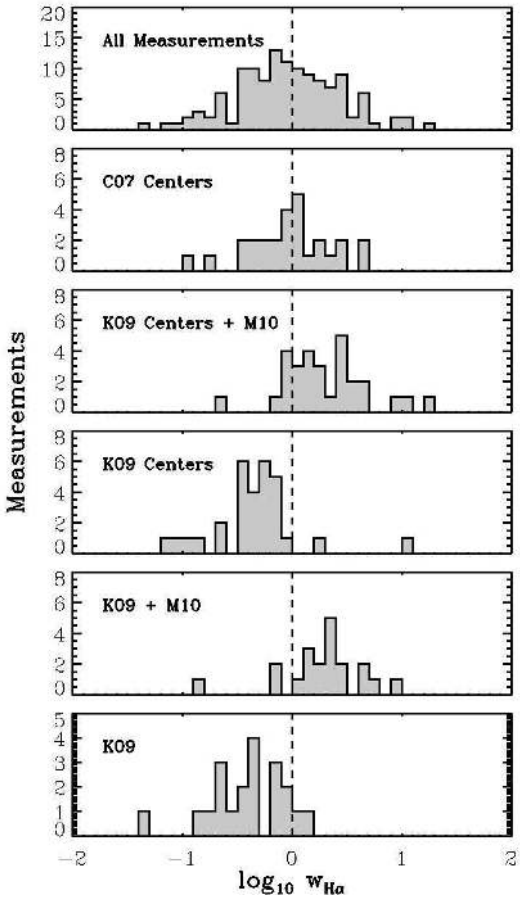

FIG. 7.— *Literature calibrations of the Hα + 24μm tracer in the SINGS sample.* The factor, $w_{\rm H\alpha}$, to be applied to 24μm emission to recover the recent star formation rate in linear combination with Hα for integrals (see definition in Equation 8) over large areas in SINGS galaxies. From top to bottom, the plots show histograms of $\log_{10} w_{\rm H\alpha}$ for (1) all measurements, allowing repeats among galaxies; (2) $50 \times 50''$ central regions referenced to Paα ("C07 Centers" Calzetti et al. 2007); (3) $20 \times 20''$ central regions measured by Kennicutt et al. (2009) and referenced to "circumnuclear" Balmer decrements measured by Moustakas et al. (2010, "K09 Centers+M10"); (4) the same central regions referenced to Balmer decrement-corrected Hα from ("K09 Centers" Kennicutt et al. 2009); (5) whole galaxies measured by Kennicutt et al. (2009) and corrected for extinction using the Balmer decrements measured by Moustakas et al. (2010, "K09+M10"). (6) whole galaxies applying the Balmer decrements measured by Kennicutt et al. (2009, "K09").

ments from Kennicutt et al. (2009) and Moustakas et al. (2010). For full galactic disks with use Balmer decrements from Kennicutt et al. (2009) and Moustakas et al. (2010), supplement these with extinctions estimated from the gas column following Wong & Blitz (2002, their "hybrid" model) and extinctions inferred from comparing thermal radio continuum flux estimates from Niklas et al. (1995, 1997) to our Hα maps (following Wong & Blitz 2002). For full galactic disks, we also benchmark against $A_{\rm H\alpha} = 1$ mag, though this is a typical extinction rather than a true estimate (Kennicutt 1998).

In the "centers" of galaxies, we work with average surface brightnesses in the central 1 kpc. For whole galaxies we work within r_{25} and we assume that the Niklas et al. (1995) fluxes come mostly from inside this area. Except in the case of the radio continuum, we adopt extinctions rather than fluxes from the literature, which somewhat obviates the need to precisely match apertures. Nonetheless we expect our reliance on published measurements rather than the original data to introduce scatter into our results. We do not consider central measurements from NGC 4736 or NGC 4569 because of their Seyfert nuclei. We also omit Balmer decrement measures for NGC 2841 and radio continuum estimates for NGC3351, NGC 5457, and NGC 6946 because they do not return sensible extinction estimates (they yield negative extinction).

As in the SINGS literature, the choice of reference SFR and 24μm treatment affects $w_{\rm H\alpha}$, leading to ~ 0.2 dex systematic variation. Even for a fixed reference SFR and cirrus approach, we find significant scatter among galaxies, typically ~ 0.3 dex (1σ). Although the 24μm offers a powerful, sensitive SFR tracer, its exact calibration remains uncertain. At present it appears that any adopted $w_{\rm H\alpha}$ should be associated with a factor of ≈ 2 uncertainty when applied to a specific galaxy while the average $w_{\rm H\alpha}$ remains uncertain by $\approx 50\%$.

Figure 9 presents an alternative, more direct, visualizations of our constraints on $w_{\rm H\alpha}$. We plot the Hα extinction drawn from the literature, $A_{\rm H\alpha}$, as a function of the ratio of Hα-to-24μm intensity. These two

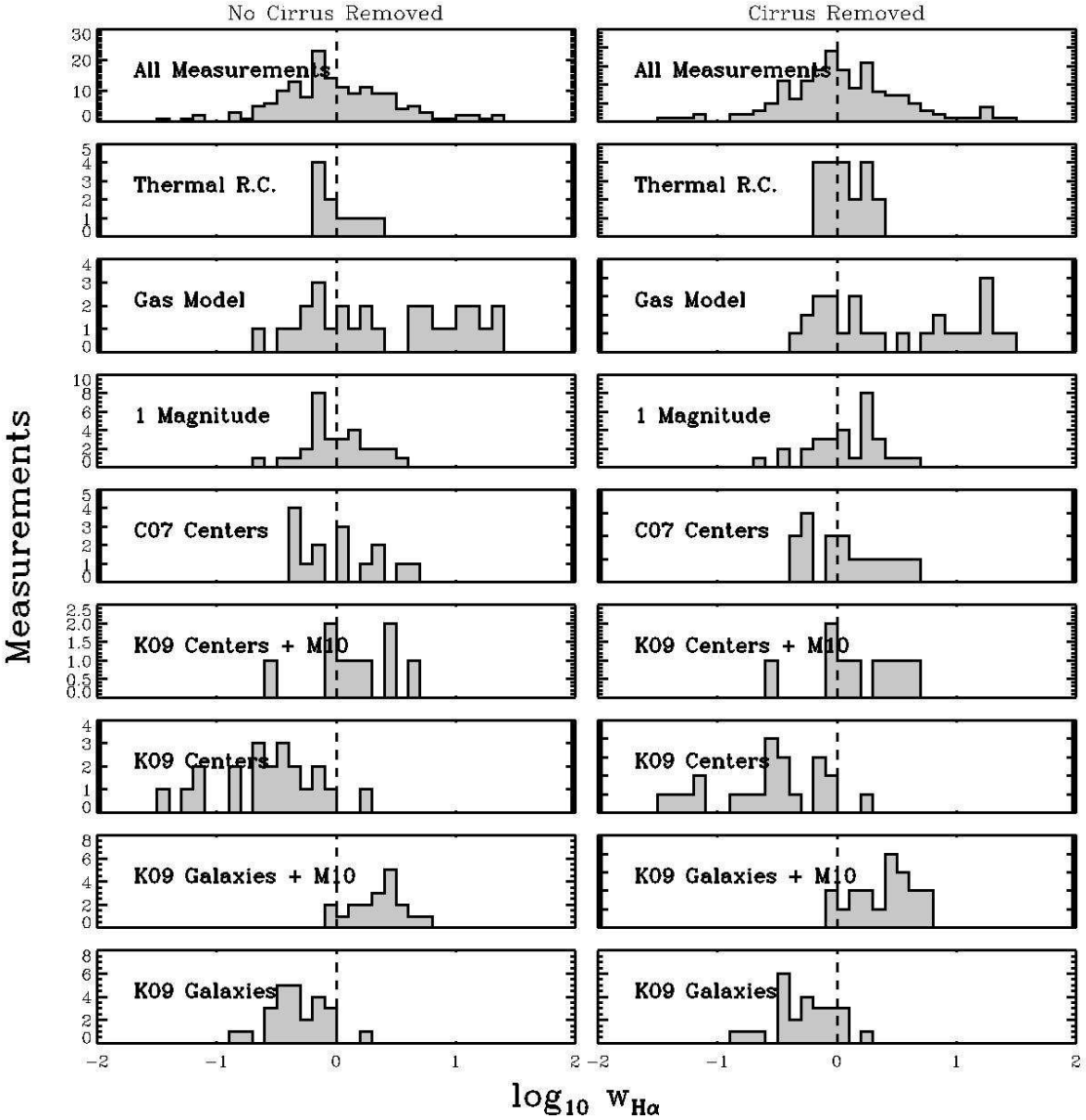

FIG. 8.— *Calibration of the Hα+24μm tracer:* The factor, $w_{\mathrm{H}\alpha}$, to be applied to 24μm emission to recover the recent star formation rate in linear combination with Hα (see definition in Equation 8) for our targets with various estimates of the true extinction. The top row shows the ensemble of all $w_{\mathrm{H}\alpha}$ determinations for 24μm emission. The left column shows results for 24μm maps with no cirrus correction and the right panel shows $w_{\mathrm{H}\alpha}$ determined from 24μm maps that have been corrected for cirrus contamination. In addition to the estimates described in Figure 7 we use extinction estimates based on gas column (Wong & Blitz 2002), thermal radio continuum (Niklas et al. 1997), and a fixed $A_{\mathrm{H}\alpha} = 1$ mag. Galaxies do not repeat in an individual determination but repeat among estimates and in the top row. A vertical line indicates $w_{\mathrm{H}\alpha} = 1$.

quantities directly track one another for the case of a fixed $w_{\mathrm{H}\alpha}$ and the solid curves show the expected relation for $w_{\mathrm{H}\alpha} = 0.25$, (bottom) $0.5, 1, 2$, and 4 (top). The two panels show extinction estimates based on radio continuum and Pα emission (top panel) and Balmer decrements (bottom panel) with the individual studies labeled. If a fixed $w_{\mathrm{H}\alpha}$ perfectly described our data, we would expect to see them strung out along one of the solid lines in Figure 9. This view highlights the contradictions among recent studies and the large scatter in $w_{\mathrm{H}\alpha}$ measurements for individual studies and galaxies.

Treating all determinations equally, we find an average $w_{\mathrm{H}\alpha} \approx 0.85$ with 0.47 dex scatter among individual determinations. Taking $A_{\mathrm{H}\alpha} = 1$ mag and no cirrus subtraction also suggests $w_{\mathrm{H}\alpha}$ about this magnitude, confirming it as a reasonable starting point. This ensemble approach agrees with the average $w_{\mathrm{H}\alpha}$ from the SINGS literature. We recommend $w_{\mathrm{H}\alpha} \sim 0.9$ as a starting point for most analyses if $w_{\mathrm{H}\alpha}$ is otherwise unconstrained. However, given the enormous scatter in results, we can not significantly distinguish this $w_{\mathrm{H}\alpha}$ from the Calzetti et al. (2007) value, $w_{\mathrm{Halpha}} = 1$, and that also represents a reasonable assumption.

When correcting for 24μm cirrus contamination, we adopt a higher $w_{\mathrm{H}\alpha} = 1.3$, driven by the Pa$\alpha$ and radio continuum estimates. These robust, extinction-free independent tracers of ionizing photons suggest $w_{\mathrm{H}\alpha} \approx 1.3$, similar to the $w_{\mathrm{H}\alpha} = 1.23$ found for H II knots in M51 by Kennicutt et al. (2007). Again this roughly matches the $A_{\mathrm{H}\alpha} \sim 1$ mag case. The upper panel in Figure 9 shows the overall consistency of the radio continuum and Pα measurements with this adopted $w_{\mathrm{H}\alpha} = 1.3$, but also

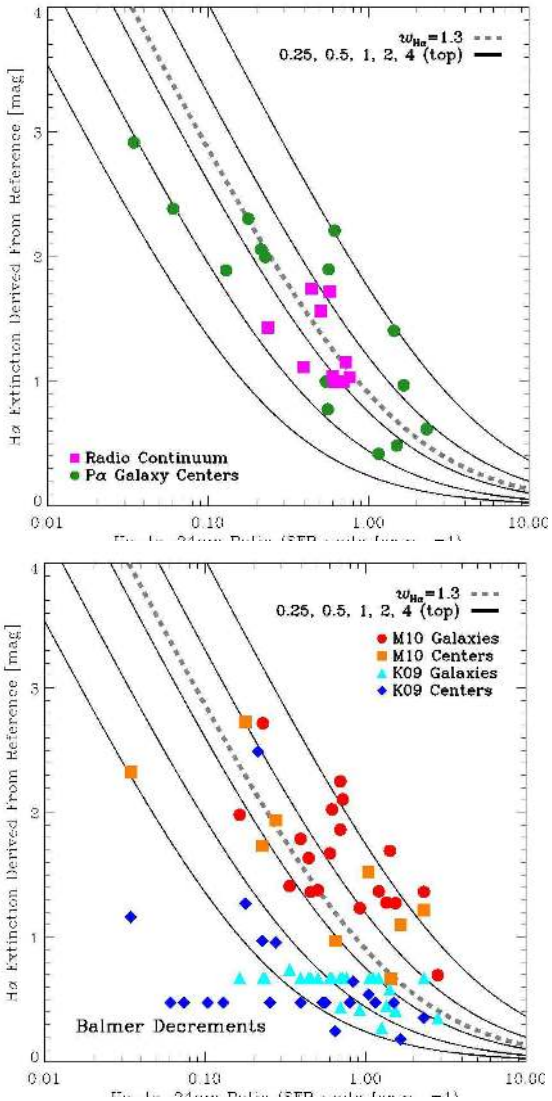

FIG. 9.— *Extinction as a Function of Hα-to-24μm Ratio:* Hα extinction drawn from the literature (y-axis) as a function of Hα-to-24μm ratio in our data (x-axis) measured in star formation surface density units (taking $w_{H\alpha} = 1$ for the ratio). Solid lines plot the expected relation for fixed values of $w_{H\alpha}$ — 0.25 (bottom), 0.5, 1.0, 2, and 4 (top); see the definition of w in Equation 8. The top panel shows measurements for extinction estimated from radio continuum and Pα measurements. The bottom panel shows extinctions estimated from Balmer decrements, marked by study. All measured Hα-to-24μm ratios have been corrected for cirrus emission. The dashed gray line shows our adopted $w_{H\alpha} = 1.3$. The different studies shown here all target the same set of galaxies, so that figure illustrates the uncertainty in the determination of $w_{H\alpha}$ and the contradictory results achieved by recent studies.

highlights the large scatter among even these "good" data. With better reference measurements, it should be possible to distinguish whether the scatter reflects the inadequacy of a linear hybrid to predict extinction or simply inconsistency among challenging measurements.

As in the SINGS literature, the results using Balmer decrement extinctions are confusing and contradictory. The Kennicutt et al. (2009) values yield the low-outlying $w_{H\alpha}$ while the Moustakas et al. (2010) values yield among the highest $w_{H\alpha}$. This difference holds for whole galaxies and galaxy centers, an so does not appear exclusively driven by weighting or S/N issues. The issues

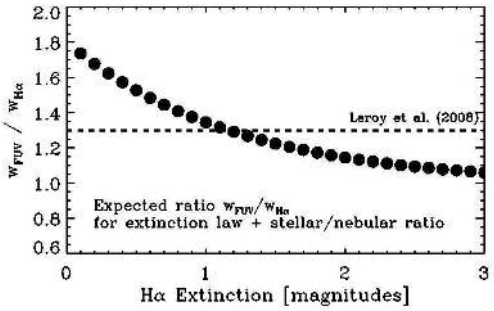

FIG. 10.— *Expectation for $w_{FUV}/w_{H\alpha}$ as a function of Hα extinction.* We plot the ratio of the calibration of 24μm term in combination with FUV, w_{FUV}, to the calibration of the 24μm term in combination with Hα, $w_{H\alpha}$, as a function of the Hα extinction along the line of sight. See the definition of w in Equation 8. The calculation assumes an extinction law with $A_{FUV}/A_R = 8.24/2.33$ and a fixed stellar-to-nebular extinction ratio of $A_{H\alpha}/A_R \approx 2$.

with these measurements can be seen directly in the lower panel of Figure 9, where matched Hα-to-24μm ratios correspond to dramatically different extinction estimates. We incline towards interpreting this wide spread to indicate that these data do not offer a robust reference SFR. However, if one accepts that the Moustakas et al. (2010) values accurately reflect the true extinctions, the Balmer decrements argue for a high $w_{H\alpha} \approx 1.4$–2.4, near the limiting case expected for heavily embedded star formation (Section 6.1).

6.3. *FUV+24μm*

6.3.1. *Expectation Relative to Hα*

Given an extinction curve and a typical stellar-to-nebular extinction ratio, one can relate the FUV and Hα extinctions, A_{FUV} and $A_{H\alpha}$. Leroy et al. (2008) adopted an R-band stellar-to-nebular extinction ratio of $A_{H\alpha}/A_R \approx 2$ (Calzetti et al. 1994; Roussel et al. 2005) and an extinction law where $A_{FUV}/A_R = 8.24/2.33$ (Cardelli et al. 1989; Wyder et al. 2007, using their filter definitions for R and the GALEX FUV band). They then solved for $w_{FUV}/w_{H\alpha}$ as a function of extinction (their Equation D9), which we plot in Figure 10. At high extinctions, virtually all emission is embedded and for FUV+24μm to match Hα+24μm then $w_{FUV} \sim w_{H\alpha}$. At low extinction, the ratio $w_{FUV}/w_{H\alpha} \sim 1.8$, which is the ratio of FUV extinction to Hα for the adopted extinction law and stellar-to-nebular ratio. In the intermediate regime, near the $A_{H\alpha} \sim 1$ magnitude typical of our sample, we expect $w_{FUV}/w_{H\alpha} \sim 1.3$.

6.3.2. *w_{FUV} in Our Data*

We also calculate w_{FUV}. For this exercise, we expand the suite of reference SFRs and carry out the calculation for each line of sight with $\langle\Sigma_{SFR}\rangle > 3 \times 10^{-3}$ M$_\odot$ yr^{-1} kpc^{-2}. Figure 11 shows histograms of w_{FUV} for different reference SFRs and reports the median and scatter for each approach. The first two panels show w_{FUV} from referencing to Hα+24μm using the indicated 24μm processing and $w_{H\alpha}$; we use the same 24μm approach for the Hα+24μm reference and the solution for w_{FUV}. The last four panels reference to Hα with $A_{H\alpha} = 1$ mag, FUV corrected using A_{FUV} inferred from the UV spectral slope following Muñoz-Mateos et al.

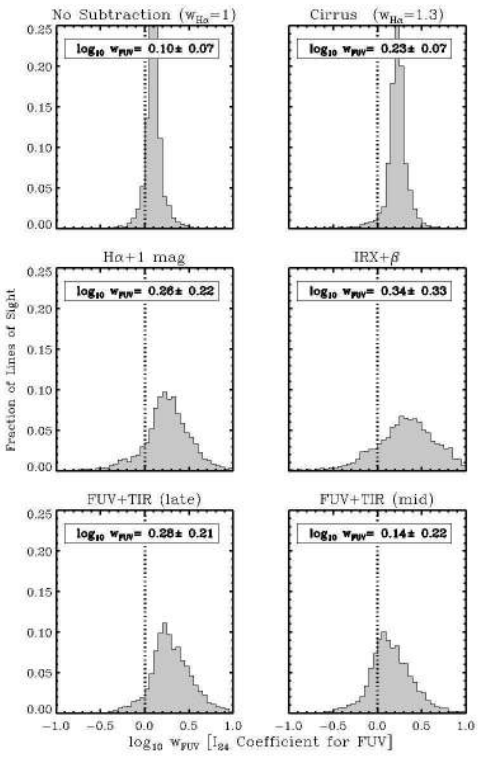

FIG. 11.— *Calibration of the FUV+24μm tracer*: The factor $w_{\rm FUV}$ needed to combine FUV and 24μm, calculated for individual lines of sight (see the definition of w in Equation 8). The top row shows $w_{\rm FUV}$ derived referencing to Hα+24μm with and without cirrus. The middle row shows $w_{\rm FUV}$ derived from Hα plus a typical 1 magnitude of extinction and FUV plus extinction estimated via the IRX-β relation of Muñoz-Mateos et al. (2009a). The bottom row shows $w_{\rm FUV}$ derived from FUV+TIR following Cortese et al. (2008) for a young ("late") and intermediate age ("mid") population, bootstrapping TIR from the 24μm. We list the median $\log_{10} w_{\rm FUV}$ and 1σ scatter among lines of sight for each approach. A vertical line indicates $w_{\rm FUV} = 1$.

(2009a, the so-called "IRX-β" relation), and FUV corrected using $A_{\rm FUV}$ inferred from the TIR/FUV ratio from Cortese et al. (2008). Cortese et al. (2008) consider stellar populations with different ages. We plot results for their youngest population, which we call "late" (their $\tau \geq 8$ Gyr case), and an intermediate age case, which we call "mid" ($\tau = 5$ Gyr).

Referencing to Hα+24μm after cirrus subtraction, we find $w_{\rm FUV} \approx 1.7$. The average of the two Cortese et al. (2008) treatments give a similar value, $w_{\rm FUV} \approx 1.6$. This is higher than the $w_{\rm FUV}$ recommended by Leroy et al. (2008) but note that we have also increased $w_{\rm H\alpha}$ to 1.3 from the $w_{\rm H\alpha} = 1.0$ used in Leroy et al. (2008). The revised $w_{\rm FUV}$ is still $\sim 1.3\ w_{\rm H\alpha}$, in accordance with our expectations (Figure 10). Because this value can be derived from the Cortese et al. (2008) FUV+TIR approach alone, this calculation establishes the FUV+24μm as somewhat independent of Hα+24μm, and not a purely bootstrapped tracer.

Different approaches yield $w_{\rm FUV}$ from 1.3–2.1. The scatter in $w_{\rm FUV}$ appears lower than in $w_{\rm H\alpha}$ but this is mostly due to the fact that our references often already include 24μm. To the degree that we bootstrap the calibration from either our $w_{\rm H\alpha}$ or the Cortese et al. (2008) approach, $w_{\rm FUV}$ carries the same $\sim$ 0.2–0.3 dex uncertainty associated with those approaches.

7. COMPARISON AMONG TRACERS AND UNCERTAINTY

Having examined the constituent terms, contamination, and calibration of hybrid tracers, we now gauge the practical impact of our choices on $\Sigma_{\rm SFR}$. Figures 12 – 14 compare pairs of tracers as a function of $\langle\Sigma_{\rm SFR}\rangle$.

Figure 12 shows the effect of our cirrus subtraction and compares FUV and Hα-based tracers. The bottom row shows that Hα and FUV based approaches agree well for matched treatments (see also Leroy et al. 2008). The top row shows that the cirrus subtraction has a net effect of 10s of percent, but less than 100% across the range $10^{-3} < \langle\Sigma_{\rm SFR}\rangle < 10^{-1}$ M$_\odot$ yr^{-1} kpc^{-2}. Below this range, the offsets can become much more severe as the Hα maps become unreliable and the cirrus correction has removed virtually all 24μm emission.

Figure 13 shows the effect of pushing the cirrus subtraction to its limits. The most conservative approach, removing only emission from dust associated with H I, has a very small impact on the net $\Sigma_{\rm SFR}$. If we adopt double our nominal cirrus estimate then the 24μm component of the tracer is largely removed below 10^{-2} M$_\odot$ yr^{-1} kpc^{-2}, suppressing $\Sigma_{\rm SFR}$ by a factor of ~ 2 (recall the typical $A_{\rm H\alpha} \sim 1$ mag).

Figure 14 presents comparisons with "independent" tracers: a fixed $A_{\rm H\alpha} = 1$ mag; FUV + $A_{\rm FUV}$ inferred from the UV spectral slope (Muñoz-Mateos et al. 2009a, "IRX-β"); $A_{\rm H\alpha}$ inferred using the "hybrid" gas model of Wong & Blitz (2002); and FUV combined with $A_{\rm FUV}$ estimated from the TIR/FUV ratio for a young and middle-aged population (Cortese et al. 2008).

Some "tilt" can be seen in the comparisons, particularly the comparison with "independent" tracers. This usually has the sense that our IR-based $\Sigma_{\rm SFR}$ estimate recovers higher $\Sigma_{\rm SFR}$ than the comparison indicated in high $\Sigma_{\rm SFR}$, presumably heavily embedded regions. In any case magnitude of systematic differences rarely exceeds a factor of 2 (0.3 dex) over 2 orders of magnitude in dynamic range. Only using gas to infer the extinction diverges dramatically at high $\langle\Sigma_{\rm SFR}\rangle$, an issue also noted by Leroy et al. (2008) that presumably results from complex geometry.

The scatter among different tracers in Figures 12–14 allows us to estimate the uncertainty in any given estimate of $\Sigma_{\rm SFR}$. For each line of sight in our data set, we take the median absolute deviation-based scatter of our ensemble of $\Sigma_{\rm SFR}$ estimates about the mean value for that point. That is, we measure the scatter of $\Sigma_{\rm SFR}$ estimates about the mean value for each point. This folds some systematic uncertainty into the estimate because some of our approaches contradict one another. Inasmuch as each approach represents a reasonable method to estimate $\Sigma_{\rm SFR}$, however, this simple calculation should yield a good idea of how uncertain a particular $\Sigma_{\rm SFR}$ estimate actually is. Overall for $\langle\Sigma_{\rm SFR}\rangle > 10^{-3}$ M$_\odot$ yr^{-1} kpc^{-2} we find a scatter of ~ 0.13 dex. We illustrate this in Figure 15, plotting a histogram of the scatter of individual estimates about the median $\Sigma_{\rm SFR}$ for that line of sight.

We have also argued that the calibration of the 24μm term in the hybrid tracers appears systematically uncertain by a factor of ~ 2. The 24μm contributes $\sim 60\%$ of the SFR on average, so this suggests a systematic uncertainty of order of 0.15–0.2 dex in the magnitude of the to-

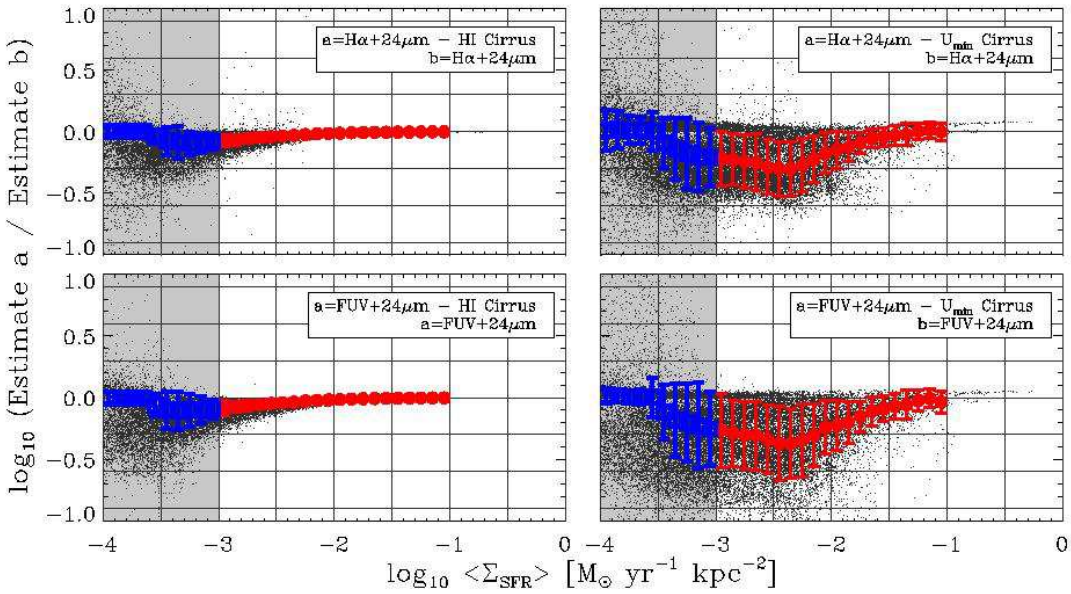

FIG. 12.— *Hybrid tracers with and without cirrus:* Ratio ($\log_{10}$) of hybrid star formation rate tracers as a function of composite $\langle\Sigma_{\rm SFR}\rangle$. The gray area shows where $\langle\Sigma_{\rm SFR}\rangle < 10^{-3}$ $M_\odot$ yr^{-1} kpc^{-2}, our lower limit for a reliable $\Sigma_{\rm SFR}$. Red circles show the median ratio in bins of $\langle\Sigma_{\rm SFR}\rangle$ with error bars indicating 1σ scatter in that bin; blue circles show the same where $\langle\Sigma_{\rm SFR}\rangle < 10^{-3}$ $M_\odot$ yr^{-1} kpc^{-2} and we consider $\Sigma_{\rm SFR}$ unreliable. Black points show individual lines of sight. The top shows the effect of subtracting the IR cirrus on the integrated estimate. The bottom row compares Hα and FUV-based tracers for matched cirrus approaches

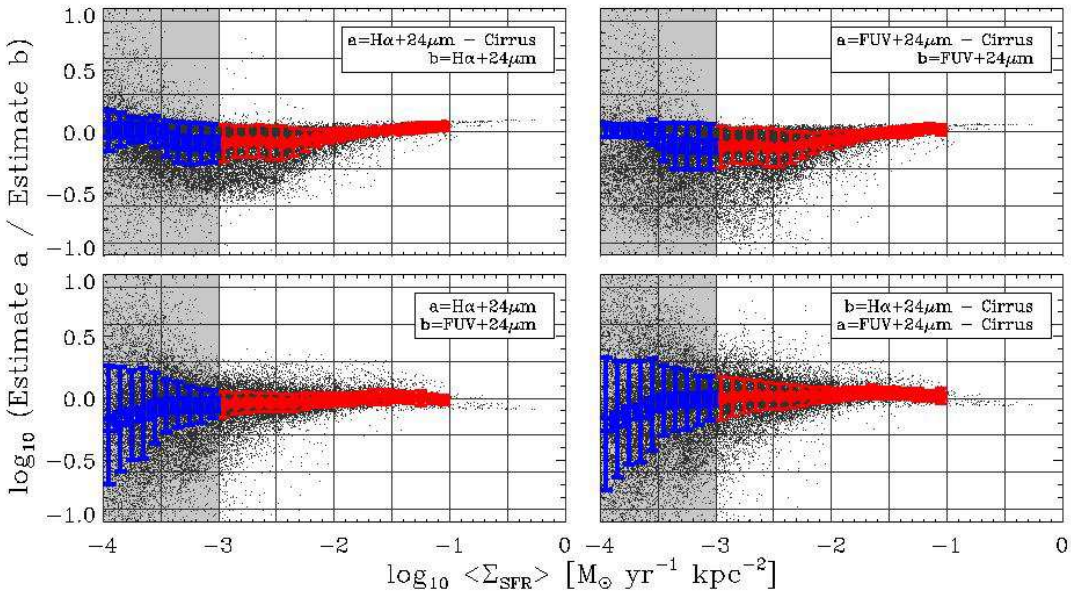

FIG. 13.— *Effect of varying the cirrus approach:* Ratio ($\log_{10}$) of star formation rate tracers as a function of composite $\langle\Sigma_{\rm SFR}\rangle$. The gray area shows where $\langle\Sigma_{\rm SFR}\rangle < 10^{-3}$ $M_\odot$ yr^{-1} kpc^{-2}, our lower limit for a reliable $\Sigma_{\rm SFR}$. Red circles show the median ratio in bins of $\langle\Sigma_{\rm SFR}\rangle$ with error bars indicating 1σ scatter in that bin; blue circles show the same where $\langle\Sigma_{\rm SFR}\rangle < 10^{-3}$ $M_\odot$ yr^{-1} kpc^{-2} and we consider $\Sigma_{\rm SFR}$ unreliable. Black points show individual lines of sight. The left panels show the effect of subtracting only cirrus emission from dust associated with H I. The right panel shows the effect of setting the radiation field to double our adopted value.

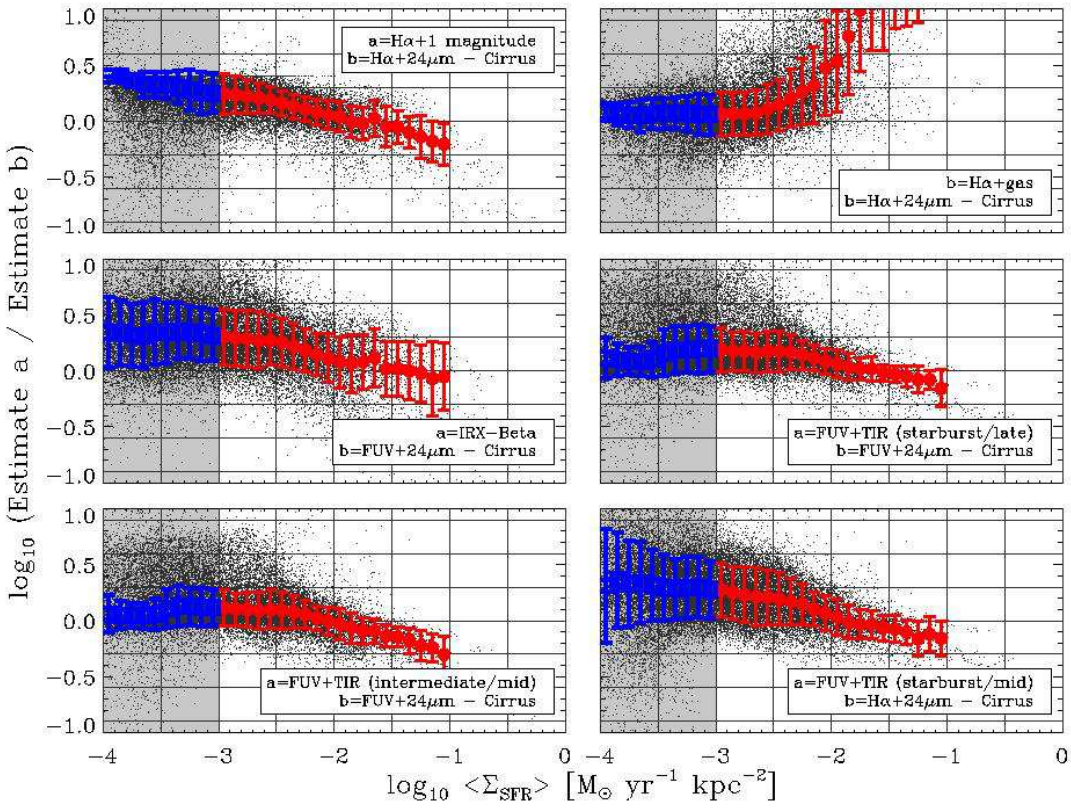

FIG. 14.— *Comparison with other tracers:* Ratio ($\log_{10}$) of star formation rate tracers as a function of composite $\langle\Sigma_{\rm SFR}\rangle$. The gray area shows where $\langle\Sigma_{\rm SFR}\rangle < 10^{-3}$ $M_\odot$ yr^{-1} kpc^{-2}, our lower limit for a reliable $\Sigma_{\rm SFR}$. Red circles show the median ratio in bins of $\langle\Sigma_{\rm SFR}\rangle$ with error bars indicating 1σ scatter in that bin; blue circles show the same where $\langle\Sigma_{\rm SFR}\rangle < 10^{-3}$ $M_\odot$ yr^{-1} kpc^{-2} and we consider $\Sigma_{\rm SFR}$ unreliable. Black points show individual lines of sight. Each panel compares one of our hybrid tracers to another approach.

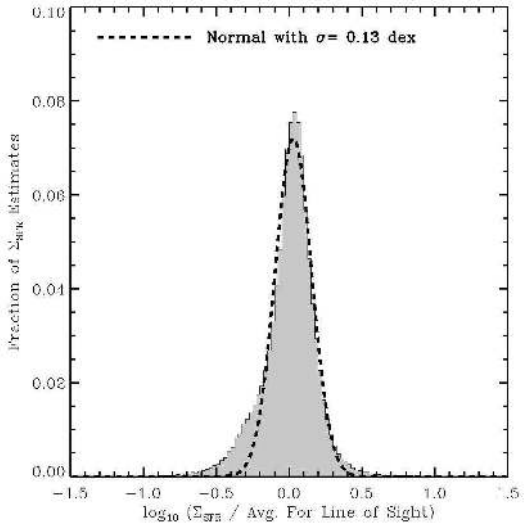

FIG. 15.— *Uncertainty estimated From scatter among tracers:* Distribution of $\Sigma_{\rm SFR} - \langle\Sigma_{\rm SFR}\rangle$, the difference between each individual SFR estimate in our data set and the mean $\Sigma_{\rm SFR}$ estimate for that line of sight. The histogram includes all lines of sight with $\Sigma_{\rm SFR} > 10^{-3}$ M$_\odot$ yr^{-1} kpc^{-2}. A typical scatter across the sample is 0.13 dex, which gives a rough empirical estimate of the uncertainty in individual $\Sigma_{\rm SFR}$ estimates.

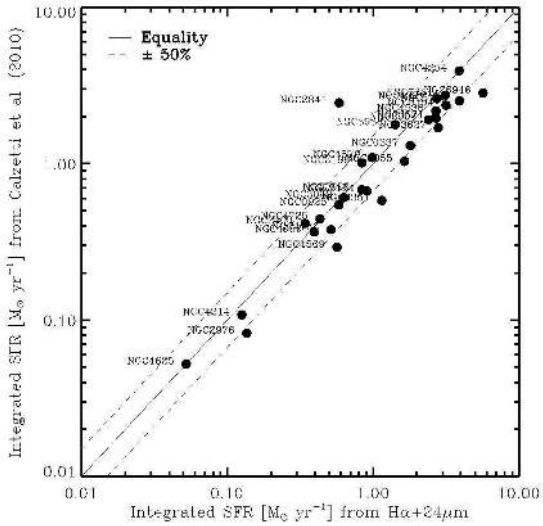

FIG. 16.— *Comparison to integrated SFRs:* Comparison of SFRs derived integrating our $\Sigma_{\rm SFR}$ (x-axis) to integrated SFRs from Calzetti et al. (2010) (y-axis). The solid line shows equality and dashed lines indicate deviations of ±50%.

tal SFR. Inasmuch as we have aimed for a self-consistent stable of tracers, this overall calibration uncertainty exists in addition to the point-by-point uncertainty derived from Figure 15.

7.1. *Limiting* $\langle\Sigma_{\rm SFR}\rangle$

Our Hα maps are unreliable below $\langle\Sigma_{\rm SFR}\rangle \lesssim 10^{-3}$ M$_\odot$ yr^{-1} kpc^{-2} and the details of the cirrus methodology dictates the 24μm distribution below this level. We therefore adopt $\Sigma_{\rm SFR} = 10^{-3}$ M$_\odot$ yr^{-1} kpc^{-2} as a limiting surface density for a robust estimate. The 24μm and FUV maps recover signal well below this value, but their translation into $\Sigma_{\rm SFR}$ becomes more uncertain. The low-$\Sigma_{\rm SFR}$ regime can help constrain many interesting astrophysical processes. Our general recommendation in this regime is to carefully focus on the constituent parts of the hybrid tracers (i.e., FUV, Hα, and 24μm separately) both as intensities and $\Sigma_{\rm SFR}$ estimates (e.g., see Bigiel et al. 2010; Schruba et al. 2011). FUV and Hα alone should provide robust lower limits to the overall $\Sigma_{\rm SFR}$.

7.2. *Comparison to Integrated Values*

A key property of well-formed $\Sigma_{\rm SFR}$ estimates that span a large part of a galaxy is that they integrate to a sensible total SFR. Figure 16 shows the results of integrating our maps, here Hα plus cirrus-corrected 24μm, and comparing them to the galaxy-average $\Sigma_{\rm SFR}$ of Calzetti et al. (2010). Note that the Calzetti et al. (2010) results are partially anchored to the Kennicutt et al. (2009) results, which we consider somewhat uncertain for these targets. The overall match appears very good given this uncertainty, with our estimates tending to be slightly higher in high SFR galaxy because of our higher adopted $w_{\rm H\alpha}$.

7.3. *Other Uncertainties*

We have attempted a thorough investigation of $\Sigma_{\rm SFR}$ estimation on kpc scales but several important uncertainties remain. We discuss these briefly here.

Diffuse Ionized Gas and Escape of Photons from H II *Regions:* Photons may escape from H II regions, producing Hα emission away from the emitting stellar population. Estimates of the fraction of such "diffuse" Hα emission in galaxies are often $\sim 30\%$ (see Rahman et al. 2010). Most such emission still reflects ionizing photons produced by massive stars and so *must* be accounted in the SFR if kpc-sized estimates are to match integrated estimates. In theory this emission should thus be added back to the likely parent region (e.g., Blanc et al. 2009) and should not be entirely removed from the map.

Given the cross section of H I to ionizing photons, the path length of ionizing photons near the Lyman limit will be extraordinarily short in the presence of any neutral gas. Despite this, diffusion over scales of a few hundred pc clearly occurs. We observe a warm ionized medium in our own Galaxy and diffuse ionized gas in other galaxies. However given that this flux must be conserved and our kpc resolution this systematic should represent a decidedly second-order concern.

Dust Absorption of Ionizing Photons: The complementary concern may also confuse our measurements. Dust inside H II regions may absorb ionizing photons before they reach a hydrogen atom. Such photons will be missed by recombination line observations, including Paα, though any bolometric tracer will account for this light as it is reradiated by the dust. Robust estimates of the magnitude of this effect remain scarce, but Inoue (2001) and Inoue et al. (2001) studied star-forming regions in the Milky Way and Local Group galaxies and suggested the dust may absorb as many as half of the ionizing photons. Calculations by Dopita et al. (2003) also suggest plausible magnitudes of several times 10% with the effect strongest for ultracompact H II regions (see also Groves et al. 2008).

We find good overall consistency between Hα-based approaches, which will be sensitive to this effect, and FUV-

based approaches, which should not be affected. However, to some degree we also calibrate the FUV-based hybrids to match the Hα-based hybrids. The bottom right panel in Figure 14 compares Hα+24μm to FUV+TIR and does reveal a bias towards higher $\Sigma_{\rm SFR}$ for the bolometric FUV+TIR tracer. The bias becomes worse at lower $\langle\Sigma_{\rm SFR}\rangle$ while we expect the opposite for dust absorption of ionizing photons. Therefore we tend to attribute the disagreement mostly to the cirrus issue, but the data could certainly be consistent with non-negligible absorption of photons. The ideal test will be to compare a robust ionizing photon production map, e.g., thermal radio continuum emission at 1–10 mm or IR recombination lines, to high resolution bolometric luminosity maps and stellar populations.

UV Emission From Older Populations: Even a relatively evolved population may still produce some FUV emission, contaminating our $\Sigma_{\rm SFR}$ estimates. We estimate potential contamination by measuring the ratio of FUV to median-filtered 3.6μm emission, an approximate tracer of stellar mass (see appendices in Leroy et al. 2008), in regions that appear dominated by old stellar populations. We measure ratios for the bulges of M 81, M 94 ("the Sombrero"), NGC 4725, and NGC 3351[16], all of which show bright stellar structures with little evidence of current star formation. We also measure the ratio across our sample for all lines of sight with very low star formation, $\langle\Sigma_{\rm SFR}\rangle < 5 \times 10^{-4}$ M$_\odot$ yr^{-1} kpc^{-2}, but significant stellar mass, $\Sigma_* \gtrsim 100$ M$_\odot$ pc^{-2}. These all suggest a ratio $I_{\rm FUV}/\Sigma_* \sim 0.7$–$1.9 \times 10^{-5}$ MJy sr^{-1} (M$_\odot$ pc^{-2})$^{-1}$.

We test the effect of correcting the FUV or $\Sigma_{\rm SFR}$ maps using a ratio at the upper end of this range, 2×10^{-5} MJy sr^{-1} (M$_\odot$ pc^{-2})$^{-1}$. Our adopted mass-to-light ratio is

$$\Sigma_* \left[\mathrm{M}_\odot\ \mathrm{kpc}^{-2}\right] = 200\ I_{3.6}\ \mathrm{MJy\ sr}^{-1}\ , \qquad (13)$$

similar to Leroy et al. (2008), though revised slightly to match the maps of Zibetti et al. (2009). Therefore this ratio corresponds to $I_{\rm FUV}\left[\mathrm{MJy\ sr}^{-1}\right] \sim 0.004\ \mathrm{I}_{3.6}\left[\mathrm{MJy\ sr}^{-1}\right]$. From Equation 6 the implied contamination in units of $\Sigma_{\rm SFR}$ will be

$$\Sigma_{\rm SFR}^{old\ UV}\left[\mathrm{M}_\odot\ \mathrm{yr}^{-1}\ \mathrm{kpc}^{-2}\right] \approx 1.6 \times 10^{-6}\ \Sigma_*\left[\mathrm{M\ pc}^{-2}\right]\ . \qquad (14)$$

Equation 14 implies that observations of stellar bulges ($\Sigma_* \gtrsim 10^2$ M$_\odot$ pc^{-2}) that measure $\Sigma_{\rm SFR}$ only a few times 10^{-4} M$_\odot$ yr^{-1} kpc^{-2} should be viewed with suspicion. The contamination will be lower in the outer disks of galaxies ($\Sigma_* \sim 10$ M$_\odot$ pc^{-2}) in proportion to the lower stellar surface density. However, for our sample and working $\Sigma_{\rm SFR}$ limit the contribution of this truly old UV component can be safely neglected. The SFR associated with FUV emission from old stars appears to be only $\approx$ 3% of the total SFR where $\Sigma_{\rm SFR} > 10^{-3}$ M$_\odot$ yr^{-1} kpc^{-2} and contributes only $\approx 10\%$ of the FUV light.

Contributions from intermediate age populations represent a more complex problem requiring detailed stellar population analysis (a more complex extension of Section 3) that is beyond the scope of this paper.

[16] M 81 and M 94 are otherwise not included in this paper.

Stochasticity and IMF Variations: At 1 kpc resolution we expect to average several star-forming regions in each element. For $\Sigma_{\rm SFR} > 10^{-3}$ M$_\odot$ yr^{-1} kpc^{-2}, we expect $M_* \gtrsim 5 \times 10^3$ M$_\odot$ formed over the last $\sim$ 5 Myr in each element. This minimizes but does not completely eliminate concerns about sampling the stellar initial mass function (IMF). Changes in the IMF will directly impact our estimates but concrete evidence for such variations remains amibiguous at best (Bastian et al. 2010). We do not consider either effect.

8. DISCUSSION

8.1. *Hybrid SFR Tracers*

Hybrid tracers that combine an unobscured and an obscured (i.e., IR) component have many advantages. The two tracers complement one another, yielding an approach that can apply, in principle, to a wide range of environments. Maps of UV, Hα, and IR emission are widely available. IR emission directly probes reprocessed photons, avoiding the need for less reliable extinction tracers. Even given the uncertainty in the IR term calibration, using a direct measure of reprocessed starlight makes for much more robust approaches than optical, UV, or gas-based approaches. Tracers constructed from linear combinations of these bands will be reasonably scale-independent and can be easily interpreted. Despite the significant uncertainties discussed in this paper, we argue that hybrid IR+UV or IR+Hα tracers do offer the best current combination of widely available data and robustness.

24μm Cirrus: The issue of infrared "cirrus", emission due to heating by an older stellar population, remains a challenge for IR-based SFR estimates. Here we have suggested an approach based on physical dust models, with the cirrus emission mainly dependent on the dust abundance and illuminating radiation field. Several points emerge from our calculation. First, cirrus emission associated with molecular gas can make an important contribution especially in the bright parts of star-forming galaxies. This is emission from dust mixed with molecular gas but heated by weak radiation fields. Because the dust emitting in such a component is mixed with the clumpy molecular ISM this contribution may easily be missed by morphological approaches (e.g., median filtering) designed to reject a smooth component.

Second, estimating the radiation field $U_{\rm cirrus}$ that is not associated with recent star formation is challenging. Doing so one must be careful to both avoid oversubtraction and catch all of the cirrus. We present a detailed attempt to estimate the appropriate U. Important checks on this quantity will come from high resolution fits to the dust SED in quiescent regions. Though not totally trivial to interpret, these will help inform our understanding of the "non-star-forming" U in galaxies. Our sample has been observed by the *Herschel* Key Program KINGFISH at higher resolution and we expect follow-up analyses to further illuminate this issue. Finally, though the IR-cirrus represents an important issue one must bear in mind that other systematics with similar magnitude persist, including the absolute calibration of the IR term in hybrid tracers, losses of ionizing photons due to dust or escape, and departures from the "continuous star formation" approximation that underlies the whole concept of

star formation rates.

Calibration and the Need For A Sample of Wide-Field, Extinction-Robust $\Sigma_{\rm SFR}$ Maps: We have shown that substantial calibration uncertainties still plague the IR portion of hybrid SFR tracers. These lingering uncertainties and the other systematics we discuss highlight the pressing need for wide-field, extinction-robust maps of the distribution of recent star formation. Though observationally expensive, such maps are indispensible to calibrate more widely used tracers like those we discuss here. Wide-field maps are a necessity because understanding galaxy evolution requires $\Sigma_{\rm SFR}$ estimates that span whole galaxies, which in turn require understanding faint regions and characterizing diffuse emission, not only studying H II peaks. Perhaps the best prospect for a large sample of such maps is using ALMA, the EVLA, or the GBT to map thermal radio continuum emission at 1–10 mm (Niklas et al. 1997; Murphy et al. 2011). Such maps avoid extinction concerns completely and can reveal the distribution of ionizing photons in galaxies in exquisite detail.

Other Uncertainties and Limiting Returns: We have noted several other important uncertainties: escape of ionizing photons from H II regions, absorption of ionizing photons by dust, contribution of an intermediate age stellar population, stochasticity or IMF variations, and the closely related age of discrete stellar populations. Several of these have a likely magnitude $\approx 10\%$ and remain difficult to constrain. As an ensemble these suggest that one should bear an uncertainty of at least a few times 10% for any star formation rate estimates. Indeed at small scales the age-based scatter we discuss implies that the very concept of a star formation rate will not be precise beyond this level.

8.2. *Recommended Approach*

We recommend estimating $\Sigma_{\rm SFR}$ at $\sim$kpc resolution over the range 10^{-3} M$_\odot$ yr^{-1} kpc^{-2} $< \Sigma_{\rm SFR} <$ 10^{-1} M$_\odot$ yr^{-1} kpc^{-2} in the following way. Use the broadband dust SED along with the models of Draine & Li (2007) to estimate $\Sigma_{\rm dust}$, $U_{\rm min}$, and $q_{\rm PAH}$. The empirical fits of Muñoz-Mateos et al. (2009a) may offer a helpful simplification or check. Derive the 24μm emissivity per unit dust mass for $U_{\rm cirrus} = 0.5\ U_{\rm min}$[17] from the Draine & Li (2007) models and subtract this emissivity times $\Sigma_{\rm dust}$ from the observed 24μm map (setting negative regions to have $I_{24} = 0$). If using only *Spitzer* data, gas maps and the assumption of a weakly varying DGR can provide a useful way to work at resolution higher than the *Spitzer* 160μm PSF. Combine the resulting 24μm intensity with an unobscured tracer, either Hα (Equation 4) or FUV (Equation 6) emission, using $w_{\rm H\alpha} = 1.3$ or $w_{\rm FUV} = 1.7$, respectively (Equation 9).

One may also attempt to correct the FUV for contamination by emission from old stars. Based on the colors of bulges and low-$\Sigma_{\rm SFR}$, high Σ_* regions we suggest correcting the FUV-related term in proportion to the old stellar population by $\Sigma_{\rm SFR} = 1.6 \times 10^{-6}\ \Sigma_*$ (Equation 14). In our sample we find this correction to have a small impact, but caution that it only accounts for old populations.

This approach removes a physically plausible, locally estimated cirrus component. It is quantitatively and qualitatively consistent with other approaches over the range 10^{-3} M$_\odot$ yr^{-1} kpc^{-2} $\leq \Sigma_{\rm SFR} \leq$ 10^{-1} M$_\odot$ yr^{-1} kpc^{-2}. It yields maps that integrate into sensible integrated SFR maps. We suggest an uncertainty of $\sim$ 0.15 dex in individual measurements, $\sim$ 0.3 dex in the calibration of the 24μm term for any given system, and $\sim$ 0.15 dex for the average calibration of the 24μm term.

In the Absence of Long-Wavelength IR Data: If one has only gas, 24μm, and Hα or FUV data one can still attempt a first-order cirrus estimate. Across our sample, 24μm emissivity per unit gas mass normalized to $U = 0.6$ and $DGR = 0.01$ is

$$I_{24}\ (U \approx 0.6, DGR \approx 0.01)\left[\text{MJy sr}^{-1}\right] \approx 1.2{\times}10^{-2}\,\Sigma_{\rm gas}\ \left[\text{M pc}^{-2}\right] \quad (15)$$

Where the gas surface density, $\Sigma_{\rm gas}$, combines H I and H_2 and includes a contribution from helium. Taking a typical cirrus U field and DGR one can then attempt a somewhat less rigorous cirrus correction and proceed as above.

If only H I data are present these can be used for a partial correction following the methodology above. In this case, we suggest a lower $w_{\rm H\alpha} = 1.0$ or $w_{\rm FUV} = 1.3$. This will somewhat offset the lack of correction for cirrus associated with H_2.

Note that these suggestions assume the typical dust-to-gas ratio for our sample. For low-luminosity, low-metallicity systems the expected cirrus emission will be lower by a factor that is to first-order proportional to the metallicity.

With No Multiwavelength Data: In the absence of multiwavelength data one can leverage the fact that in star-forming galaxies the deprojected H I surface density, $\Sigma_{\rm HI}$, appears relatively flat. Across our data the median $\Sigma_{\rm HI} \approx 6$ M$_\odot$ pc^{-2} with a factor of 2 scatter. In the absence of any knowledge of the gas distribution and provided that one is studying a "normal" $z = 0$ star-forming galaxy, adopting $\Sigma_{\rm HI} \sim 6$ M$_\odot$ pc^{-2} and then proceeding as above will allow a rough cirrus correction.

8.3. *Implication for SFR-Gas Comparisons*

Our calculations have several implications for measurements of the relationship between gas and star formation in galaxies. The most basic implication is that we find broad consistency among different estimates of $\Sigma_{\rm SFR}$ at kpc resolution across a sample of 30 nearby galaxies. We demonstrate sensible scaling relations among hybrid tracer components, motivate a physical approach to separate 24μm emission not associated with star formation, and verify the calibration of the IR component of hybrid tracers for our approach.

Calibration Uncertainty and Gas Depletion Time: The uncertainty in the absolute calibration of the dominant 24μm term implies a corresponding uncertainty in the ratio of gas to star formation. This quantity can be phrased as the gas depletion time, $\tau_{\rm Dep} = M_{\rm gas}/{\rm SFR}$, or its inverse, the star formation efficiency SFE $= SFR/M_{\rm gas}$. In either case, our factor of $\approx$ 1.5 uncertainty on the 24μm term in a hybrid SFR estimate implies an uncertainty of $\approx$ 25% on the absolute determination of the SFR and thus the ratio. Comparison to integrated SFRs

[17] At very different resolution than this study, $U_{\rm cirrus} \approx 0.6$ may be a safer choice.

from Calzetti et al. (2010) bears out this estimate; these differ from our estimates only in treatment and calibration of the IR emission and display a median $\approx 11\%$ offset with $\approx 30\%$ scatter. This uncertainty will be compounded by other uncertainties in physical parameter estimation: the CO-to-H_2 conversion factor, H I opacity, stellar initial mass function, adopted star formation history, etc. However, as this is a calibration uncertainty, one should still be able to carry out internally consistent comparisons below this level.

Uncertainty in Scaling Relations: From intercomparison of tracers we find that the systematic "tilt" among $\Sigma_{\rm SFR}$ estimates does not exceed 0.3 dex across the range $10^{-3} < \langle\Sigma_{\rm SFR}\rangle < 10^{-1}$ M$_\odot$ yr^{-1} kpc^{-2} and is usually substantially lower. Here "tilt" means systematic change in the ratio of a pair of $\Sigma_{\rm SFR}$ estimates across this range. The systematic uncertainty in the index of any power law scaling relation involving $\Sigma_{\rm SFR}$ will be $\sim$ tilt/Δx where Δx is the dynamic range of the other, non-$\Sigma_{\rm SFR}$ variable over the range $10^{-3} < \langle\Sigma_{\rm SFR}\rangle < 10^{-1}$ M$_\odot$ yr^{-1} kpc^{-2}. If $\Sigma_{\rm SFR} \sim x^n$ then the uncertainty in the the index n due to choice of $\Sigma_{\rm SFR}$ esimate will be $\sim 0.15 \times n$. Thus for any nearly linear relationship (e.g., $\Sigma_{\rm SFR}$ vs. $\Sigma_{\rm H2}$, Bigiel et al. 2008, 2011), the implied uncertainty in the power law index due to uncertainty in $\Sigma_{\rm SFR}$ is ~ 0.15. For a steeper relationship like the $\Sigma_{\rm SFR} \sim \Sigma_{\rm HI}^2$ found in the outer parts of galaxies (Bigiel et al. 2010) the implied uncertainty is ~ 0.3. The normalization of the scaling relation will have the overall calibration uncertainty already discussed.

Small-Scale Scatter in Scaling Relations: High resolution observations and simulations have begun to consider the scatter in the ratios of SFR tracers to gas as a function of scale (Schruba et al. 2010; Onodera et al. 2010; Feldmann et al. 2011). This scatter encodes key information on the evolution of star forming regions, the small scale correlation of star formation, and intrinsic variations in the star formation efficiency. On the scale of individual clouds or clusters, one cannot escape the fact that star formation occurs in discrete events. We considered the intrinsic scatter in Hα or FUV emission from the same population at different, but still young, ages. These suggest that as one isolates individual populations one will find intrinsic scatter ~ 0.3 dex in Hα intensities and ~ 0.45 dex in FUV intensity for otherwise identical regions with different ages and ~ 0.5 dex scatter. This scatter represents a minimum and will be compounded by any uncertainties in the estimation of gas mass and extinction or evolution of the region. The limited measurements available so far appear consistent with these rough calculations (see also Blanc et al. 2009).

9. SUMMARY

We estimate the surface density of recent star formation, $\Sigma_{\rm SFR}$, at 1 kpc resolution in the HERACLES sample and examine the underpinnings of empirical hybrid tracers (Hα+24μm and FUV+24μm). We look at the magnitudes and correlations among constituent parts of the hybrid tracers and consider the effects of discrete events on the derivation of SFRs. Using dust models and multiwavelength data, we make a physically motivated estimate of the contamination of the 24μm band by emission not associated with star formation. Benchmarking to reference SFRs drawn from the literature we derive the appropriate calibration to use 24μm with Hα or FUV given our cirrus approach and physical resolution. We then compare a wide range of $\Sigma_{\rm SFR}$ estimates and check the integrated SFRs for our targets. We present our recommended approach and discuss uncertainties and implications for SFR-gas comparisons.

We highlight the following points:

1. Starburst99 simulations of an evolving single stellar population imply an intrinsic scatter of ~ 0.3 dex in Hα-based SFR estimates and ~ 0.5 dex in FUV based SFR estimates when isolating a single stellar population.

2. We use the dust models of Draine & Li (2007) to make physical estimates of the 24μm unassociated with star formation. These models suggest that emission along a line of sight depends weakly on the PAH mass fraction and linearly on both the dust-to-gas ratio, gas column density, and the radiation field not associated with recent star formation.

3. By maximizing the impact of the cirrus subtraction on low-lying emission without oversubtracting we find $U_{\rm cirrus} \approx 0.5\ U_{\rm min}$ to be an appropriate radiation field not associated with recent star formation. Here $U_{\rm min}$ is the fixed, pervasive radiation field illuminating all dust derived from fitting the Draine & Li (2007) models. Our best-fit field has typical magnitude $U = 0.6$ times the solar neighborhood interstellar radiation field. The resulting cirrus subtraction removes $\approx 20\%$ of the 24μm, on average, across our sample.

4. Subtracting only cirrus emitted by dust associated with H I does not offer an appreciable correction in the parts of galaxies where most star formation occurs. IR cirrus from molecular gas must represent an important term, especially given that most dust is mixed with molecular gas in the inner, H_2 dominated parts of spiral galaxies. This emission will likely exhibit the same clumpy morphology as CO emission, making it difficult to estimate using image processing techniques.

5. Lack of a robust, wide-field reference SFR renders the absolute calibration and universality of the 24μm term in hybrid tracers like Hα+24μm and FUV+24μm uncertain, even for the well-studied SINGS sample. We demonstrate this uncertainty in both the SINGS literature and our own measurements.

6. Although there is substantial scatter in the available reference SFRs, we verify the appropriate calibration for the 24μm portion of Hα- and UV-based hybrid tracers for our cirrus approach and 1 kpc resolution. Based on references to literature extinction and SFR estimates, we recommend $w_{\rm H\alpha} = 1.3$ and $w_{\rm FUV} = 1.7$ for our resolution and cirrus approach. We arrive at the FUV calibration referencing to both Hα+24μm and the FUV+TIR approach of Cortese et al. (2008). The latter means that the FUV+24μm approach is not only derived from the Hα+24μm calibration.

7. A wide variety of UV, Hα, and IR-based approaches to estimate $\Sigma_{\rm SFR}$ at 1 kpc resolution yield results with systematic disagreement of a factor of 2 or less above $\Sigma_{\rm SFR} = 10^{-3}$ M$_\odot$ yr^{-1} kpc^{-2}.

8. Below $\Sigma_{\rm SFR} = 10^{-3}$ M$_\odot$ yr^{-1} kpc^{-2} the Hα data become unreliable and our results depend strongly on the adopted approach to the IR cirrus. We recommend this value as a useful lower limit for robust $\Sigma_{\rm SFR}$ estimation using hybrid tracers. Studies targeting lower levels should carefully consider the constituent terms.

Our work also has implications for SFR-gas comparisons, which have heavily leveraged these tracers. We emphasize the requirement that a well-constructed $\Sigma_{\rm SFR}$ map integrate to a sensible SFR and note:

1. The uncertainty in the calibration of the 24μm term implies a corresponding uncertainty in the gas depletion time, $\tau_{\rm dep} = M_{\rm gas}/{\rm SFR}$, of $\approx 25\%$.

2. Systematic variations among tracers are less than 0.3 dex over the range $10^{-3} < \langle\Sigma_{\rm SFR}\rangle < 10^{-1}$ M$_\odot$ yr^{-1} kpc^{-2}. Over this range, the implied uncertainty in the power law slope of any scaling relation $\Sigma_{\rm SFR} \sim x^n$ will be $\leq 0.15 \times n$.

3. We expect an intrinsic SFR scatter of $\sim$ 0.3 dex (Hα) – 0.5 dex (FUV) to emerge at small scales due to age effects. Observations that isolate single stellar populations should observe such scatter.

We thank the referee for a detailed, constructive report that improved the quality of this paper. We thank the *GALEX* NGS, SINGS, and LVL teams for making their outstanding datasets available. We acknowledge helpful correspondence and discussion with K.-F. Schuster, R. C. Kennicutt, J. Moustakas, S. Schnee, and K. Sheth. We thank staff of the IRAM 30m for their assistance carrying out the HERACLES survey. We thank Deidre Hunter for sharing her Hα image of NGC 4214. F.B., A.K.L., and F.W. gratefully acknowledge the Aspen Center for Physics, where part of this work was carried out. Support for A.K.L. for part of this project was provided by NASA through Hubble Fellowship grant HST-HF-51258.01-A awarded by the Space Telescope Science Institute, which is operated by the Association of Universities for Research in Astronomy, Inc., for NASA, under contract NAS 5-26555. J.C.M.M. acknowledges financial support from NASA JPL/*Spitzer* grant RSA 1374189 provided for the S4G project. A.B. wishes to acknowledge support from NSF AST-0955836 and a Cottrell Scholar award from the Research Corporation for Science Advancement. We have made use of the Extragalactic Database (NED), which is operated by the Jet Propulsion Laboratory, California Institute of Technology, under contract with the National Aeronautics and Space Administration. We also acknowledge use of the Lyon Extragalactic Database (LEDA) and NASA's Astrophysics Data System (ADS). The National Radio Astronomy Observatory is a facility of the National Science Foundation operated under cooperative agreement by Associated Universities, Inc.

REFERENCES

Abdo, A. A., Ackermann, M., Ajello, M., Baldini, L., Ballet, J., Barbiellini, G., Bastieri, D., Baughman, B. M., Bechtol, K., Bellazzini, R., Berenji, B., Bloom, E. D., Bonamente, E., Borgland, A. W., Bregeon, J., Brez, A., Brigida, M., Bruel, P., Burnett, T. H., Buson, S., Caliandro, G. A., Cameron, R. A., Caraveo, P. A., Casandjian, J. M., Cecchi, C., Çelik, Ö., Chekhtman, A., Cheung, C. C., Chiang, J., Ciprini, S., Claus, R., Cohen-Tanugi, J., Cominsky, L. R., Conrad, J., Dermer, C. D., de Palma, F., Digel, S. W., Silva, E. d. C. e., Drell, P. S., Dubois, R., Dumora, D., Farnier, C., Favuzzi, C., Fegan, S. J., Focke, W. B., Fortin, P., Frailis, M., Fukazawa, Y., Funk, S., Fusco, P., Gargano, F., Gehrels, N., Germani, S., Giavitto, G., Giebels, B., Giglietto, N., Giordano, F., Glanzman, T., Godfrey, G., Grenier, I. A., Grondin, M., Grove, J. E., Guillemot, L., Guiriec, S., Harding, A. K., Hayashida, M., Horan, D., Hughes, R. E., Jackson, M. S., Jóhannesson, G., Johnson, A. S., Johnson, W. N., Kamae, T., Katagiri, H., Kataoka, J., Kawai, N., Kerr, M., Knödlseder, J., Kuss, M., Lande, J., Latronico, L., Lemoine-Goumard, M., Longo, F., Loparco, F., Lott, B., Lovellette, M. N., Lubrano, P., Makeev, A., Mazziotta, M. N., McEnery, J. E., Meurer, C., Michelson, P. F., Mitthumsiri, W., Mizuno, T., Monte, C., Monzani, M. E., Morselli, A., Moskalenko, I. V., Murgia, S., Nolan, P. L., Norris, J. P., Nuss, E., Ohsugi, T., Okumura, A., Omodei, N., Orlando, E., Ormes, J. F., Paneque, D., Pelassa, V., Pepe, M., Pesce-Rollins, M., Piron, F., Porter, T. A., Rainò, S., Rando, R., Razzano, M., Reimer, A., Reimer, O., Reposeur, T., Rodriguez, A. Y., Ryde, F., Sadrozinski, H., Sanchez, D., Sander, A., Saz Parkinson, P. M., Sgrò, C., Siskind, E. J., Smith, P. D., Spandre, G., Spinelli, P., Starck, J., Strickman, M. S., Strong, A. W., Suson, D. J., Takahashi, H., Tanaka, T., Thayer, J. B., Thayer, J. G., Thompson, D. J., Tibaldo, L., Torres, D. F., Tosti, G., Tramacere, A., Uchiyama, Y., Usher, T. L., Vasileiou, V., Vilchez, N., Vitale, V., Waite, A. P., Wang, P., Winer, B. L., Wood, K. S., Ylinen, T., & Ziegler, M. 2010, ApJ, 710, 133

Alonso-Herrero, A., Rieke, G. H., Rieke, M. J., Colina, L., Pérez-González, P. G., & Ryder, S. D. 2006, ApJ, 650, 835

Bastian, N., Covey, K. R., & Meyer, M. R. 2010, ARA&A, 48, 339

Bigiel, F., Bolatto, A., Leroy, A., Blitz, L., Walter, F., Rosolowsky, E., Lopez, L., & Plambeck, R. 2010, ArXiv e-prints

Bigiel, F., Leroy, A., Walter, F., Brinks, E., de Blok, W. J. G., Madore, B., & Thornley, M. D. 2008, AJ, 136, 2846

Bigiel, F., Leroy, A. K., Walter, F., Brinks, E., de Blok, W. J. G., Kramer, C., Rix, H. W., Schruba, A., Schuster, K.-F., Usero, A., & Wiesemeyer, H. W. 2011, ApJ, 730, L13+

Blanc, G. A., Heiderman, A., Gebhardt, K., Evans, N. J., & Adams, J. 2009, ApJ, 704, 842

Boselli, A., & Gavazzi, G. 2002, A&A, 386, 124

Boulanger, F., Abergel, A., Bernard, J.-P., Burton, W. B., Desert, F.-X., Hartmann, D., Lagache, G., & Puget, J.-L. 1996, A&A, 312, 256

Buat, V. 1992, A&A, 264, 444

Calzetti, D., Kennicutt, R. C., Engelbracht, C. W., Leitherer, C., Draine, B. T., Kewley, L., Moustakas, J., Sosey, M., Dale, D. A., Gordon, K. D., Helou, G. X., Hollenbach, D. J., Armus, L., Bendo, G., Bot, C., Buckalew, B., Jarrett, T., Li, A., Meyer, M., Murphy, E. J., Prescott, M., Regan, M. W., Rieke, G. H., Roussel, H., Sheth, K., Smith, J. D. T., Thornley, M. D., & Walter, F. 2007, ApJ, 666, 870

Calzetti, D., Kennicutt, Jr., R. C., Bianchi, L., Thilker, D. A., Dale, D. A., Engelbracht, C. W., Leitherer, C., Meyer, M. J., Sosey, M. L., Mutchler, M., Regan, M. W., Thornley, M. D., Armus, L., Bendo, G. J., Boissier, S., Boselli, A., Draine, B. T., Gordon, K. D., Helou, G., Hollenbach, D. J., Kewley, L., Madore, B. F., Martin, D. C., Murphy, E. J., Rieke, G. H., Rieke, M. J., Roussel, H., Sheth, K., Smith, J. D., Walter, F., White, B. A., Yi, S., Scoville, N. Z., Polletta, M., & Lindler, D. 2005, ApJ, 633, 871

Calzetti, D., Kinney, A. L., & Storchi-Bergmann, T. 1994, ApJ, 429, 582

Calzetti, D., Wu, S., Hong, S., Kennicutt, R. C., Lee, J. C., Dale, D. A., Engelbracht, C. W., van Zee, L., Draine, B. T., Hao, C., Gordon, K. D., Moustakas, J., Murphy, E. J., Regan, M., Begum, A., Block, M., Dalcanton, J., Funes, J., Gil de Paz, A., Johnson, B., Sakai, S., Skillman, E., Walter, F., Weisz, D., Williams, B., & Wu, Y. 2010, ApJ, 714, 1256
Cardelli, J. A., Clayton, G. C., & Mathis, J. S. 1989, ApJ, 345, 245
Chabrier, G. 2003, PASP, 115, 763
Cortese, L., Boselli, A., Franzetti, P., Decarli, R., Gavazzi, G., Boissier, S., & Buat, V. 2008, MNRAS, 386, 1157
Dale, D. A., Cohen, S. A., Johnson, L. C., Schuster, M. D., Calzetti, D., Engelbracht, C. W., Gil de Paz, A., Kennicutt, R. C., Lee, J. C., Begum, A., Block, M., Dalcanton, J. J., Funes, J. G., Gordon, K. D., Johnson, B. D., Marble, A. R., Sakai, S., Skillman, E. D., van Zee, L., Walter, F., Weisz, D. R., Williams, B., Wu, S., & Wu, Y. 2009, ApJ, 703, 517
Dale, D. A., Gil de Paz, A., Gordon, K. D., Hanson, H. M., Armus, L., Bendo, G. J., Bianchi, L., Block, M., Boissier, S., Boselli, A., Buckalew, B. A., Buat, V., Burgarella, D., Calzetti, D., Cannon, J. M., Engelbracht, C. W., Helou, G., Hollenbach, D. J., Jarrett, T. H., Kennicutt, R. C., Leitherer, C., Li, A., Madore, B. F., Martin, D. C., Meyer, M. J., Murphy, E. J., Regan, M. W., Roussel, H., Smith, J. D. T., Sosey, M. L., Thilker, D. A., & Walter, F. 2007, ApJ, 655, 863
Dame, T. M., Hartmann, D., & Thaddeus, P. 2001, ApJ, 547, 792
Dopita, M. A., Groves, B. A., Sutherland, R. S., & Kewley, L. J. 2003, ApJ, 583, 727
Draine, B. T., Dale, D. A., Bendo, G., Gordon, K. D., Smith, J. D. T., Armus, L., Engelbracht, C. W., Helou, G., Kennicutt, Jr., R. C., Li, A., Roussel, H., Walter, F., Calzetti, D., Moustakas, J., Murphy, E. J., Rieke, G. H., Bot, C., Hollenbach, D. J., Sheth, K., & Teplitz, H. I. 2007, ApJ, 663, 866
Draine, B. T., & Li, A. 2007, ApJ, 657, 810
Feldmann, R., Gnedin, N. Y., & Kravtsov, A. V. 2011, ApJ, 732, 115
Galliano, F., Hony, S., Bernard, J. ., Bot, C., Madden, S. C., Roman-Duval, J., Galametz, M., Li, A., Meixner, M., Engelbracht, C. W., Lebouteiller, V., Misselt, K., Montiel, E., Panuzzo, P., Reach, W. T., & Skibba, R. 2011, ArXiv e-prints
Gavazzi, G., Boselli, A., Donati, A., Franzetti, P., & Scodeggio, M. 2003, A&A, 400, 451
Genzel, R., Tacconi, L. J., Gracia-Carpio, J., Sternberg, A., Cooper, M. C., Shapiro, K., Bolatto, A., Bouché, N., Bournaud, F., Burkert, A., Combes, F., Comerford, J., Cox, P., Davis, M., Schreiber, N. M. F., Garcia-Burillo, S., Lutz, D., Naab, T., Neri, R., Omont, A., Shapley, A., & Weiner, B. 2010, MNRAS, 407, 2091
Gil de Paz, A., Boissier, S., Madore, B. F., Seibert, M., Joe, Y. H., Boselli, A., Wyder, T. K., Thilker, D., Bianchi, L., Rey, S.-C., Rich, R. M., Barlow, T. A., Conrow, T., Forster, K., Friedman, P. G., Martin, D. C., Morrissey, P., Neff, S. G., Schiminovich, D., Small, T., Donas, J., Heckman, T. M., Lee, Y.-W., Milliard, B., Szalay, A. S., & Yi, S. 2007, ApJS, 173, 185
Gini, C. 1912, Memorie di Metodologia Statistica, ed. E. Pizetti & Ti. Selvemini
Greenawalt, B., Walterbos, R. A. M., Thilker, D., & Hoopes, C. G. 1998, ApJ, 506, 135
Groves, B., Dopita, M. A., Sutherland, R. S., Kewley, L. J., Fischera, J., Leitherer, C., Brandl, B., & van Breugel, W. 2008, ApJS, 176, 438
Helfer, T. T., Thornley, M. D., Regan, M. W., Wong, T., Sheth, K., Vogel, S. N., Blitz, L., & Bock, D. C.-J. 2003, ApJS, 145, 259
Helou, G., Roussel, H., Appleton, P., Frayer, D., Stolovy, S., Storrie-Lombardi, L., Hurt, R., Lowrance, P., Makovoz, D., Masci, F., Surace, J., Gordon, K. D., Alonso-Herrero, A., Engelbracht, C. W., Misselt, K., Rieke, G., Rieke, M., Willner, S. P., Pahre, M., Ashby, M. L. N., Fazio, G. G., & Smith, H. A. 2004, ApJS, 154, 253
Heyer, M., Krawczyk, C., Duval, J., & Jackson, J. M. 2009, ApJ, 699, 1092
Hoopes, C. G., Walterbos, R. A. M., & Bothun, G. D. 2001, ApJ, 559, 878
Hunter, D. A., & Elmegreen, B. G. 2004, AJ, 128, 2170
Inoue, A. K. 2001, AJ, 122, 1788
Inoue, A. K., Hirashita, H., & Kamaya, H. 2001, ApJ, 555, 613
Kennicutt, R. C., Calzetti, D., Aniano, G., Appleton, P., Armus, L., Beirão, P., Bolatto, A. D., Brandl, B., Crocker, A., Croxall, K., Dale, D. A., Meyer, J. D., Draine, B. T., Engelbracht, C. W., Galametz, M., Gordon, K. D., Groves, B., Hao, C.-N., Helou, G., Hinz, J., Hunt, L. K., Johnson, B., Koda, J., Krause, O., Leroy, A. K., Li, Y., Meidt, S., Montiel, E., Murphy, E. J., Rahman, N., Rix, H.-W., Roussel, H., Sandstrom, K., Sauvage, M., Schinnerer, E., Skibba, R., Smith, J. D. T., Srinivasan, S., Vigroux, L., Walter, F., Wilson, C. D., Wolfire, M., & Zibetti, S. 2011, PASP, 123, 1347
Kennicutt, R. C., Hao, C., Calzetti, D., Moustakas, J., Dale, D. A., Bendo, G., Engelbracht, C. W., Johnson, B. D., & Lee, J. C. 2009, ApJ, 703, 1672
Kennicutt, Jr., R. C. 1998, ARA&A, 36, 189
Kennicutt, Jr., R. C., Armus, L., Bendo, G., Calzetti, D., Dale, D. A., Draine, B. T., Engelbracht, C. W., Gordon, K. D., Grauer, A. D., Helou, G., Hollenbach, D. J., Jarrett, T. H., Kewley, L. J., Leitherer, C., Li, A., Malhotra, S., Regan, M. W., Rieke, G. H., Rieke, M. J., Roussel, H., Smith, J.-D. T., Thornley, M. D., & Walter, F. 2003, PASP, 115, 928
Kennicutt, Jr., R. C., Calzetti, D., Walter, F., Helou, G., Hollenbach, D. J., Armus, L., Bendo, G., Dale, D. A., Draine, B. T., Engelbracht, C. W., Gordon, K. D., Prescott, M. K. M., Regan, M. W., Thornley, M. D., Bot, C., Brinks, E., de Blok, E., de Mello, D., Meyer, M., Moustakas, J., Murphy, E. J., Sheth, K., & Smith, J. D. T. 2007, ApJ, 671, 333
Kennicutt, Jr., R. C., Lee, J. C., Funes, José G., S. J., Sakai, S., & Akiyama, S. 2008, ApJS, 178, 247
Knapen, J. H., Stedman, S., Bramich, D. M., Folkes, S. L., & Bradley, T. R. 2004, A&A, 426, 1135
Kroupa, P. 2001, MNRAS, 322, 231
Kuno, N., Sato, N., Nakanishi, H., Hirota, A., Tosaki, T., Shioya, Y., Sorai, K., Nakai, N., Nishiyama, K., & Vila-Vilaró, B. 2007, PASJ, 59, 117
Law, K.-H., Gordon, K. D., & Misselt, K. A. 2011, ApJ, 738, 124
Lawton, B., Gordon, K. D., Babler, B., Block, M., Bolatto, A. D., Bracker, S., Carlson, L. R., Engelbracht, C. W., Hora, J. L., Indebetouw, R., Madden, S. C., Meade, M., Meixner, M., Misselt, K., Oey, M. S., Oliveira, J. M., Robitaille, T., Sewilo, M., Shiao, B., Vijh, U. P., & Whitney, B. 2010, ApJ, 716, 453
Lee, M.-Y., Stanimirovic, S., Douglas, K. A., Knee, L. B. G., Di Francesco, J., Gibson, S. J., Begum, A., Grcevich, J., Heiles, C., Korpela, E. J., Leroy, A. K., Peek, J. E. G., Pingel, N., Putman, M. E., & Saul, D. 2011, ArXiv e-prints
Leitherer, C., Schaerer, D., Goldader, J. D., González Delgado, R. M., Robert, C., Kune, D. F., de Mello, D. F., Devost, D., & Heckman, T. M. 1999, ApJS, 123, 3
Leroy, A. K., Bolatto, A., Bot, C., Engelbracht, C. W., Gordon, K., Israel, F. P., Rubio, M., Sandstrom, K., & Stanimirović, S. 2009, ApJ, 702, 352
Leroy, A. K., Bolatto, A., Gordon, K., Sandstrom, K., Gratier, P., Rosolowsky, E., Engelbracht, C. W., Mizuno, N., Corbelli, E., Fukui, Y., & Kawamura, A. 2011, ArXiv e-prints
Leroy, A. K., Walter, F., Brinks, E., Bigiel, F., de Blok, W. J. G., Madore, B., & Thornley, M. D. 2008, AJ, 136, 2782
Martin, D. C., Fanson, J., Schiminovich, D., Morrissey, P., Friedman, P. G., Barlow, T. A., Conrow, T., Grange, R., Jelinsky, P. N., Milliard, B., Siegmund, O. H. W., Bianchi, L., Byun, Y.-I., Donas, J., Forster, K., Heckman, T. M., Lee, Y.-W., Madore, B. F., Malina, R. F., Neff, S. G., Rich, R. M., Small, T., Surber, F., Szalay, A. S., Welsh, B., & Wyder, T. K. 2005, ApJ, 619, L1
Mathis, J. S., Mezger, P. G., & Panagia, N. 1983, A&A, 128, 212
McKee, C. F., & Williams, J. P. 1997, ApJ, 476, 144
Meurer, G. R., Heckman, T. M., & Calzetti, D. 1999, ApJ, 521, 64
Meurer, G. R., Heckman, T. M., Leitherer, C., Kinney, A., Robert, C., & Garnett, D. R. 1995, AJ, 110, 2665
Moustakas, J., & Kennicutt, Jr., R. C. 2006, ApJS, 164, 81
Moustakas, J., Kennicutt, Jr., R. C., Tremonti, C. A., Dale, D. A., Smith, J., & Calzetti, D. 2010, ApJS, 190, 233
Muñoz-Mateos, J. C., Gil de Paz, A., Boissier, S., Zamorano, J., Dale, D. A., Pérez-González, P. G., Gallego, J., Madore, B. F., Bendo, G., Thornley, M. D., Draine, B. T., Boselli, A., Buat, V., Calzetti, D., Moustakas, J., & Kennicutt, R. C. 2009a, ApJ, 701, 1965

Muñoz-Mateos, J. C., Gil de Paz, A., Zamorano, J., Boissier, S., Dale, D. A., Pérez-González, P. G., Gallego, J., Madore, B. F., Bendo, G., Boselli, A., Buat, V., Calzetti, D., Moustakas, J., & Kennicutt, Jr., R. C. 2009b, ApJ, 703, 1569
Murphy, E. J., Condon, J. J., Schinnerer, E., Kennicutt, Jr., R. C., Calzetti, D., Armus, L., Helou, G., Turner, J. L., Aniano, G., Beirão, P., Bolatto, A. D., Brandl, B. R., Croxall, K. V., Dale, D. A., Donovan Meyer, J. L., Draine, B. T., Engelbracht, C., Hunt, L. K., Hao, C. ., Koda, J., Roussel, H., Skibba, R., & Smith, J. . T. 2011, ArXiv e-prints
Niklas, S., Klein, U., Braine, J., & Wielebinski, R. 1995, A&AS, 114, 21
Niklas, S., Klein, U., & Wielebinski, R. 1997, A&A, 322, 19
Onodera, S., Kuno, N., Tosaki, T., Kohno, K., Nakanishi, K., Sawada, T., Muraoka, K., Komugi, S., Miura, R., Kaneko, H., Hirota, A., & Kawabe, R. 2010, ApJ, 722, L127
Osterbrock, D. E., & Ferland, G. J. 2006, Astrophysics of gaseous nebulae and active galactic nuclei, ed. Osterbrock, D. E. & Ferland, G. J.
Pérez-González, P. G., Kennicutt, Jr., R. C., Gordon, K. D., Misselt, K. A., Gil de Paz, A., Engelbracht, C. W., Rieke, G. H., Bendo, G. J., Bianchi, L., Boissier, S., Calzetti, D., Dale, D. A., Draine, B. T., Jarrett, T. H., Hollenbach, D., & Prescott, M. K. M. 2006, ApJ, 648, 987
Prescott, M. K. M., Kennicutt, Jr., R. C., Bendo, G. J., Buckalew, B. A., Calzetti, D., Engelbracht, C. W., Gordon, K. D., Hollenbach, D. J., Lee, J. C., Moustakas, J., Dale, D. A., Helou, G., Jarrett, T. H., Murphy, E. J., Smith, J.-D. T., Akiyama, S., & Sosey, M. L. 2007, ApJ, 668, 182
Prugniel, P., & Heraudeau, P. 1998, A&AS, 128, 299
Rahman, N., Bolatto, A. D., Wong, T., Leroy, A. K., Walter, F., Rosolowsky, E., West, A. A., Bigiel, F., Ott, J., Xue, R., Herrera-Camus, R., Jameson, K., Blitz, L., & Vogel, S. N. 2010, ArXiv e-prints
Reipurth, B. 2008a, Handbook of Star Forming Regions, Volume I: The Northern Sky, ed. Reipurth, B.
—. 2008b, Handbook of Star Forming Regions, Volume II: The Southern Sky, ed. Reipurth, B.
Rosolowsky, E. W., Pineda, J. E., Kauffmann, J., & Goodman, A. A. 2008, ApJ, 679, 1338
Roussel, H., Gil de Paz, A., Seibert, M., Helou, G., Madore, B. F., & Martin, C. 2005, ApJ, 632, 227
Salim, S., Rich, R. M., Charlot, S., Brinchmann, J., Johnson, B. D., Schiminovich, D., Seibert, M., Mallery, R., Heckman, T. M., Forster, K., Friedman, P. G., Martin, D. C., Morrissey, P., Neff, S. G., Small, T., Wyder, T. K., Bianchi, L., Donas, J., Lee, Y., Madore, B. F., Milliard, B., Szalay, A. S., Welsh, B. Y., & Yi, S. K. 2007, ApJS, 173, 267
Schlegel, D. J., Finkbeiner, D. P., & Davis, M. 1998, ApJ, 500, 525
Schnee, S., Li, J., Goodman, A. A., & Sargent, A. I. 2008, ApJ, 684, 1228
Schruba, A., Leroy, A. K., Walter, F., Sandstrom, K., & Rosolowsky, E. 2010, ApJ, 722, 1699
—. 2011, ApJ, 722, 1699
Schuster, K.-F., Boucher, C., Brunswig, W., Carter, M., Chenu, J.-Y., Foullieux, B., Greve, A., John, D., Lazareff, B., Navarro, S., Perrigouard, A., Pollet, J.-L., Sievers, A., Thum, C., & Wiesemeyer, H. 2004, A&A, 423, 1171
Storey, P. J., & Hummer, D. G. 1995, MNRAS, 272, 41
Strong, A. W., & Mattox, J. R. 1996, A&A, 308, L21
Thilker, D. A., Boissier, S., Bianchi, L., Calzetti, D., Boselli, A., Dale, D. A., Seibert, M., Braun, R., Burgarella, D., Gil de Paz, A., Helou, G., Walter, F., Kennicutt, Jr., R. C., Madore, B. F., Martin, D. C., Barlow, T. A., Forster, K., Friedman, P. G., Morrissey, P., Neff, S. G., Schiminovich, D., Small, T., Wyder, T. K., Donas, J., Heckman, T. M., Lee, Y., Milliard, B., Rich, R. M., Szalay, A. S., Welsh, B. Y., & Yi, S. K. 2007, ApJS, 173, 572
Thilker, D. A., Braun, R., & Walterbos, R. A. M. 2000, AJ, 120, 3070
Vacca, W. D., Garmany, C. D., & Shull, J. M. 1996, ApJ, 460, 914
Walter, F., Brinks, E., de Blok, W. J. G., Bigiel, F., Kennicutt, R. C., Thornley, M. D., & Leroy, A. 2008, AJ, 136, 2563
Wilson, C. D., Warren, B. E., Israel, F. P., Serjeant, S., Bendo, G., Brinks, E., Clements, D., Courteau, S., Irwin, J., Knapen, J. H., Leech, J., Matthews, H. E., Mühle, S., Mortier, A. M. J., Petitpas, G., Sinukoff, E., Spekkens, K., Tan, B. K., Tilanus, R. P. J., Usero, A., van der Werf, P., Wiegert, T., & Zhu, M. 2009, ApJ, 693, 1736
Wong, T., & Blitz, L. 2002, ApJ, 569, 157
Wyder, T. K., Martin, D. C., Schiminovich, D., Seibert, M., Budavári, T., Treyer, M. A., Barlow, T. A., Forster, K., Friedman, P. G., Morrissey, P., Neff, S. G., Small, T., Bianchi, L., Donas, J., Heckman, T. M., Lee, Y., Madore, B. F., Milliard, B., Rich, R. M., Szalay, A. S., Welsh, B. Y., & Yi, S. K. 2007, ApJS, 173, 293
Young, J. S., Xie, S., Tacconi, L., Knezek, P., Viscuso, P., Tacconi-Garman, L., Scoville, N., Schneider, S., Schloerb, F. P., Lord, S., Lesser, A., Kenney, J., Huang, Y.-L., Devereux, N., Claussen, M., Case, J., Carpenter, J., Berry, M., & Allen, L. 1995, ApJS, 98, 219
Zibetti, S., Charlot, S., & Rix, H. 2009, MNRAS, 400, 1181

APPENDIX

ESTIMATING THE RADIATION FIELD ASSOCIATED WITH THE CIRRUS

Our fits to the dust properties yield the radiation field powering dust emission in each ring, including the best-fit single radiation field illuminating the bulk of the dust mass, $U_{\rm min}$. The fits do not distinguish how much of this $U_{\rm min}$ is associated with recently formed stars and how much results from an older stellar population. Because of this uncertainty, we cannot simply identify all 24μm emission associated with $U_{\rm min}$ as cirrus. In this appendix, we attempt an independent estimate of the radiation field, $U_{\rm cirrus}$, not directly associated with star formation. In the regime that we consider the intensity of the cirrus emission at 24μm, I_{24}, depends linearly on the incident radiation field (Section 5 and Figure 4), so that $I_{24}^{\rm cirrus} \propto U_{\rm cirrus}$.

Estimating $U_{\rm cirrus}$ requires that we define a "successful" cirrus subtraction, or equivalently a goodness-of-fit metric for a cirrus estimate. After considerable experimentation we settled on the following: *a successful cirrus estimate removes most emission from faint regions but does not overcorrect the map or delete emission actually associated with star formation.* This means that we look for $U_{\rm cirrus}$ that significantly affects low-lying emission but does not systematically oversubtract. In practice we use five measurements of structure in the cirrus-subtracted 24μm map to assess the quality of our $U_{\rm cirrus}$ determination:

1. The fraction of lines of sight for which the 24μm is set to zero, that is, completely removed, by the cirrus subtraction (this will include lines of sight where the 24μm has been oversubtracted).

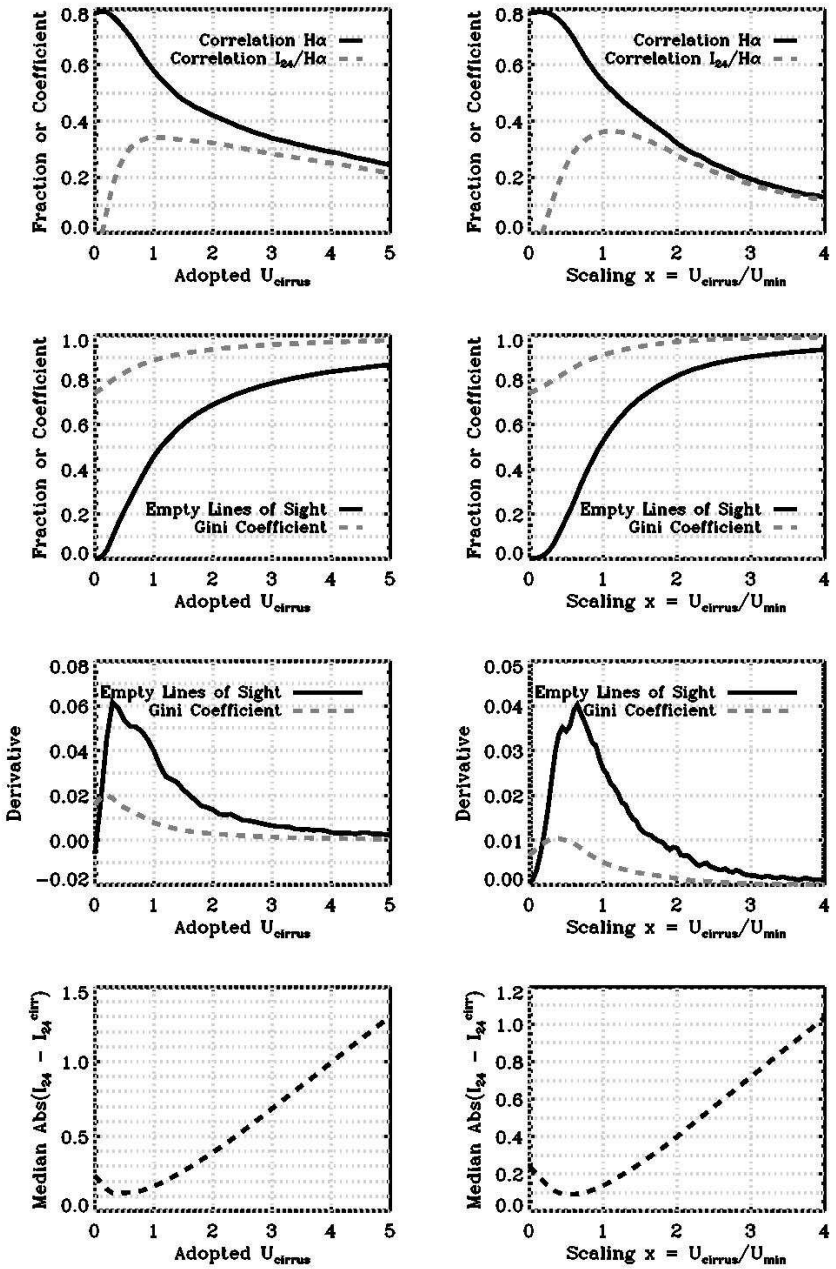

FIG. 17.— The structure of 24μm emission after cirrus subtraction as a function of (*left column*) adopted cirrus radiation field, $U_{\rm cirrus}$ and (*right column*) adopted scaling factor x when $U_{\rm cirrus} = x\ U_{\rm min}$. The top row shows the correlation of 24μm emission with Hα emission or $A_{\rm H\alpha}$ inferred from the ratio $I_{24}/I_{\rm H\alpha}$. The second row shows the fraction of lines of sight where the cirrus removes all emission, and the Gini coefficient, a non-parametric measure of the unevenness of the distribution. The third row shows the derivatives of the fraction of pixels set to zero by the cirrus subtraction and the Gini coefficient as a function of the radiation field. The bottom row shows the median absolute difference between the cirrus map calculated from the indicated radiation field and the observed "low-lying" emission, with low-lying defined as all data less than the median.

2. The median absolute difference between the cirrus estimate and the initial 24μm map for faint emission. We define "faint" emission as emission below the median I_{24} in the map. This measures the degree to which the cirrus matches the 24μm map over the faint lines of sight.

3. The Gini coefficient (Gini 1912), a non-parametric measure of the unevenness of the distribution of emission (see discussion in Muñoz-Mateos et al. 2009b). This measures the degree to which the IR emission is concentrated into a few bright regions after the cirrus subtraction.

4. The rank correlation coefficient between Hα emission and cirrus-subtracted 24μm emission. In principle, this should measure the degree to which the morphology of the cirrus-subtracted 24μm map matches that of the Hα, a relatively unambiguous signature of high-mass star formation (but see complications below).

5. The rank correlation coefficient relating Hα emission and the ratio of 24μm-to-Hα emission, or equivalently $A_{\rm H\alpha}$. This measures the degree to which the cirrus-subtracted map obeys the expectation that more actively star-forming regions exhibit more extinction (but see below).

Calculations: For each galaxy, we carry out a cirrus subtraction for a range of test radiation fields and measure each of these five statistics for each test radiation field. We consider: (1) a single fixed radiation field, $U_{\rm cirrus}$, for the whole sample; (2) a single fixed radiation field, $U_{\rm cirrus}$, per galaxy; and (3) the case where the cirrus is powered by a scaled version of the best-fit $U_{\rm min}$ from the dust SED fits (i.e., $U_{\rm cirrus} = xU_{\rm min}$; recall $U_{\rm min}$ is derived from a fit for each radial ring). We vary these test fields from $U_{\rm cirrus} = 0$–5 and try scaling $U_{\rm cirrus} = xU_{\rm min}$ with x from 0–4. We consider $x > 1$, which may seem counterintuitive, to allow the possibility that the cirrus is driven by a radiation field locally more intense than that indicated by the $U_{\rm min}$ parameter fit at coarser ($40''$) resolution or because of contribution from fields $> U_{\rm min}$. In the end we do find $x < 1$ to yield the best results.

Figure 17 shows these measurements for all of our data, plotting each as a function of the radiation field $U_{\rm cirrus}$ assumed to power the cirrus (left column) or the factor x by which we scale $U_{\rm min}$, $U_{\rm cirrus} = xU_{\rm min}$ (right column). A single $U_{\rm cirrus}$ for the whole sample is certainly too simplistic, but the plots still give a good overview of the calculations. We include all data with $\langle\Sigma_{\rm SFR}\rangle > 10^{-4}$ M$_\odot$ yr^{-1} kpc^{-2}. We will find $\Sigma_{\rm SFR}$ to be unreliable at this low level but including these low-lying data in the cirrus calculations is important. A major goal of the cirrus subtraction will be to correct for faint but pervasive emission that extends down to this level.

The left column of Figure 17 shows that over the range $U_{\rm cirrus} \sim 0.3$–1.5, the cirrus subtraction varies between creating no empty lines of sight at all to removing all emission associated with more than half of the lines of sight. Over this same range, the correlation of extinction with Hα surface brightness improves. The Gini coefficient also increases, implying a stronger concentration of IR emission into a few bright regions. The deviation between the calculated cirrus and the faint parts of the sample is minimized for $U_{\rm cirrus} \sim 0.4$ (bottom left panel). The right column shows similar behavior scaling the fit radiation field ($U_{\rm min}$) by ~ 0.3–1, with the match between the calculated cirrus and faint emission best for $\sim 0.6\ U_{\rm min}$.

Identification of $U_{\rm cirrus}$: Figure 17 suggests a rough magnitude of the cirrus. Low values, $U_{cirrus} \lesssim 0.3$ will have little or no effect on the 24μm map and not produce a meaningful correction. High values $U_{cirrus} \gtrsim 1$ will suppress a very large part of the map and oversubtract emission from low intensity regions. We want to pick a cirrus correction in the intermediate regime, near the regions of steep positive slope in the fraction of blank lines of sight or Gini coefficient where the cirrus subtraction has the maximum effect without oversubtraction. The derivative of the fraction of lines of blank lines of sight and the Gini coefficient appear in the middle row of Figure 17 and indeed peak in the desired range. Even more basically, we argue that the most appropriate $U_{\rm cirrus}$ will be the one that generates the minimum scatter between the calculated cirrus and the real map for low-level emission. The bottom row in Figure 17 plots the median absolute difference between the cirrus and low-lying emission, defined as I_{24} below the median.

Thus, we have several candidates for $U_{\rm cirrus}$:

1. $U_{\rm cirrus}$ that yields the maximum derivative of the fraction of blank lines of sight vs. U.

2. $U_{\rm cirrus}$ that yields the maximum of derivative of the Gini coefficient vs. U.

3. $U_{\rm cirrus}$ that yields the minimum absolute difference between the calculated cirrus and the observed 24μm intensity for faint lines of sight.

4. U at which the fraction of blank pixels passes some fiducial threshold; 0.2 works well for our data based on the tests in the next section.

5. U that yields the maximum correlation of Hα and 24μm.

6. U that yields the maximum correlation of Hα with $A_{\rm H\alpha}$, traced by $I_{24}/I_{\rm H\alpha}$ after cirrus subtraction.

Testing of Our U-Fitting Metrics: We evaluate these metrics by testing their ability to recover a known radiation field. We generate a series of simulated 24μm data sets with cirrus powered by a range of $U_{\rm cirrus}$ and a similar set powered by scaled versions of $U_{\rm min}$. To do so we:

1. Scale the Hα data to correspond to the 24μm emission expected for $A_{\rm H\alpha} = 1$ mag. This represents a plausible core of IR associated with star formation.

2. Rescale the calculated cirrus for each line of sight to have a known $U_{\rm cirrus}$ between 0 and 5 and then add it to this "star forming" 24μm emission to produce a realistic mix of star formation and cirrus. We run a parallel set of calculations with $U_{\rm cirrus} = xU_{\rm min}$ and x ranging from 0 to 4.

3. Add lognormal (multiplicative) scatter with magnitude 0.15 dex to the cirrus map to reflect uncertainty in the cirrus estimate.

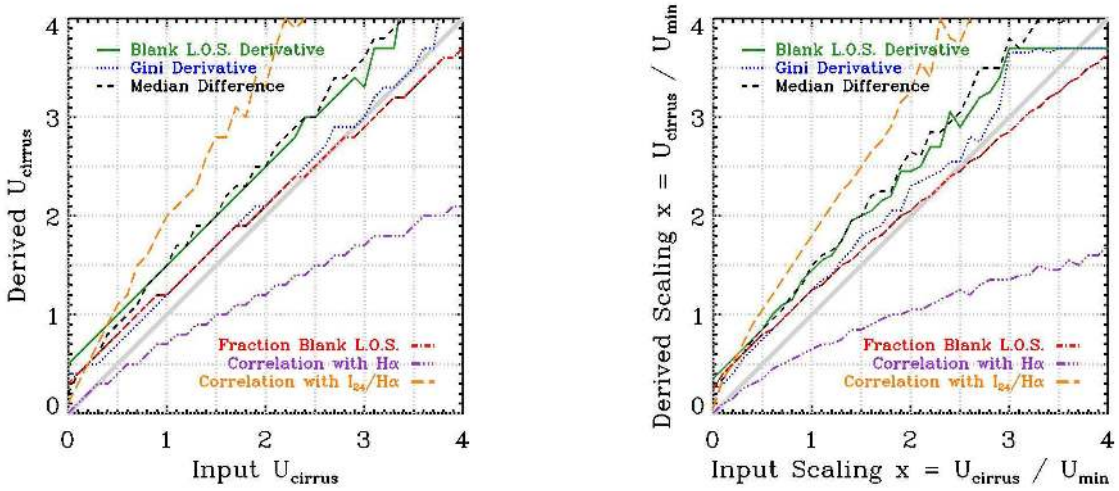

FIG. 18.— *Test of U-fitting metrics.* Ability of our $U_{\rm cirrus}$ goodness-of-fit metrics to recover the radiation field powering the cirrus in model case where the true $U_{\rm cirrus}$ is known. The lines show U derived from maximizing the derivative of the fraction of blanked lines of sight; maximizing the derivative of the Gini coefficient; minimizing the scatter between the cirrus and low-lying emission; matching a fixed fraction (here 20%) of blanked lines of sight; maximizing the rank correlation between Hα and I_{24}; and maximizing the rank correlation between Hα and $I_{24}/I_{\rm H\alpha}$ (a quantity closely related to the Hα extinction, $A_{\rm H\alpha}$). The *left* panel shows the results of Monte Carlo calculations aimed at recovering a fixed $U_{\rm cirrus}$, the *right* panel explores the ability of our metrics to recover the scaling factor x when $U_{\rm cirrus} = xU_{\rm min}$, with $U_{\rm min}$ fit from the IR SED. A solid gray line in each panel shows equality for reference.

We apply each metric to each simulated 24μm map and to estimate either $U_{\rm cirrus}$ or x. Figure 18 plots the ability of the methods to recover the input cirrus radiation field. The left panel plots results for a fixed $U_{\rm cirrus}$, the right panel for a scaled version of $U_{\rm min}$, so that $U_{\rm cirrus} = xU_{\rm min}$.

The tests show that the derivative-based and minimum scatter metrics recover the input $U_{\rm cirrus}$ well with a small bias to recover higher values than the input. This small high bias reflects the fact that low lying Hα pervades much of the map so that forcing many lines of sight to zero actually moves some "star formation" emission into "cirrus." The effect is mild. Picking the $U_{\rm cirrus}$ that recovers 20% completely blank lines of sight also works well, but this particular value of 20% had to be tuned for our data.

The rank-correlation based metrics, Hα with either I_{24} or $I_{24}/I_{\rm H\alpha}$, show strong biases, especially toward large $U_{\rm cirrus}$ or x. The correlation of I_{24} with $I_{\rm H\alpha}$ is biased toward to recover lower $U_{\rm cirrus}$ than the input because the cirrus correction is noisy. As we apply progressively more cirrus correction to I_{24}, this scatter artificially suppresses the correlation. The extinction correlation is biased to recover higher $U_{\rm cirrus}$ than input because the two quantities, $I_{\rm H\alpha}$ and $I_{24}/I_{\rm H\alpha}$, are intrinsically anti-correlated for random I_{24}.

We conclude from this test that the derivative of the blank-pixel fraction, the derivative of the Gini coefficient, a tuned blank-pixel fraction threshold, and the minimum absolute deviation between calculated cirrus and observed intensity all represent useful tools to identify the radiation field driving the cirrus (though they have a mild bias to recover too much cirrus). We expect that the rank correlation coefficients, which fail in our data, will emerge as very useful for higher resolution studies but the resolution of our current data set is too coarse to take full advantage of them.

Galaxy-by-Galaxy Estimates: So far we have examined the ensemble of our data, but the radiation field certainly varies among and within galaxies. Our metrics require a population of points to identify a best-fit $U_{\rm cirrus}$. Therefore they cannot be applied point-by-point, but our individual galaxies do have enough data to derive $U_{\rm cirrus}$.

Figure 19 shows the median $U_{\rm cirrus}$ (left) and the best-fit scaling of $U_{\rm min}$ (right) derived from our four useful goodness-of-fit statistics: maximizing the derivative of the blank line of sight, maximizing the derivative of the Gini coefficient, finding $U_{\rm cirrus}$ that minimizes the difference between 24μm and cirrus for faint lines of sight, and finding $U_{\rm cirrus}$ that blanks a fixed fraction of lines of sight. We plot both $U_{\rm cirrus}$ and the best-fit scaling x in $U_{\rm cirrus} = xU_{\rm min}$ as a function of the median fit radiation field $U_{\rm min}$ for that galaxy from the Draine & Li (2007) models.

The left panel of Figure 19 reveals a median $U_{\rm cirrus}$ of 0.6 and a good correspondence between our $U_{\rm cirrus}$ and fit $U_{\rm min}$. The rank correlation relating the two is ~ 0.9, but the derived $U_{\rm cirrus}$ are smaller than the fit $U_{\rm min}$ by a factor of two on average (dashed line). The exceptions are the two bright systems NGC 337 and NGC 7331 where both the dust fitting and our metrics suggest a very high diffuse field $U \sim 4$–5. These targets are interesting points of follow-up but appear to be special cases, as we expect the very high field to be partially due to resolution and geometric effects. We do not follow up further here, but note these galaxies as excellent targets for *Herschel* study.

The right panel of Figure 19 shows the best-fit scaling x for the case where $U_{\rm cirrus} = xU_{\rm min}$, again as a function of the fit field $U_{\rm min}$. The median scaling is $x \approx 0.6$ with about a factor of two scatter. There is certainly some correlation between host galaxy and best scaling and again NGC 337 and NGC 7331 appear as outliers, though here with very large error bars, meaning large scatter in x determined by different methods. This median scaling in the right panel

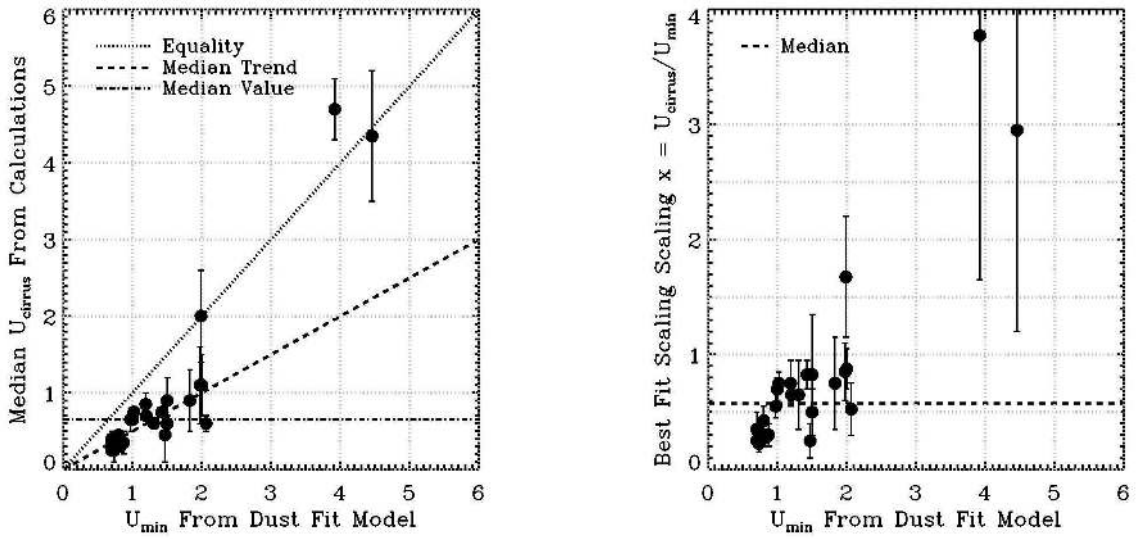

FIG. 19.— (*left*) Calculated $U_{\rm cirrus}$ vs. $U_{\rm min}$ from fitting dust models to the IR SED. We show the median $U_{\rm cirrus}$ (y-axis) estimated for individual galaxies (points) using our four reliable methods. We plot $U_{\rm cirrus}$ as a function of each galaxy's average $U_{\rm min}$, the fixed radiation yielded from fitting the Draine & Li (2007) models to the IR SED. $U_{\rm cirrus}$ tracks $U_{\rm min}$ well, but tends to be lower than $U_{\rm min}$ by a factor of ≈ 2. The dashed line shows $U_{\rm cirrus} = 0.5\ U_{\rm min}$, which is a good description of the data. The dash-dotted line show $U_{\rm cirrus} \sim 0.6$, the median value. The *right* panel shows an analogous determination of the best-fit factor x considering $U_{\rm cirrus} = x\ U_{\rm min}$. The dashed line shows the median $x \approx 0.6$. NGC 337 and NGC 7331 appear as outliers in both panels.

and the typical ratio of $U_{\rm cirrus}$ to to $U_{\rm min}$ in the left panel agree with one another fairly well, both suggesting a cirrus radiation field about half of the fit $U_{\rm min}$.

The good correspondence between our calculated $U_{\rm cirrus}$ and the fit $U_{\rm min}$ suggests that we can use a scaled version of $U_{\rm min}$ for local estimates of the cirrus. This is desirable, as it allows us to capture local variations in the radiation field driving the cirrus. The correspondence of $U_{\rm cirrus}$ and $U_{\rm min}$ also reinforces that our calculations have returned a meaningful result, inasmuch as they return information similar to an SED fit.

Conclusions From Radiation Field Calculations: We define and test a series of goodness-of-fit metrics that attempt to identify the radiation field powering the cirrus at 24μm. We require that subtracting a cirrus driven by this radiation field significantly affect the faint emission in the map but not dramatically oversubtract emission.

For our data set, the cirrus correction should employ $U_{\rm cirrus} \sim 0.5 U_{\rm min}$, a median $U_{\rm cirrus} \sim 0.6$–0.7. There is a factor of ~ 2 scatter in these estimates from galaxy to galaxy with two notable outliers. In practice this lowers the median U used in our calculation from ~ 1.4 times the Solar Neighborhood ISRF on average to ~ 0.6. This appears reasonable; as noted, the Solar Neighbornood ISRF likely includes significant contributions from nearby young stars. When we refer to "cirrus" throughout the rest of the paper we will adopt $U_{\rm cirrus} = 0.5 \times U_{\rm min}$. To test the impact of this conclusion, we will also occasionally refer to "twice" or "double" cirrus, which indicates that we have taken $U_{\rm cirrus} = 1.0 \times U_{\rm min}$, i.e., double our best estimate of the appropriate $U_{\rm cirrus}$ value.

The critical points are that the rough magnitude of the cirrus is slightly below the Solar Neighborhood ISRF and does appear to track the radiation field estimated from dust fits. The specific scaling $U_{\rm cirrus} \sim 0.5\ U_{\rm min}$ almost certainly results from the interaction of resolutions for which we carry out our dust fits ($40''$) and cirrus calculations (1 kpc$\sim 13''$) and we do not expect it to be a general result . For a recent demonstration of the shortcomings of simple power law distributions of U to yield scale-independent dust-fitting results see the work by Galliano et al. (2011) on the Large Magellanic Cloud. The magnitude, $U_{\rm cirrus} \sim 0.6$, on the other hand, seems plausible and may represent a reasonable conservative starting point (as might $U \sim 1$). In any case, our understanding of IR cirrus emission will benefit greatly from achieving good IR SED coverage at very high spatial resolution (e.g., Lawton et al. 2010). This will allow the kind of dust-SED based analysis that we apply here to be undertaken on maps with the ability to cleanly distinguish quiescent and star-forming parts of a galaxy. In this regime, we expect the rank correlation statistics that we test and reject (I_{24} with Hα morphology) and simple estimates of the total U in quiescent regions to become powerful tools.

$\Sigma_{\rm SFR}$ ESTIMATES FOR HERACLES DISK GALAXIES

In this appendix we plot $\Sigma_{\rm SFR}$ estimates based on our data. Figures 20 – 24 show each line of sight considered in this paper as a point color-coded by $\Sigma_{\rm SFR}$. As described in Section 2, these data are sampled on a hexagonal grid with spacing 0.5 kpc except for a few distant cases noted Table 1, which are sampled with $6.5''$ (half-beam) spacing. Gray points indicate where the Hα+24μm based $\Sigma_{\rm SFR} < 10^{-3}$ M$_\odot$ yr^{-1} kpc^{-2}, our limit for a robust measurement (Section 7). From left to right panels show $\Sigma_{\rm SFR}$ estimated from Hα+24μm, FUV+24μm, FUV only, Hα only, and 24μm only. In all panels we have applied our recommended cirrus correction (Section 5) to the 24μm data and adopt our recommended $w_{\rm H\alpha} = 1.3$ and $w_{\rm FUV} = 1.7$. The 24μm-only panel uses $w = 1.3$.

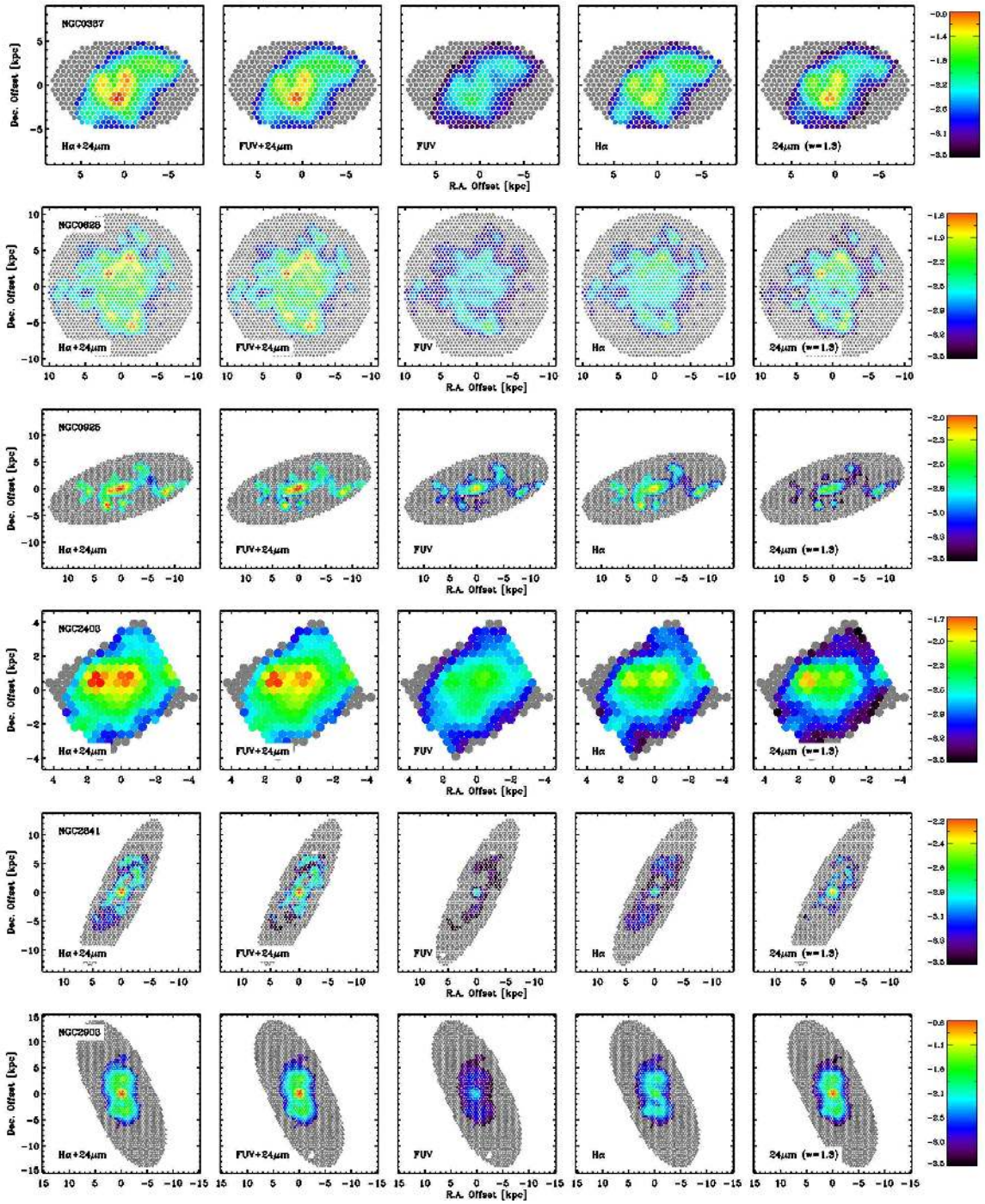

FIG. 20.— $\Sigma_{\rm SFR}$ estimates for the individual lines of sight studied throughout this paper. The axes show displacement from the galaxy center in kpc. We color code points by $\log_{10}$ $\Sigma_{\rm SFR}$ estimated following the recommendations in the main text. We fix the scale for each galaxy to allow comparison of different components but the color scale varies from target to target according to the dynamic range in the maps. Points where $\Sigma_{\rm SFR}$ estimated from Hα+24μm $< 10^{-3}$ M$_\odot$ yr^{-1} kpc^{-2} are color coded gray in all panels.

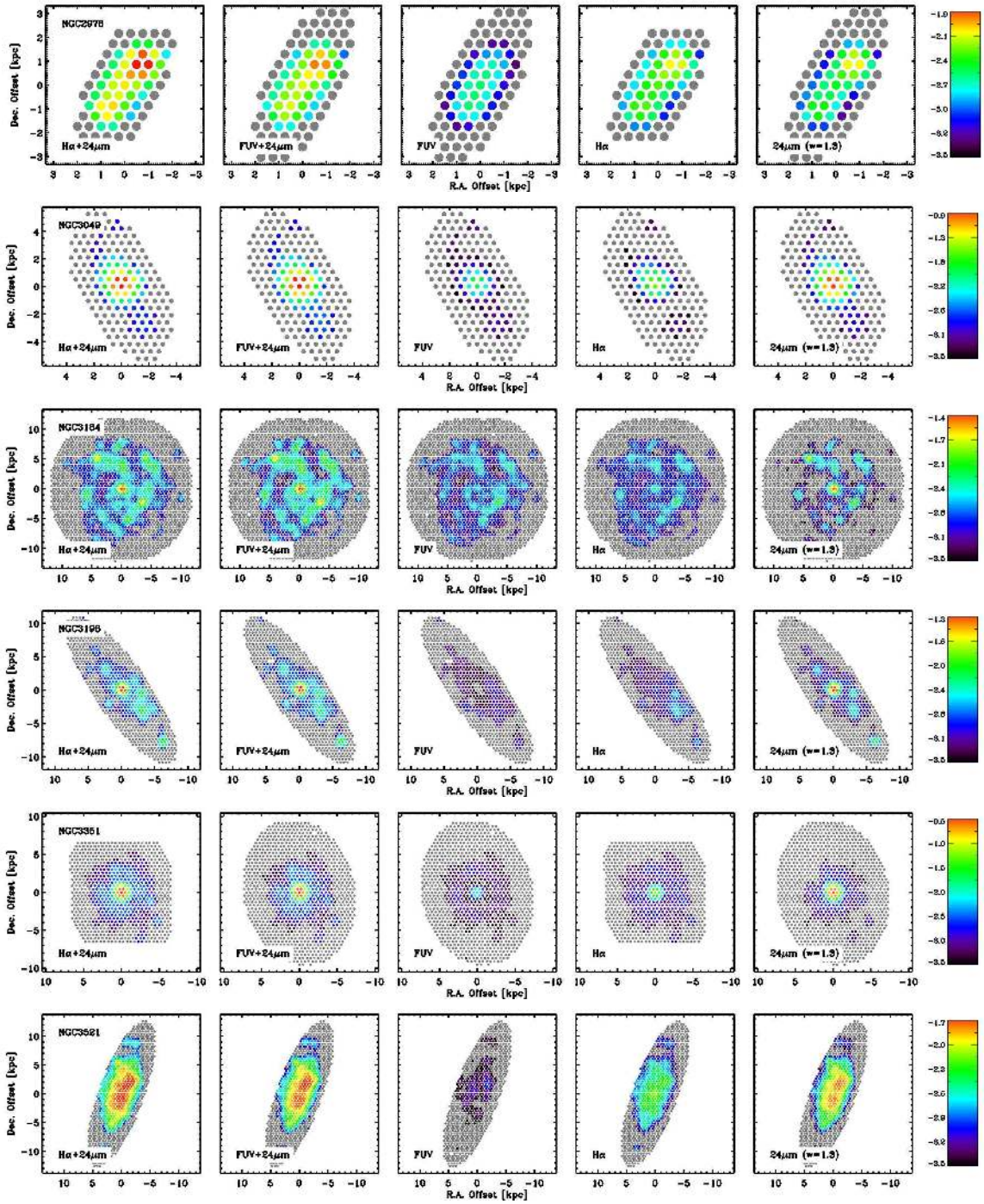

FIG. 21.— As Figure 20.

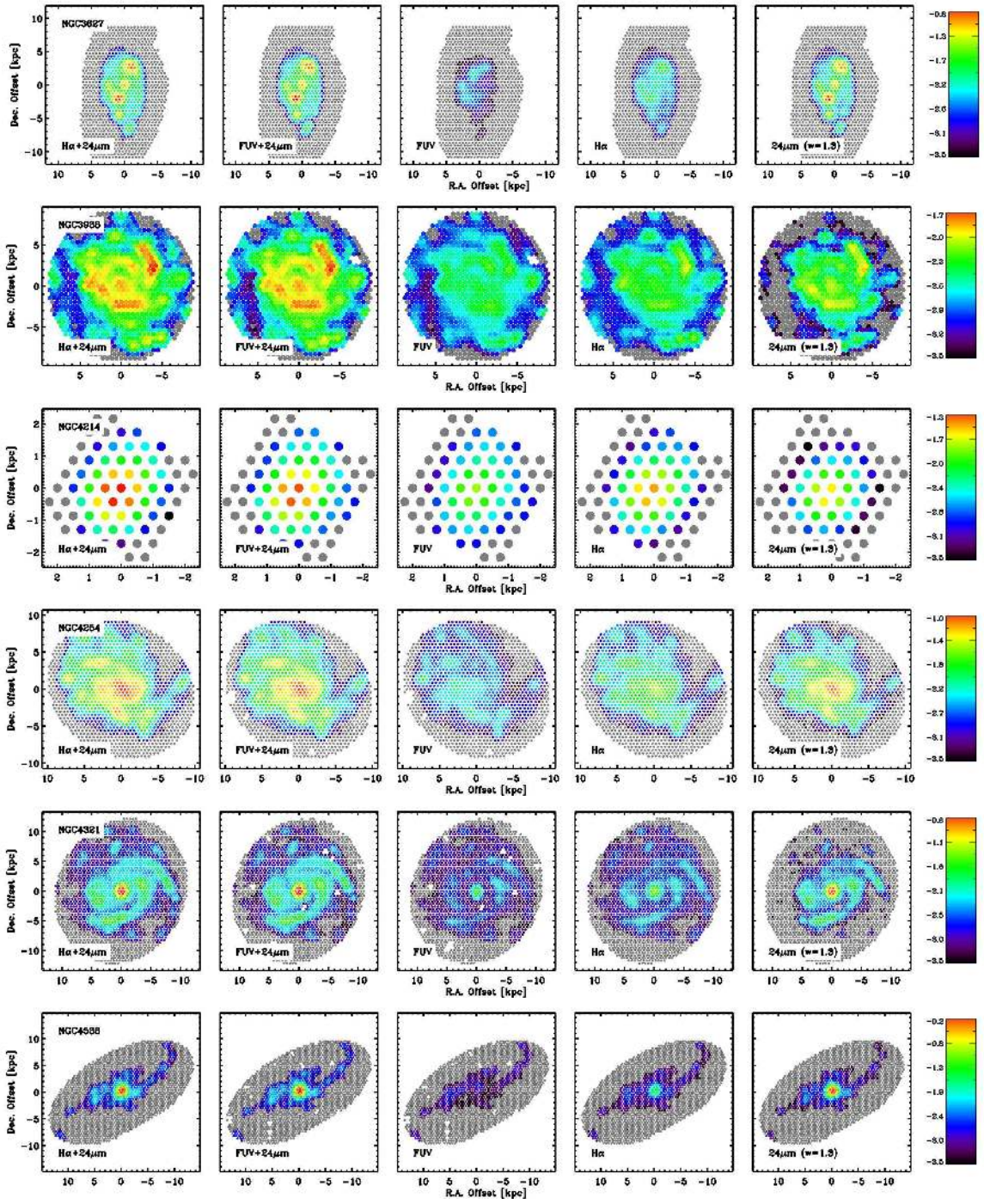

FIG. 22.— As Figure 20.

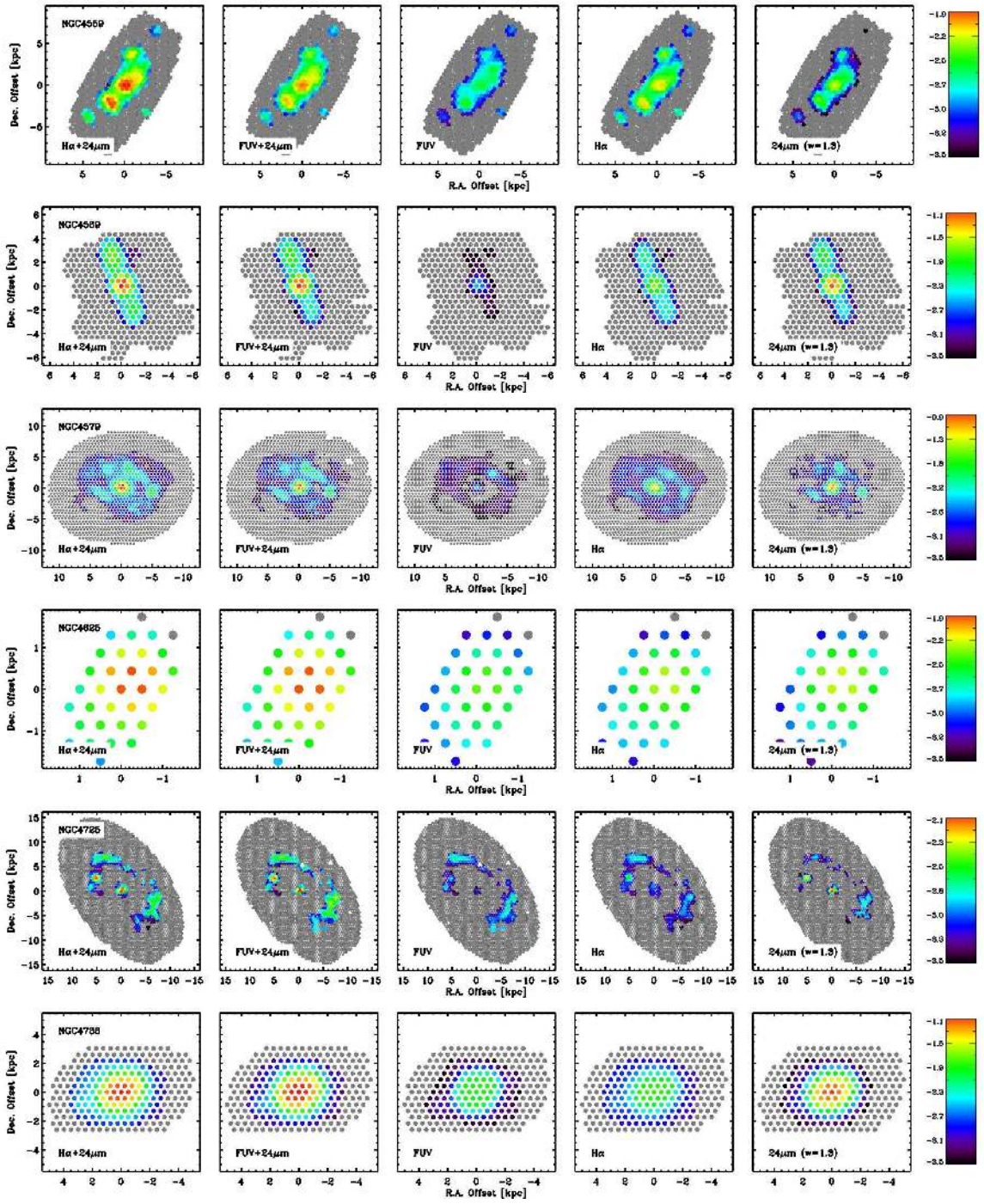

FIG. 23.— As Figure 20.

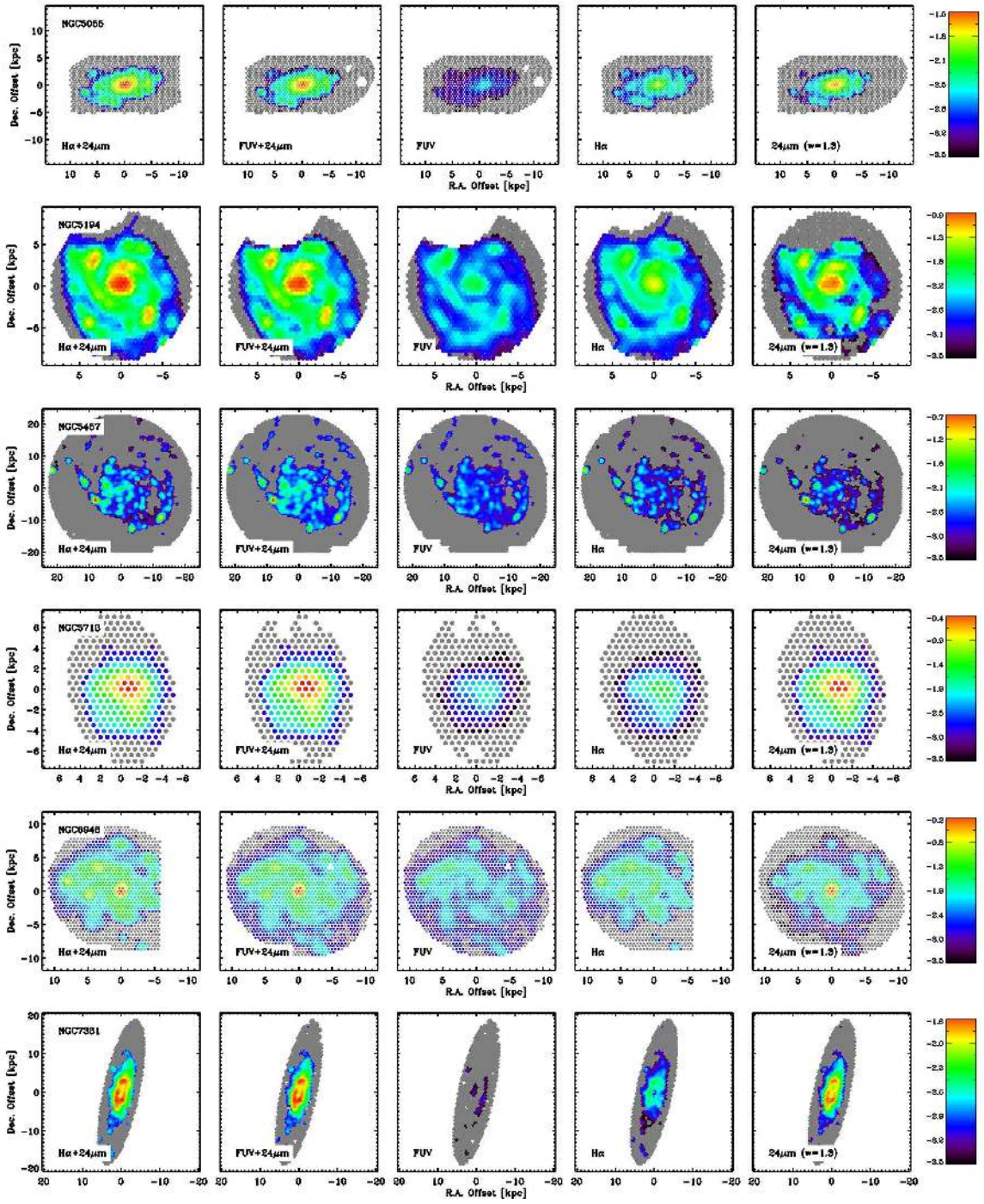

FIG. 24.— As Figure 20.